CELLULAR ADHESION DYNAMICS: INVESTIGATION OF MOLECULAR CLUTCH ATTACHMENT AND FORCE TRANSMISSION

A DISSERTATION
SUBMITTED TO THE FACULTY OF THE GRADUATE SCHOOL
OF THE UNIVERSITY OF MINNESOTA
BY

CLARENCE ELVIN CHAN

IN PARTIAL FULFILLMENT OF THE REQUIREMENTS
FOR THE DEGREE OF
DOCTOR OF PHILOSOPHY

ADVISOR DAVID J. ODDE

DECEMBER 2008

© Clarence Elvin Chan, 2008

ACKNOWLEDGEMENTS

First, I would like to thank my advisor, David Odde, for his patience and direction over my graduate career. Through his guidance, I have truly learned a great deal, not only scientific knowledge, but about myself as well. I would also like to extend thanks to my committee members: Victor Barocas, Paul Letourneau, and Lorene Lanier for their time serving on my committee, whose critical review helped shape and refine a great deal of my work.

I would also like to thank members of the Odde Lab, whose friendship and camaraderie made my six years spent in the lab seem much shorter. Thank you Andy, Dominique, Melissa, Erkan, and Aleksey for celebrating with me during the highs and encouraging me during the lows. I would also like to extend a special thanks to Erkan and Kwaku. Without their help, at least one chapter of this work would be missing.

Thanks also to my family and friends. Although they may never completely understand what I been working or why I've been away for all these years, I truly appreciate their genuine love and encouragement.

Finally, I would like to thank my wife, Carolina, who supported my decision to go back to school despite having to put our lives 'on hold'. Many a times, when I was ready to give up, her steadfast support saw me through. Her patience, understanding, and love have been vital to the completion of this work. I will forever be in her debt.

This dissertation is dedicated to my family and wife,
without whose love and support this work would have been impossible.

ABSTRACT

As the major structural element of the cell, the cytoskeleton plays a vital role in response and transmission of forces in both extracellular and intracellular environments. For instance, in cell motility, the cell utilizes a host of proteins to physically link F-actin to the extracellular substrate, allowing the cell to exert traction forces as well as probe the mechanics of its local environment. During mitosis, the cell constructs a mitotic spindle, using microtubules and kinetochores to exert forces that segregate sister chromatids. Ultimately, understanding how cells build these robust molecular machines for unique tasks could one day lead to therapeutics that treat disease causing dysfunctions in these vital cellular processes.

In order to explore how molecular clutches work in concert with the cytoskeleton to exert forces and maintain attachment under load, we developed a mechano-chemical cellular adhesion dynamics framework to simulate these processes. In the case of cellular motility, we find that a "motor-clutch" mechanism exhibits substrate-stiffness sensitive dynamics. On soft substrates, motor-clutch motility exhibits "load-and-fail" dynamics that lead to higher rates of retrograde flow and lower traction force transmission compared to stiff substrates. We confirm these predictions experimentally using embryonic chick forebrain neurons (ECFNs) plated on compliant polyacrylamide gels (PAGs) demonstrating that a motor clutch system could be the basis of cellular mechanosensing.

We also use cellular adhesion dynamics to explore kinetochore-microtubule attachment during mitosis to identify what properties might be important in maintaining attachment during mitosis. We show that molecular clutch microtubule-lattice diffusion

is important for relieving clutch stresses, prolonging bond life-times and minimizing detachment forces. Furthermore, molecular clutches that preferentially associate with interdimer interfaces, rather than with intradimer interfaces, promote robust kinetochore attachment by preventing the more distal, attachment-promoting linkers from becoming nonproductive. These findings help further our understanding of the mechanochemical basis of kinetochore attachment and mitosis, a process essential throughout development.

TABLE OF CONTENTS

- CHAPTER 1 - INTRODUCTION 1
1.1 MOLECULAR CLUTCHES IN CELL MOTILITY AND MECHANOSENSING 1
1.1.1 Actin Dynamics in Motile Cells 2
1.1.2 Integrins and Focal adhesions 4
1.1.3 Motor-clutch motility 5
1.2 MOLECULAR CLUTCHES IN MITOSIS 6
1.2.1 Microtubules Dynamics and the Kinetochore 7
1.2.2 Ndc80 and Dam1 complexes 8
1.2.3 The Hill Sleeve Model of Kinetochore End-tracking 10

- CHAPTER 2 - TRACTION DYNAMICS OF FILOPODIA ON COMPLIANT SUBSTRATES 12
2.1 ABSTRACT 12
2.2 BACKGROUND 13
2.3 METHODS 14
2.3.1 Computational Modeling of Stochastic Motor-Clutch Motility on Compliant Substrates 14
2.3.2 Transfection and Cell Culture 17
2.3.3 Preparation and Characterization of PAGs 18
2.3.4 Live Cell Imaging 20
2.3.5 Image Analysis 21
2.3.6 Statistical Analysis 26
2.4 RESULTS 27
2.4.1 Simulated Motor-Clutch Dynamics on Compliant Substrates 27
2.4.2 Experimental Tests of Motor-Clutch Dynamics on Compliant Substrates 30
2.5 DISCUSSION 37
2.6 ACKNOWLEDGEMENTS 43
2.7 TABLES AND FIGURES 44

- CHAPTER 3 - MICROTUBULE-LATTICE DIFFUSION AND INTERDIMER ASSOCIATIONS PROMOTE ROBUST KINETOCHORE COUPLING 61
3.1 ABSTRACT 61
3.2 BACKGROUND 62
3.3 METHODS 64
3.3.1 Mathematical Model 64
3.4 RESULTS 70
3.4.1 Stochastic Model of Kinetochore-Clutch Adhesion Dynamics 70
3.4.2 MT-lattice diffusion expands the parameter space of successful kinetochore end-tracking 71
3.4.3 Interdimer association prevents clutch poisoning 72
3.4.4 A kinetochore of interdimer associating, MT-lattice diffusing clutches end-tracks most robustly 75
3.5 DISCUSSION 76
3.6 ACKNOWLEDGEMENTS 79
3.7 TABLES AND FIGURES 80

- CHAPTER 4 - SUMMARY AND CONCLUSIONS 93

APPENDIX A - NANOSCALE MARKER BEAD DYNAMICS ON SOFT AND STIFF SUBSTRATES 97

APPENDIX B - EFFECTS OF SUBSTRATE STIFFNESS ON U251 GLIOMA MORPHOLOGY AND MOTILITY 110

REFERENCES 120

LIST OF TABLES

Table 2-1 Parameters of the Stochastic Motor-Clutch Model. 44
Table 3-1 Parameters of the Stochastic Kinetochore-Clutch Model. 80

LIST OF FIGURES

Figure 2-1 Validation of bead tracking algorithm. 45
Figure 2-2 Estimation of maximum filopodial traction force using the *Cerruti* solution. 46
Figure 2-3 Validation of cross-correlation F-actin flow tracking algorithm. 47
Figure 2-4 A model for motor-clutch motility on compliant substrates predicts substrate stiffness-dependent dynamics. 49
Figure 2-5 Clutch dynamics transition is a robust feature of motor-clutch model. 50
Figure 2-6 Spatial map of neuronal traction force dynamics. 51
Figure 2-7 ECFN growth cone advance depends on β1-integrins. 52
Figure 2-8 Growth cone filopodia on compliant substrates exert traction forces with "load-and-fail" dynamics. 53
Figure 2-9 High temporal resolution (100 ms) traction force dynamics reveal abrupt failure events. 54
Figure 2-10 Aggregate marker bead single time increment displacement distributions. 55
Figure 2-11 Growth cone filopodia F-actin retrograde flow rate abruptly transitions from low to high around an elastic modulus of E=1 kPa. 56
Figure 2-12 ECFNs die on extremely soft PAGs. 57
Figure 2-13 Untransfected ECFNs exhibit F-actin retrograde flow substrate stiffness sensitivity. 58
Figure 2-14 F-Actin retrograde flow in ECFN growth cones is myosin II dependent. 59
Figure 2-15 Surface tension of ECFNs decreases on stiff PAGs. 60
Figure 3-1 Schematic representation of a molecular kinetochore-clutch model. 81
Figure 3-2 Molecular clutch MT-lattice diffusion improves kinetochore tracking. 83
Figure 3-3 MT-lattice diffusion relieves clutch stress increasing the frequency of engagement. 84
Figure 3-4 Kinetochore systems with MT-lattice diffusion support greater loads over a wider range of parameter space. 85
Figure 3-5 Interdimer associating clutches improve MT end-tracking by recycling inactive clutches. 86
Figure 3-6 Interdimer associating kinetochores quickly recycles inactive distal clutches. 87
Figure 3-7 Kinetochore systems with interdimer associating clutches support greater loads over a wider range of parameter space. 88
Figure 3-8 A kinetochore of MT-lattice diffusing interdimer associating clutches supports the greatest loads. 89
Figure 3-9 Kinetochore systems with interdimer associating clutches that diffusion along the MT-lattice support the greatest loads over a wider range of parameter space. 90
Figure 3-10 Increasing loads reduces the valid parameter space and shifts the optimum. 91

Figure 3-11 An interdimer MT-lattice diffusing kinetochore-clutch system end-tracks at high MT depolymerization rates. 92

Figure A.1 Marker bead positions, trajectories and single time increment displacement distributions on (A) 260 Pa, (B) 730 Pa and (C) 1300 Pa PAGs..... 95
Figure B.1 U251 glioma area and shape are altered by substrate stiffness. 112
Figure B.2 U251 glioma expansion times are not significantly altered by substrate stiffness. 113
Figure B.3 U251 gliomas explore a larger surface area as PAG substrate stiffness increases. 114
Figure B.4 U251 glioma cells move faster as substrate stiffness increases. 115
Figure B.5 U251 glioma cells “diffuse” faster over stiffer PAG substrates. 116

- CHAPTER 1 -
INTRODUCTION

Everyday, our knowledge of cellular processes and their complexity grows. We continually identify proteins involved in complex networks that regulate specific behaviors or responses. But these biochemical reactions must occur in some context. They occur in the presence of other biochemical networks at physical locations within a cell. Quite often these networks are also subject to mechanical loading. Cellular adhesions represent a unique opportunity to marry biochemical processes with physical outputs, building the initial steps in constructing complete bio-chemical-physical models. In this work we explore two cases of cellular adhesions mediated by molecular clutches: (1) Adhesion to the extracellular substrate mediated via integrins and focal adhesions, and (2) Kinetochore adhesion to depolymerizing microtubules in metaphase and anaphase. Results from these studies lay a framework with which to conceptualize the mechanism of these processes, allowing further hypothesis testing, and ultimately future therapeutic benefit.

1.1 Molecular Clutches in Cell Motility and Mechanosensing

Cell motility is essential for an extensive range of physiological processes throughout the lifetime of an individual. In embryogenesis, migration of cells during gastrulation enables the formation of the three germ layers from which all tissues eventually develop. Formation of the nervous system involves the crawling of neuronal growth cones towards precise synaptic targets at distances far exceeding the diameter of

the cell body. Cell motility also has prominent roles during adulthood, functioning in homeostatic processes such as bone remodeling, inflammation, and wound healing. Motility is dependent on the construction of firm adhesions with the extracellular substrate that transmit contractile forces generated in the actin cytoskeleton to promote advance. Observations of the dynamics of cellular adhesions also suggest that cells utilize these sites of adhesion for probing the local mechanical environment, altering cellular morphology, motility, or fate in response to substrate stiffness. Therefore, understanding how this highly complex phenomenon operates has important implications for pathological processes such as tumor formation and metastasis.

1.1.1 Actin Dynamics in Motile Cells

A motile cell must make coordinated changes in shape oriented in the direction of desired motion. The shape of the cell is controlled mainly by the dynamics of actin, a 42 kDa protein that polymerizes to form structural filaments. In many cells, actin is utilized to form protrusive structures at the leading edge to probe the local environment for chemical and physical guidance cues.

In cells such as fibroblasts, these leading edge structures take the form of thin sheet-like networks, referred to as the lamellipodia. Lamellipodia consist of dense networks of actin filaments with individual filaments making an angle of ~70˚ with respect to each other, and ~35˚ with respect to the leading edge. Additionally, actin filaments in these networks preferentially orient their dynamic, barbed (plus) ends towards the direction of protrusion, utilizing actin polymerization to power the extension of the leading edge [1]. Regulation of this complex structure is mediated by a

number of factors, including dendritic nucleation factors such as Arp2/3, tethering proteins such as Ena/VASP, actin filament capping proteins, actin monomer sequestering factors such as thymosin β4, factors promoting filament disassembly at the minus end such as ADF/cofilin, and nucleotide exchange factors such as profilin [2].

In neurons, the extension of the axon is dependent on a specialized motile structure at the tip of the process called the growth cone. Growth cones not only possess lamellipodia, but are also dramatically enriched with filopodia, another type of actin protrusive structure. Filopodia, are long slender protrusions, typically 1-10 μm in length, consisting of long parallel bundles of ~15-20 actin filaments with their barbed ends oriented in the direction of protrusion. They have been observed to exhibit complex motions including extension, retraction, and stationary behavior, and when presented with chemical attractants, preferentially extend towards the source lending to the current view that filopodia have a role in neuronal pathfinding [3, 4]. Currently, it is believed that the dynamics of filopodial extension and retraction are also dependent on the underlying filament dynamics of actin polymerization in a similar manner to the actin networks of lamellipodia, though differences in the distributions of some factors have been noted [5, 6]. Factors implicated in regulating these dynamics include nucleation factors, such as members of the WASP family and formins, and minus end depolymerizing/severing factors, such as gelsolin [7].

Along with the underlying activity of individual actin filaments, the leading edge of motile cells exhibits a dramatic "retrograde flow" thought to be related to the generation of traction forces that pulls the cell forward. The first evidence that this retrograde flow consisted of actin filaments was a study using labeled actin monomers

demonstrating that a photobleached spot at the leading edge translocated towards the cell body [8]. Early work seeking to identify the driving force for this flow implicated the motor protein, myosin II, as a possible source, but subsequent work has also implicated possible roles for other myosins in some cases [9].

1.1.2 Integrins and Focal adhesions

In order to exploit and direct the forces generated by myosin motors, molecular clutches must be able to mechanically link the retrograde flow of F-actin to the extracellular environment via surface cell adhesion molecules (CAMs). The most commonly studied of these cytoskeletal-substrate coupling systems is the integrin-focal adhesion supramolecular complex found in a variety of cell types [10].

Integrins are heterodimeric transmembrane proteins that mediate divalent cation dependent cell-ECM interactions in all metazoa. Individual receptors of this family are composed of noncovalently associated αβ subunit pairs that are able to recognize multiple ligands. At present, 8 β subunits and 18 α subunits are known in vertebrates to interact in a restricted manner forming a total of 24 functional receptors. Interestingly, integrins dynamically switch from a low (inactive) to high (active) binding affinity state by agonists which regulate in an "inside-out" manner, or by ligand binding which regulate in an "outside-in" manner, leading to integrin clustering that increases the avidity of the receptor complex [11].

Upon activation and clustering, integrins recruit a wide array of proteins to their cytoplasmic domains forming a specialized structure known as the focal adhesion. These sites consisted of large heterogeneous protein networks which associate with

actin filaments or stress fibers making them ideal candidates for a molecular clutch complex [12]. Some of the structural proteins found at these sites include the cytoskeletal proteins tensin, vinculin, paxillin, talin, and α-actinin. Signaling molecules can also be found in these complexes and include tyrosine kinases, such as Src and focal adhesion kinase (FAK), serine/theronine kinases, regulators of small GTPases, tyrosine phosphatases, and additional enzymes including phosphoinositide-3 kinase (PI3K). As such, focal adhesions are thought of as not only as sites of mechanical linkage, but also as sites where biochemical signal transduction occurs [13, 14].

1.1.3 Motor-clutch motility

Mitchison and Kirschner first proposed motor-clutch motility in the late 1980s, suggesting that traction forces might be related to the phenomenon of F-actin retrograde flow observed in so many motile cell types. They postulated that by selectively coupling retrograde flow to the substrate (i.e. engaging a clutch), the cell could transfer the forces generated by myosin motors to the substrate [15]. This coupling would also have the effect of slowing the retrograde motion, allowing actin polymerization at the barbed end to push the leading edge forward. In this way, motor-clutch motility predicts an inverse relationship between retrograde flow and leading edge advance.

Perhaps the best evidence of motor-clutch motility comes from work with ApCAM, a cell adhesion molecule of the IgCAM superfamily found on *Aplysia* bag cell neurons [16, 17]. Anti-ApCAM coated beads applied to the surface of growth cones were found to couple to F-actin and exhibited retrograde flow [18]. Following this report, Suter et al. developed a restrained bead interaction (RBI) assay, utilizing a glass

microneedle to oppose the retrograde flow of coupled beads to simulate interactions with cellular substrates [19]. When they opposed the retrograde motion of the coated beads, they observed an abrupt increase in tension, indicated by the deflection of the restraining microneedle, accompanied with leading edge protrusion and central domain extension along the axis of bead interaction. When the restraint was removed during this period, the central domain nearly snapped back to its pre-interaction position, moving retrograde along with the interacting bead. They found that during strong coupling interaction, retrograde motion slowed on average by ~70%, as the central domain of the growth cone extended forward, providing some of the first evidence that resistance of F-actin retrograde flow can lead to leading edge advance.

In chapter 2 of this work, we present the first computational model of motor-clutch motility, incorporating a compliant substrate to predict how substrate stiffness might affect motor-clutch motility. We present some of the first evidence that retrograde flow and traction force generation are sensitive to substrate stiffness, using embryonic chick forebrain neurons plated on compliant polyacryamide gel substrates. The results of our work not only further strengthen the model of motor-clutch motility, but also suggest that it may be the basis of cellular mechanosensing.

1.2 Molecular Clutches in Mitosis

During mitosis, cells must appropriately segregate replicated chromosomes to accurately complete cell division. This process occurs in highly regulated phases using microtubules in conjunction with kinetochores, to exert forces that position and eventually pull sister chromosomes apart [20]. While the detailed mechanism by which

kinetochores maintain attachment to a dynamic microtubule is not known, extraordinary advances have been made in identifying the vital components that form mechanical linkages to the dynamic microtubule plus-end. Errors in this vital process lead to aneuploidy, resulting in birth defects and cancer [21]. Therefore, building a better understanding of kinetochore attachment while under load could ultimately lead to prevention or therapeutic treatments of disease.

1.2.1 Microtubules Dynamics and the Kinetochore

In prometaphase, a mitotic spindle assembles as the centrosome separates to form two asters of microtubules bound at their minus end, referred to as spindle poles [22]. As the spindle poles continue to separate, microtubules undergo dynamic instability, eventually capturing and binding to specialized sites that form on the centromeric portion of the chromosomes, called kinetochores [23, 24]. Spindle assembly is complete when chromosomes congress to the metaphase plate as a result of tension that develops from the sliding of anti-parallel microtubules under the influence of kinesin motor proteins [25]. Once the spindle assembly checkpoint has been satisfied, cohesion between sister chromatids is lost, and separation is at least partially achieved by the decrease in chromosome-pole distance, thought to be powered by depolymerization of kinetochore microtubules. How kinetochores maintain attachment under such dynamic conditions during metaphase and anaphase is currently a major area of study.

The kinetochore is an assembly of a large number of subcomplexes forming a trilaminar structure [23, 24]. The first layer, or inner kinetochore, takes shape during

mitotic entry on highly repetitive sequences of DNA and remains tightly associated with chromatin throughout mitosis. Many of these inner kinetochore proteins, such as CENP-A and CENP-C, are important for guiding the assembly of the next kinetochore layer, the outer kinetochore. The outer kinetochore, or outer plate, is not only the site of MT attachment, but is also known to be involved in tension sensing and the regulation of checkpoint. Furthermore, evidence suggests that it may also regulate MT dynamics. While there are a large number of essential kinetochore proteins, recent studies have identified two outer kinetochore complexes essential to maintaining attachment to chromosomes, (1) Ndc80 complex, and (2) Dam1 complex.

1.2.2 Ndc80 and Dam1 complexes

The Ndc80 complex is a set of highly conserved proteins thought to directly interact with microtubules [26-28]. In its complete form, Ndc80 complex is formed from two heterodimers, a MT-associating subcomplex of Ndc80 and Nuf2, and an inner kinetochore associating subcomplex of Spc24 and Spc25. The coiled-coil regions of each heterodimer associate to form a long, 57 nm rod-like structure capped by two globular head domains at each end.

Genetic analysis in yeast demonstrates the importance of this complex [29]. When deleted or mutated, kinetochore attachment during anaphase is lost leading to errors in chromosome segregation [30]. Depletion by siRNA also leads to a dramatic reduction in attachment leading to an extended prometaphase and eventual cell death [31, 32].

While the affinity of Ndc80 complex for tubulin is low, FRAP studies of whole kinetochores find very low recovery rates, suggesting that the Spc24/Spc25 globular head domain is firmly bound to the inner kinetochore [32]. Electron tomographic studies from vertebrate kinetochores suggest that in its native form, the Ndc80 complex is part of a fibrous mesh extending from the outer plate of the kinetochore [33]. Interestingly, recent work using cryoelectron microscopy has demonstrated that the MT-associating Ndc80/Nuf2 dimer interacts along protofilaments with an alternating strong-weak affinity, corresponding to interdimer and intradimer tubulin interfaces, respectively [34]. The coiled-coil portion of the Ndc80/Nuf2 dimer is observed to have a flexible kink, bending with a range of ~ 120 degrees [29].

Another important complex demonstrated to make direct contacts with MTs is the Dam1 (or DASH) complex identified in budding yeast [35]. Each subunit of Dam1 is a heterodecamer, 16 of which oligomerize *in vitro* to form a ring around MTs. Loss or mutation of any one of the complex components leads to loss of kinetochore attachment or inability to biorient in metaphase [36, 37]. Due to the stoichiometry and dimensions, the ring complex is thought to diffuse along the length of MTs, and has been proposed to harness protofilament curling during MT depolymerization to perform useful work [38]. Dam1 has been shown to follow and accumulate at the depolymerizing plus-end MTs *in vitro* systems [39]. Furthermore, when under tension, the Dam1 ring has been demonstrated to promote polymerization, suggesting a role in tension-dependent rescue of MTs [40].

While this mechanism has been the subject of much theoretical study [41-43], new results showing that single Dam1 complexes diffuse along the MT-lattice bring in

question the need of the ring structure [44]. Rather than transducing the mechanical curling of protofilaments from the end of the depolyermizing MT, diffusion of single Dam1 complexes suggest a biased diffusion model where the complex end-tracks due to affinity with the MT surface [45, 46].

1.2.3 The Hill Sleeve Model of Kinetochore End-tracking

One of the first mathematical models of how kinetochores might be mediating attachment to depolymerizing microtubules came from Hill [45]. In Hill's model, the kinetochore consists of a thermally driven "sleeve" that encircles the microtubule. Tubulin binding sites line the inner circle of the sleeve, and are spaced such that all tubulin dimers over a 40 nm thickness would have an available site to associate with (~65 sites). Since there is affinity between tubulin and the binding sites, the system will seek to minimize the free energy by maximizing the overlap between the MT and sleeve. As the MT inserts further into the sleeve, progressively more bonds must be broken to allow the MT to step into the next favorable position. Thus, a linearly increasing potential energy barrier due to the breaking of bonds counteracts MT insertion, setting up a steady-state position about which the system fluctuates. As tubulin units are lost due to depolymerization, the Hill sleeve moves to maintain this steady-state insertion, thus tracking with a depolymerizing MT. Based on theoretical grounds, Hill finds that a kinetochore sleeve could maintain attachment up to 15 pN of load.

Since Hill's proposed sleeve model, many advances have altered our thinking of how kinetochore attachment might work. The identification of molecular clutches that

independently associate and dissociate from tubulin contrasts Hill's idea of a crystalline sleeve, where all bonds act in concert. In addition, recent cryo-electron microscopy studies show that the kinetochore is fairly amorphous rather than crystalline [47]. Furthermore, the recent EM results argue against the close apposition of a mechanically rigid sleeve immediately adjacent to the MT, limiting the free exchange of tubulin required for MT dynamics during mitosis.

In chapter 3 of this work, we develop a new model for kinetochore motility to incorporate characteristics of recently identified molecular clutches that mediate kinetochore attachment. We demonstrate that a kinetochore of independently acting clutches tracks in much the same manner as predicted by Hill, but that it can be greatly improved by allowing the linkages to be mechanically compliant. In addition, we find a potentially important role for MT-lattice diffusion of clutches, and for preferential binding of clutches at interdimer interfaces, rather than intradimer interfaces.

- CHAPTER 2 -
TRACTION DYNAMICS OF FILOPODIA ON COMPLIANT SUBSTRATES

The contents of this chapter were published as "Traction Dynamics of Filopodia on Compliant Substrates." (Chan and Odde, Science 2008)

2.1 Abstract

Cells sense the environment's mechanical stiffness to control their own shape, migration, and fate. To better understand stiffness sensing, we constructed a stochastic model of the "motor-clutch" force transmission system, where molecular clutches link F-actin to the substrate and mechanically resist myosin-driven F-actin retrograde flow. The model predicts two distinct regimes: (1) "frictional slippage" with fast retrograde flow and low traction forces on stiff substrates, and (2) oscillatory "load-and-fail" dynamics with slower retrograde flow and higher traction forces on soft substrates. We experimentally confirmed these model predictions in embryonic chick forebrain neurons by measuring the nanoscale dynamics of single growth cone filopodia. Furthermore, we experimentally observed a model-predicted switch in F-actin dynamics around an elastic modulus of 1 kPa. Thus, a motor-clutch system inherently senses and responds to the mechanical stiffness of the local environment.

2.2 BACKGROUND

Recent work has demonstrated the importance of substrate stiffness on cell motility, morphology and fate [48]. For instance, fibroblasts display a behavior known as durotaxis, preferentially migrating towards regions of higher stiffness [49]. Softer substrates have been shown to promote branching in primary mouse spinal cord neurons while suppressing the growth of associated glia [50, 51]. A recent study has also shown that mesenchymal stem cell fate can be determined by the stiffness of the culture substrate, a phenomenon that requires actomyosin contractility [52]. While the importance of actomyosin and substrate adhesions are well appreciated, it is not clear how these components work together to sense and respond to the stiffness of the local environment.

One way cells are thought to probe their environment is through the generation of traction by a "motor-clutch" mechanism where cells utilize molecular clutches to physically link F-actin to the extracellular substrate [15]. By creating this physical coupling, cells are thought to create a frictional slippage interface that transmits traction forces and slows F-actin retrograde flow, allowing actin polymerization to advance the leading edge [53-55]. If cells use the motor-clutch system to probe their mechanical environment, we wondered how this system would be influenced by substrate stiffness. Here we use an integrated computational/experimental approach by simulating key components of motor-clutch motility on compliant substrates to determine how such a system might behave. Then, we confirm model predictions showing that motor-clutch motility explains many aspects of neuronal growth cone filopodia dynamics as a function of substrate stiffness.

2.3 METHODS

2.3.1 Computational Modeling of Stochastic Motor-Clutch Motility on Compliant Substrates

A computational model of motor-clutch motility over compliant substrates was developed and run in MATLAB (The MathWorks) as described below.

Model Assumptions

Briefly, the model simulates a filopodium consisting of myosin motors, an F-actin bundle, molecular clutches, and a compliant substrate. The current model assumes that myosin motors and the F-actin bundle are relatively stiff compared to the molecular clutches and the compliant substrate. In addition, while focal adhesions consist of a complex of proteins [10, 56], more recent work suggests that focal adhesions tend to undergo shearing at specific proteins within the complex [53, 57]. Thus, we simplify molecular clutches to a single, Hookean spring, allowed to fail at one point (e.g. at the F-actin-clutch interface). However, the model behavior does not depend on the specific site of failure, and if there are potential failure sites in series they will tend to fail at the weakest point. It is this weakest point that is represented in the model, and in principle this failure point could lie outside the cell. In addition, as tension develops within an engaged molecular clutch, we assume that the effective dissociation rate, k_{off}*, increases exponentially according to a Bell Model [58],

$$k_{off}^{*} = k_{off} \cdot e^{F_{clutch}/F_b} \qquad \text{(Eq. 2-1)}$$

where k_{off} is the unloaded dissociation rate of the molecular clutch from the actin bundle, F_b is the characteristic bond rupture force, and F_{clutch} is the tension within an individual clutch given by,

$$F_{clutch(i)} = \kappa_{clutch} \cdot \left(x_i - x_{sub} \right) \quad \text{(Eq. 2-2)}$$

where κ_{clutch} is the Hookean spring constant of molecular clutches, x_i is the position of the molecular clutch, and x_{sub} is the position of the substrate. We also treat the compliant substrate as a linear, Hookean spring since strains are relatively small. Furthermore, we assume that myosin motors will slow when acting against an elastically loaded substrate according to a linear force-velocity relation given by

$$v_{filament} = v_u \left(1 - \frac{\kappa_{sub} \cdot x_{sub}}{F_{stall}} \right) \quad \text{(Eq. 2-3)}$$

where v_u is the unloaded sliding velocity of myosin and F_{stall} is the total myosin motor stall force of the system defined as

$$F_{stall} = n_m \cdot \hat{F}_m \quad \text{(Eq. 2-4)}$$

where $\hat{F}_m$ is the force required to stall the activity of one myosin motor and n_m is the number of motors in the system. We ignore the effects due to inertial forces within the filopodium since the Reynolds number is much less than one ($Re \approx 10^{-6}$). We also ignore the viscous forces in the substrate since the experimentally observed viscoelastic relaxation time (<10 ms; Fig. 2-9) is shorter than the characteristic event time.

Model Methodology

For each time step in the Monte Carlo simulation (5-10 ms), molecular clutches are first allowed to associate with the F-actin bundle according to the association rate

constant, k_{on}. Next, engaged clutches are tested for disengagement according to their effective dissociation rate (Eq. 2-1). Once the final spring network has been resolved, the forces are balanced to solve for the final position of the substrate, x_{sub}, according to

$$x_{sub} = \frac{\kappa_{clutch} \cdot \sum_{i=1}^{n_{eng}} x_i}{\kappa_{sub} + n_{eng} \cdot \kappa_{clutch}} \quad \text{(Eq. 2-5)}$$

where n_{eng} is the number of engaged molecular clutches. From the position of the substrate, we determine the amount of force against which the myosin motors are working, and calculate the velocity of F-actin retrograde flow, $v_{filament}$, according to Equation 2-3. Once the new F-actin retrograde flow velocity has been determined, engaged clutches are displaced by a distance $\Delta x = v_{filament}\Delta t$ and the force along each molecular clutch calculated to determine the effective F-actin-clutch off rates for the next time step. The new F-actin retrograde flow velocity also allows us to determine the velocity of the leading edge of the filopodium, v_{edge}, determined as

$$v_{edge} = v_{poly} + v_{filament} \quad \text{(Eq. 2-6)}$$

where v_{poly} is the polymerization velocity of F-actin. The simulation is allowed to run for 60,000 time steps (300 s) to ensure the simulation has reached steady-state before statistics are calculated.

Model Parameters

Values and the sources for the model parameters are summarized in Table 2-1. Parameters that are not well established have been estimated using our experimental data. Note that some of the parameters are drawn from a variety of cell types and systems, although some parameters, such as the myosin stall force, are observed to be

narrowly constrained across a wide range of systems. In many cases we could cite a large number of studies, but for simplicity we cite only one or two representative studies.

2.3.2 Transfection and Cell Culture

Embryonic chick forebrain neurons (ECFNs) were transfected with EGFP-actin plasmid (kindly provided by Paul Letourneau) by *in ovo* electroporation [59]. Briefly, embryonic day 5 chick embryos were exposed by removing the eggshell above the air pocket of the inner membrane. Then, to separate the inner membrane from the vasculature, 50 μl of PBS was pipetted over the inner membrane and allowed to drain into the egg by making a small incision. Following this, the vitelline membrane was cleared to the side and the embryo positioned to allow access to the forebrain. Next, ~5-10 μg of plasmid was injected into the right hemisphere of the forebrain with a Picospritzer II (Intracell, Frederick, MD). CUY610P4-4 2mm platinum electrodes were then positioned to straddle the treated hemisphere, and five square wave pulses (50 ms pulse, 950 ms rest at 50 V) delivered by a CUY-21 electroporator (Protech, San Antonio, TX). Following this procedure, eggs were sealed with tape and placed in an incubator at 39 °C for another two days.

At E7, transfected ECFNs were harvested as previously described [60] with the exception that only the transfected hemisphere was dissected and dissociated in 5 ml of media. Cultures were then plated on prepared polyacrylamide gel (PAG) substrates and maintained in F12 media supplemented with 5% fetal bovine serum, 5% chicken serum, 100 units/ml penicillin, 100 mg/ml streptomycin, 250 ng amphotericin B/ml, and 20

mM HEPES, adjusted to pH 7.4 (all components from Gibco). To allow sufficient time for growth cone development, all cultures were incubated overnight in an air incubator (Forma Scientific) at 37 °C prior to experimentation.

2.3.3 Preparation and Characterization of PAGs

Polyacrylamide gel (PAG) substrates were fabricated according to published procedures [61, 62]. Briefly, 35 mm culture dishes with No. 0 coverglass bottoms (MatTek#: P35G-0-20-C) were etched with a 15 min treatment of 0.1 N NaOH and silanized by treatment for 15 min with 3-aminopropyl-trimethoxysilane. Following a series of washes in deionized (DI) H_2O, culture dishes were treated with a solution of 0.5% glutaraldehyde. After 30 minutes in solution, the culture dishes were thoroughly washed in DI H_2O and allowed to dry vertically.

Next, PAG prepolymer was prepared in a sterile environment by combining the appropriate amounts of 40% acrylamide (3-8% by volume), 2% bis-acrylamide (0.04%-0.1% by volume), and 1 M 4-(2-Hydroxyethyl)piperazine-1-ethanesulfonic acid (HEPES) buffer at pH 8.5. This solution was then degassed for 30 minutes followed by the addition of 0.2 μm crimson fluorescent beads (Invitrogen #: F-8806). Initiation of polymerization occurred by the addition of ammonium persulfate (10% w/v solution, Biorad) and N,N,N,N-tetramethyl ethylenediamine (TEMED, Biorad). Immediately following initiation, the prepolymer was pipetted onto the previously treated coverglass and a separate round coverglass (No. 1, 12mm diameter; Fisher) was overlayed onto the gel droplet to promote spreading. The entire apparatus was then inverted to allow the settling of fluorescent beads near the upper surface of gel surface. After allowing the

dishes 30 min to complete polymerization, the surface of the PAG was exposed by removal of the overlaying coverglass and prepared for surface treatment by washing thoroughly with 50 mM HEPES buffer. To promote cell adhesion, PAGs were incubated in 0.5 mg/ml polyethyleneimine (PEI) at 4 °C overnight. Prior to plating, PAGs were washed in PBS, sterilized under UV for 15 minutes, and incubated in culture media for 1 hr at 37 °C.

PAG stiffness was determined using a microsphere indentation method similar to previously described methods [61, 62]. In order to minimize indentation depths and maintain material linearity, smaller (150-250 μm), less dense, glass microspheres (PolySciences, Inc.) were used as probes instead of the previously published use of 300 μm steel spheres. In general, sphere sizes were matched to keep indentations to ~15% of the gel thickness (total gel thickness = 40-100 μm). Indentations were calculated by measuring the sphere radius, R, and radius of contact, r, via microscopy by centering a glass sphere in the field of view and bringing the glass sphere and upper surface of the gel into focus, respectively. From these measurements, indentation, δ, was calculated as follows

$$\delta = R - \sqrt{R^2 - r^2} \qquad \text{(Eq. 2-7)}$$

Using this value, the PAG's Young's Modulus, E, was estimated by Hertzian theory according to

$$E = \frac{3\left(1-\nu^2\right)f}{4R^{1/2}\delta^{3/2}} \qquad \text{(Eq. 2-8)}$$

where ν is the Poisson ratio of the hydrogel (ν=0.3), and f is the buoyancy corrected force exerted by the spherical probe [63].

2.3.4 Live Cell Imaging

Traction force dynamics were visualized via wide-field epifluorescence fluorescence microscopy using a 1.49 NA 60x Planapo TIRF oil immersion objective mounted on a Nikon TE200 inverted microscope equipped with a dual channel FITC-TRITC filter set with single band exciters (Chroma#: 52004v2). Images were captured at 0.1-3 s time intervals using a 14 bit, cooled CCD digital camera (CoolSnap HQ2, PhotoMetrics) controlled by MetaMorph software (Universal Imaging). Typical exposure times for recording fluorescent bead images were 30-50 ms. Time-lapse recordings for GFP-actin retrograde flow measurements were acquired at 1 s intervals with 250-300 ms exposure times on the same apparatus using a single channel ET-GFP filter set (Chroma#: 49002). Image sequences collected to determine whether integrins played a role in ECFN growth cone motility were collected at 30 s intervals in the presence of 100 μM monoclonal anti-chicken β1 integrin non-activating IgG antibody (Sigma#: I8636). To determine whether myosin II motors contributed to F-actin retrograde flow, time-lapse images were recorded at 1 s intervals in the presence of 100 μM blebbistatin (BIOMOL International#: EI-315). F-actin retrograde flow measurements were also recorded using transmitted microscopy with typical exposures of 50 ms at intervals of 1 s. Experiments to estimate the amount of surface tension generated by single ECFNs were performed by recording pre- and post-trypsinized images on the same microscope using a custom modified MP-285 micromanipulator (Sutter Instruments) as a stage along with a single channel TRITC filter set (Chroma#:

31002). All experiments were performed in cell culture media in an enclosed environment maintained at 37 °C.

2.3.5 Image Analysis

Fluorescent Marker Bead Tracking and Traction Force Dynamics

In order to measure high temporal resolution traction force dynamics, we developed a custom marker bead tracking algorithm in MATLAB. Briefly, the background for each frame in the image stack was determined and subtracted. To trace each marker bead through time, each frame was segmented using a Sobel edge detector (edge.m, Image Processing Toolbox), and further processed to highlight and determine the trackable beads in the field of view. Overlapping segmented regions from one frame to the next were assumed to be from the same marker bead while the user identified segmented regions having no overlap in the next frame. Next, the algorithm cropped around identified marker beads, removed further noise, and fit a 2D Gaussian to determine the position of the marker bead with sub-pixel resolution. Stage drift was accounted for by measuring the position of 5-10 marker beads within a reference region far away from the influence of cells, measuring their motion, and subtracting their motion from the trace bead positions. Traces along filopodia were then rotated such that all motion was along the x-axis and the bead rest position at the origin, thus defining loading or failing motions as negative or positive movements along the x-axis, respectively.

In order to validate our bead tracking procedure, we estimated the precision of the algorithm using image stacks (~181 frames) of marker beads embedded within

PAGs from reference regions far away from the influence of cells (Figure 2-1a). Throughout the duration of these movies, reference beads should not show motion, making them excellent objects to test for algorithm noise. We tracked these beads and calculated stage drift as the mean vector of frame-to-frame bead motion (Figure 2-1b). These values were then subtracted from the fitted bead positions to remove drift. Following this procedure, the mean position of each reference bead through the duration of the image stack was determined. Next, we calculated the frame-to-frame deviation of the fitted position from the mean position of every reference bead and used these values to calculate the rms displacement from the mean position (Figure 2-1c). Using this procedure, we estimated that our algorithm has an r.m.s. uncertainty in the bead position of 5.2 nm.

Estimate of maximal filopodial traction force and substrate spring constant

To constrain the range of values for the motor number parameter, we estimated the maximum force exerted by filopodia by applying the *Cerruti solution* [64] for a point force acting tangential to a linear elastic half-space (Figure 2-2a). When simplified to one dimension, the *Cerruti solution* is given by

$$T = \frac{\pi E \delta}{1+\upsilon} U \qquad \text{(Eq. 2-9)}$$

where T is the magnitude of the applied point force, E is the Young's modulus of the material, δ is the distance between the point of force application and the marker bead, v is the Poisson's ratio of the material, and U is the strain of the substrate at the location of the marker bead. Since δ is not readily apparent in our system, we use the special case where two marker beads fall along the axis of a filopodium (Figure 2-2b). We note

that beads more than a few micrometers from a cell do not exhibit detectable displacement, indicating that δ is on the order of less than a micrometer. In this case, the force can be estimated independent of δ as

$$T = \frac{\pi E}{1+\upsilon}\left(\frac{U_1 U_2 L}{U_1 - U_2}\right) \qquad \text{(Eq. 2-10)}$$

where U_1 and U_2 are the respective strains of the first and second marker beads, and L is the distance between the two marker beads. Furthermore, δ can be estimated by

$$\delta = \frac{U_2 L}{U_1 - U_2} \qquad \text{(Eq. 2-11)}$$

In other words, the *Cerruti solution* is applied for both beads under the assumption that the same force acts on them, so that there are two equations and two unknowns (i.e. δ is eliminated to solve for T). From 18 bead traces of force dynamics where we could clearly see two beads influenced by a single filopodium (Figure 2-2c-d), we estimated the maximum force exerted by ECFN growth cone filopodia to be 110 ± 25 pN (SEM). Furthermore, we find that δ is approximately 150 ± 30 nm (SEM), indicating that the point of contact is generally very close to marker beads showing observable dynamics. Note that because we estimate the filopodial force, T, and marker bead distance, δ, from the maximum displacements in these bead traces, these estimates of T and δ may be higher/lower than average, respectively.

From equation 2-9, we can estimate the substrate spring constant, κ_{sub} as a function of Young's modulus of the PAG, E, using the estimate of δ as

$$\kappa_{sub} = \frac{\pi E \delta}{1+\upsilon} \qquad \text{(Eq. 2-12)}$$

Since our estimate of δ has a relatively large error and is biased towards smaller values, we may also be underestimating κ_{sub}. In order to test how well our model predictions of F-actin retrograde flow fit with our experimental measurements, we introduce a fitting parameter, Δ, to account for our underestimate of κ_{sub}. Using this fitting parameter (Δ=277 nm), we find that our experimental findings do not significantly deviate from our modeling predictions (p=0.09).

Measuring F-Actin Retrograde Flow Within ECFN Growth Cone Filopodia

Briefly, we constructed kymographs along individual ECFN growth cone filopodia showing trackable fluorescent features using MetaMorph. From these kymographs, GFP-actin features showing retrograde motion appear as diagonal streaks. To measure the velocity of these features, we constructed a custom cross-correlation algorithm in MATLAB analogous to published methods [65]. Fluorescent "streaks", resulting with retrogradely moving fluorescent F-actin features inside of filopodia, were manually selected by the user and used to create a template and shifted window, shifted by one time interval along the temporal dimension. To further enhance features, a background vector was calculated as the mean fluorescence intensity along columns, and subtracted from the region of interest. A 2D cross-correlation was then performed along the spatial dimension, and a 1D Gaussian fitted to the correlation coefficient profile yielding the velocity of the feature.

To validate our F-actin flow-tracking algorithm, we created synthetic image stacks of retrogradely flowing F-actin features along single filopodia (Figure 2-3). We started by creating a fine mesh (5 nm) image of a 4 μm long filopodium with a 250 nm

bright (2x) feature (Figure 2-3a). Next, we added a linearly decreasing background to simulate light scatter from growth cones or thicker regions of the cell commonly found in our experimental images. This fine mesh image was then convolved with a theoretical point spread function and binned creating a coarse-grained image with pixel sizes of 100 nm (Figure 2-3b). Next, to this coarse-grained image we added a constant background signal along with Gaussian-distributed noise to obtain signal-to-noise levels similar to the experimentally obtained images of filopodia (Signal: 800 intensity counts; Background: 600 +/- 200 (S.D.) intensity counts, Figure 2-3c). We repeated the above procedure, moving the F-actin feature at the appropriate velocity each time, creating an image stack representing 30 s of synthetic data. We call this procedure "model-convolution" and have used it to validate image processing in other studies of cytoskeletal dynamics [66-70]. From these synthetic image stacks, we created kymographs along filopodia using MetaMorph software (Figure 2-3d). We then analyzed these kymographs using our flow-tracking algorithm and compared the measured rates to the known, simulated values (Figure 2-3e-f). These tests indicate that the tracking algorithm achieves agreement to within 5% of the actual flow rates that were set in the simulation.

Estimation of ECFN Surface Tension

In order to estimate the surface tension generated by individual ECFNs, we imaged paired stressed (pre-trypsinization) and relaxed (post-trypsinization) marker bead images of individual ECFNs with at least 20 μm of space between cells. A Sobel edge detector was used to segment the paired images and stress and unstressed regions paired

if they were mutually exclusive nearest neighbors. Next, 2D Gaussians were fit to each bead and the drift removed using an estimate from a region containing 5-10 beads far away from any cells. Then, the distances between paired stressed-unstressed regions were calculated. In order to estimate the scaled stored elastic energy for each bead, we multiplied the summed square strains by a normalized stiffness as follows

$$Energy_{Stored} = \frac{E_{PAG}}{E_{norm}} \sum (strain)^2 \qquad \text{(Eq. 2-13)}$$

where E_{norm} was the stiffness of the softest PAG in the experiment (730 Pa). Due to the limits of force sensitivity in the stiffer PAGs, we excluded strains from softer gels with scaled energies lower than 710 nm^2. Strains from bad pairings were identified by the user and also excluded from the calculation. From this, we estimated the scaled surface tension generated by the cell (dimensionless) by normalizing the scaled stored energy (units of $pixels^2$) by the area of the region containing the ECFN (units of $pixels^2$).

2.3.6 Statistical Analysis

Student's t-tests and regression analysis were performed using the "Data Anaylsis" toolpak add-in in Excel (Microsoft). Each bead motion trace for the traction dynamics analysis within a given substrate stiffness was treated as an individual event. F-actin retrograde flow velocities from individual filopodia were also treated as individual events. For the above tests, we treated individual cells as individual events for the surface tension analysis. Finally, to test whether the experimental findings for retrograde flow as a function of stiffness were significantly different from the model predicted behavior, we calculated the number of SEMs a given experimental point deviated from simulation and determined the probability that that point significantly

deviated from the model prediction. The overall p-value for the test of model behavior was then estimated using the lowest p-value multiplied by the number of tests for deviation.

2.4 Results

2.4.1 Simulated Motor-Clutch Dynamics on Compliant Substrates

In order to address this question, we first constructed a stochastic physical model of the motor-clutch hypothesis, treating molecular clutches and the substrate as simple, Hookean springs (Figure 2-4a). At every time step, n_m myosin motors drive retrograde flow by exerting a force, F_M, on an F-actin bundle. Next, individual molecular clutches are allowed to reversibly engage the F-actin bundle with rate constants k_{on} and k_{off}. Clutches that successfully engage will build tension with spring constant κ_c, as they are stretched by retrograde motion of F-actin. Tension along engaged clutches increases their off-rate constant, k_{off}*, exponentially according to Bell's Law [58], with characteristic breaking force, F_b. Tension in the engaged molecular clutches sums to a traction force that must be balanced by tension and deformation in the compliant substrate with spring constant κ_{sub}. Myosin motors work against this load force, slowing their motor sliding velocity according to a linear force-velocity relation. Finally, actin polymerizes at the plus-end of the F-actin bundle with constant velocity to counter retrograde flow and maintain the F-actin bundle. For simplicity we ignored tension-dependent strengthening of adhesions, as has been reported in some cases [71, 72], as this effect can be added later to increase the model sophistication and complexity, if necessary.

When we simulated the motor-clutch system on compliant substrates, we observed the emergence of two distinct traction force dynamics (Figure 2-4b). On stiff substrates, molecular clutches engage the F-actin bundle but abruptly disengage as lack of compliance in the substrate results in a rapid building of tension within engaged clutches that drastically shortens F-actin-clutch interaction life-times. In this case, the F-actin bundle is constantly slipping from the point of contact at a roughly constant velocity. We describe this dynamic as "frictional slippage", a behavior that has been previously noted on stiff glass substrates [53, 73, 74].

On soft substrates, substrate compliance slows the rate at which tension builds along individually engaged clutches. This prolongs F-actin-clutch interaction times with most clutches remaining engaged to the F-actin bundle at early times in the cycle (Figure 2-4b). During this time, there is little relative motion between the F-actin bundle and substrate as tension slowly develops within the substrate. Due to this lack of resistance, myosin motors work near their unloaded sliding velocity, leading to high rates of F-actin retrograde flow and a slight retraction of the leading edge. As the substrate strains and greater tension builds, clutches largely remain engaged due to sharing of the mechanical load amongst engaged neighbors. This provides significant resistance to the motor force, substantially slowing retrograde flow. Eventually, the load becomes so great that the stochastic loss of one clutch leads to a cascading failure event, where the unsupportable load shifts progressively to remaining bonds, further destabilizing the F-actin-clutch interaction. This quickly leads to an abrupt coupling failure where all clutches rapidly disengage, consequently unloading the substrate, causing it to snap back to its initial rest position. Thus, computational modeling of

motor-clutch motility on soft substrates predicts the natural emergence of an oscillatory "load-and-fail" traction force dynamic characterized by protracted periods (~10-100 seconds) of increasing tension followed by an abrupt coupling failure (Figure 2-4b, Figure 2-4c).

In addition, simulations predict that these substrate stiffness-dependent changes in clutch dynamics lead to significant differences in F-actin retrograde flow rates and the mean traction forces exerted on soft versus stiff substrates. On stiff substrates, short-lived F-actin-clutch interactions create a "molecular friction" [75], where only a few clutches are engaged at any given time point. Lower average clutch numbers limit the total tension developed along engaged clutches, resulting in lower mean traction forces and higher rates of retrograde flow. On the other hand, load-and-fail dynamics on soft substrates results in higher numbers of engaged clutches on average, increasing the total tension developed along clutches, leading to slower retrograde flow velocity and greater transmission of traction forces (Figure 2-4). As the substrate becomes softer still, modeling predicts a slight increase in retrograde flow rate along with a slight decrease in traction forces (Figure 2-4d). This occurs as the system spends a greater fraction of the time weakly loaded, resulting in longer times to generate sufficient tension to significantly resist the myosin motors. Thus, a motor-clutch system is predicted to exhibit substrate stiffness-dependent changes in clutch dynamics that result in higher retrograde flow rates with lower traction forces on stiff substrates, and lower retrograde flow rates with higher traction forces on soft substrates.

Simulation of the motor-clutch system on compliant substrates suggested that transition from load-and-fail dynamics to frictional slippage was a robust feature,

occurring in many regions of parameter space. To demonstrate this effect, we varied the unloaded clutch off-rate k_{off} by a factor of 3 (Figure 2-5). As expected, increasing k_{off} by a factor of 3 caused clutches to frequently disengage from the actin bundle. This leads to increased retrograde flow throughout the entire relevant stiffness, as frictional slippage dominates the system (Figure 2-5a). On the other hand, decreasing k_{off} by a factor of 3 reduces the frequency of clutch disengagement, leading to stalling of retrograde flow on soft substrates. This abruptly switches to frictional slippage once the substrate stiffness become great enough such that strain occurs mostly within engaged molecular clutches. Adjusting other parameters in the model can compensate for these effects. For example, in the case of a stalling system, reducing the number of clutches reduces the ability of the system to resist myosin motors, leading to a recovery of load-and-fail dynamics (Figure 2-5b). In a similar vein, incorporating more clutches into a system exhibiting frictional slippage can slow retrograde flow, allowing clutches to work in tandem, leading to load-and-fail dynamics (Figure 2-5c).

2.4.2 Experimental Tests of Motor-Clutch Dynamics on Compliant Substrates

To test these model predictions, we used green fluorescent protein (GFP)-actin transfected embryonic chick forebrain neurons (ECFNs) plated on soft (260-730 Pa), or stiff (1.3-57 kPa) polyacrylamide gel (PAG) substrates coated with polyethyleneimine (PEI) as an adhesion promoter. Compliant PAGs embedded with 200 nm diameter fluorescent fiduciary marker beads allow the visualization of traction forces as deflections of beads from their rest position [61, 62, 76]. Using dual-channel

epifluorescence imaging in combination with a computational bead tracking algorithm, we visualized F-actin dynamics in growth cone filopodia and deflections of underlying marker beads to directly observe traction force transmission dynamics at 1-10 Hz frame rates.

With this system we find that neurons exhibit a wide variety of region specific traction force dynamics on compliant PAGs (Figure 2-6). Under the cell body and axon, neurons exert relatively small, but detectable, randomly fluctuating tractions, as visualized by the somewhat random trajectories of embedded substrate marker beads. The central region of the growth cone exhibits similar random force fluctuations, except with larger magnitude than axons or cell bodies, consistent with the growth cone being the major motile apparatus and force integrator of neurons. In these cases the direction of the force also fluctuates randomly. In contrast, growth cone filopodia frequently displayed large, unidirectional bead deflections several times greater in magnitude than other regions of the neuron. We also observed similar behavior from filopodia originating from cell bodies of early stage neurons (data not shown), but have excluded them from this analysis, as we are interested in traction dynamics near the motile growth cone.

Neuronal growth cones are known to utilize a number of adhesion molecules for successful adhesion and motility including integrins, NCAMs, and L1 [77-83]. To determine whether ECFN growth cones use the integrin-mediated coupling pathway during their motility over PEI-coated PAGs, GFP-actin transfected ECFNs were cultured on PAGs and imaged for 15 min prior to addition of 100 μM anti-β1 integrin antibody (Figure 2-7a). Within 30 minutes of treatment, we observed dramatic

retraction of growth cones, while cell bodies and axons remained intact (Figure 2-7b). This indicates that integrin coupling plays a significant role in ECFN growth cone adhesion and motility. In contrast, neuronal cell bodies and axons may utilize additional molecules to maintain attachment to PEI-coated PAGs.

When we examined the detailed time evolution of filopodial traction forces, we found that substrate embedded marker beads deflected inwardly toward the growth cone and would occasionally snap back towards their rest position, indicative of the load-and-fail behavior predicted by the motor-clutch model when the substrate is soft (Figure 2-8a; Appendix A). A time projection through the movie shows that filopodia exert unidirectional tractions along the filopodium axis (Figure 2-8b). A kymograph along the axis of the filopodium shows that filopodium exert traction forces with load-and-fail dynamics similar to that predicted by the model, with cycle times on the order of tens of seconds (Figure 2-8c). Interestingly, on occasions where more than one filopodium within a growth cone exerted observable tractions, we found substantial variation in both the amplitude and frequency of load-and-fail events. This suggests that cells likely have stochastic fluctuations or spatial gradients in one or more motor-clutch parameters, leading to variable dynamics amongst individual filopodia.

To further characterize the abruptness of failure events, we imaged ECFN growth cones at 100 ms time resolution. At this temporal resolution, we noted that failures still occurred within one time step with no observable blurring, suggesting that viscous forces within the substrate can be ignored at time scales much less than 100 ms, in agreement with model assumptions and the simulation time step (10 ms) (Figure 2-8d, Figure 2-9). Furthermore, loading often occurred immediately (less than 100 ms)

following failure events, demonstrating that failures were due to transient clutch disengagement, rather than filopodia retracting from the region entirely.

From these traces and movies, it became clear that traction force dynamics could vary significantly from one filopodium to the next. Even within a given growth cone, we observed variable dynamics between individual filopodia. This led us to believe that filopodium composition can vary dramatically, consistent with other reports [84, 85]. In order to characterize the frequency of failure events for a given substrate stiffness, we had to set criteria to identify failure events despite these variable dynamics. To resolve this, we normalized each marker bead trace by its maximum displacement (Appendix A, second column) and calculated the distribution of bead displacements from one time point to the next (i.e. during one time interval of 1 s) (Appendix A, third column). Averaging these single time increment histograms within a given stiffness condition revealed roughly similar distributions (Figure 2-10a-c). In all stiffness conditions, the frequency of positive single time increments above 30% of the maximum displacement dropped off abruptly, indicating the presence of infrequent failure events. Using this criterion as identification for the infrequent and large failure events, we calculated the frequency of failures as a function of stiffness. As predicted by the model, the frequency of failure events significantly increased with increasing substrate stiffness ($p<0.03$, Figure 2-10d). Together, these data reveal that filopodia exert traction forces with load-and-fail dynamics predicted by a stochastic model for the motor-clutch system on a soft substrate.

To test the model prediction that retrograde flow rate increases with increasing substrate stiffness, we tracked fluorescent GFP-actin features from growth cones of

transfected ECFNs on PAG substrates imaged via epifluorescence (Figure 2-11a). As growth cones crawl, polymerization at the leading edge stochastically gives rise to a fluctuating number of GFP-labeled actin filaments that constitute the filopodial F-actin bundle, creating alternately bright and dark F-actin features that can be quantitatively tracked via digital image analysis.

As with other motile cell types, the peripheral zone of growth cones exhibits rapid retrograde flow of polymerized actin (Figure 2-11b). Furthermore, GFP-actin features were never observed to move anterogradely (out of n=922 features tracked), demonstrating that the major point of coupling failure lies between the F-actin-substrate interface, rather than between the myosin-F-actin interface. Creating kymographs along filopodia reveals motion of F-actin features that were tracked utilizing a cross-correlation algorithm. Using this method, we found that retrograde flow was significantly slower on soft substrates ($p<0.0001$, Figure 2-11c). Filopodia on substrates from 730-1300 Pa showed high sensitivity to stiffness, abruptly increasing their retrograde flow rates as substrate stiffness increased (Figure 2-11d, blue region). Once substrate stiffness exceeded a critical value of ~1300 Pa, retrograde flow rates became insensitive to stiffness, having a mean velocity of ~110 nm/s. Thus, measuring the retrograde flow rate over a range of substrate stiffness revealed a trend not significantly different from that predicted by simulation ($p=0.09$) and suggests that ECFN growth cone filopodia may transition from load-and-fail dynamics to frictional slippage around 1 kPa (Figure 2-11d).

In order to test model predictions on even softer substrates, we attempted to culture ECFNs on extremely soft PAGs (84 Pa). We found that these cultures tended to

look unhealthy within 24 hrs, often dying within 5 days, compared with cultures on stiffer PAGs, which often survive for more than 5 days (Figure 2-12). These results suggest that there is some minimal amount of tension required for ECFN survival, which the cells were not able to generate on extremely soft PAGs.

Following *in ovo* electroporation, ~70-80% of ECFNs remain untransfected. To determine whether the substrate-dependent changes in F-actin retrograde flow were an artifact of using GFP-actin, we measured the velocity of refractile features via transmitted light microscopy in both untransfected and transfected ECFNs on soft (260 Pa) and stiff (24 kPa) substrates. We found that ECFN growth cones were visible under transmitted light imaging conditions (Figure 2-13a) along with rapidly moving refractile features, reminiscent of GFP-actin retrograde flow. By constructing kymographs along filopodia and measuring the slopes of these refractile feature movements (Figure 2-13b), we found that transfection alone did not significantly alter motion of refractile features (Within stiffness p-values - 260 Pa PAG: $p=0.2$, 24 kPa PAG: $p=0.2$). Furthermore, the motion of refractile features in both transfected and untransfected ECFNs exhibit substrate stiffness-dependence (Figure 2-13c). These results demonstrate that the substrate sensitivity observe in this study was not an artifact of altered actin dynamics due to the use of GFP-actin.

To determine whether myosin II plays a role in driving retrograde flow in our system, we recorded time-lapse images of individual GFP-actin transfected ECFNs under epi-fluorescence prior to and following the introduction of 100 μM blebbistatin, a cell membrane permeable inhibitor specific for non-muscle myosin II ATPases (Figure 2-14)[86, 87]. Prior to treatment, we find ECFN growth cones exhibit rapid retrograde

flow, as made apparent by visible GFP-actin feature streaks visible in kymographs along filopodia (Figure 2-14c). Following a 15 minute incubation in media containing 100 μm blebbistatin, ECFN morphology did not change drastically, though we observed a reduction of lamellipodia and a slight increase in filopodia length (Figure 2-14a, Figure 2-14b), similar to other reports [88]. Time lapse recordings from blebbistatin treated ECFNs had little to no apparent motion, as evidence by vertical GFP-actin feature streaks in kymographs constructed from filopodia (Figure 2-14d). These results suggest that myosin II motors provide the major driving force for F-actin retrograde flow in ECFN growth cone filopodia.

Next, to test the model prediction of increased traction force transmission on softer substrates, we considered the amount of elastic strain energy exerted by ECFNs to displace individual marker beads from their rest position as the cell pulls on the elastic substrate. To estimate the elastic strain energy stored within the substrate, stressed images of marker beads during ECFN interaction were captured, followed by an unstressed image where the cell was released from the substrate using trypsin (Figure 2-15a-b). Next, we measured the displacement of every marker bead in the field (Figure 2-15c) and estimated the total stored energy by summing the squared displacements of all marker beads above the noise and scaling the result according to the substrate stiffness (Figure 2-15d). When normalized to the projected area of the cell, this metric can be considered as a "surface tension" between the cell and the substrate. Using this method, we find that ECFNs on soft PAGs have a three-fold higher surface tension compared with stiffer gels ($p<0.01$, Figure 2-15e), in agreement with model predictions.

Together, these modeling and experimental results show that a motor-clutch retrograde flow mechanism naturally responds to substrate stiffness, with a very abrupt change around 1 kPa in the specific case of embryonic chick forebrain neurons grown in vitro. Substrate stiffness-dependent changes in clutch dynamics may serve as a basis for sensing environmental stiffness, providing differential inputs to mechanosensitive elements, ultimately transducing these signals into altered cell motility, cell morphology, and cell fate.

2.5 DISCUSSION

In this work, we take initial steps toward constructing a systems framework for understanding cellular mechanosensing by utilizing a computational model of the motor-clutch hypothesis on compliant substrates and present experimental results that directly test model predictions in ECFN growth cones. We find evidence that clutch dynamics vary in a substrate-stiffness dependent manner resulting in differences in F-actin retrograde flow rate and traction forces transmitted to the substrate in growth cone filopodia.

While this work specifically sought to capture the traction dynamics of single filopodia, filopodia must work in cooperation with other growth cone components to form a complete and functioning cellular motile machine. As with most other cell types, growth cone filopodia extend deeply into the growth cone proper and are tightly embedded within a lamellipodial network that also transmits force to the substrate [89]. Previous reports also suggest that myosin motors are primarily found in this lamellipodial region of the growth cone [90, 91]. Interestingly, we find that filopodia

within a single growth cone exhibit variable retrograde flow rates and traction dynamics, suggesting spatial stochastic variations in motile machinery components such as the number of motors or clutches. One can thus imagine extending the single motor-clutch module, as we applied here to filopodia, to incorporate multiple modules from various regions of parameter space to capture an integrated picture of growth cone or cellular motility. In the case of neuronal growth cones, our view is that the filopodia are weakly linked by a contractile lamellipodial network, which integrates the filopodial forces to determine the overall direction of growth cone advance. As currently presented, we believe the motor-clutch model comprises an important module of the motility apparatus, which captures the average filopodia behavior in response to compliant substrates. It will be important future work to link multiple motor-clutch modules together to capture the integrative behavior of more complex systems.

Computational models of this type have been used in previous studies to describe a number of cellular phenomena, including leukocyte rolling [92], microtubule aster formation and dynamics [93, 94], and mitosis [95-97]. In particular, models of microtubule aster dynamics and mitosis utilize very similar components to provide a picture of how molecular linkers (in these cases possessing motor activity) interact with and organize filaments. In fact, oscillatory behavior, such as the load-and-fail dynamics for the motor-clutch system, also occur in these systems under certain conditions, and is considered a hallmark of molecular motors working against an elastic load [98]. In our case, multiple elastic elements are incorporated into the system, and the particular balance between compliance in the molecular clutches and the compliant substrate govern the switch from frictional slippage to load-and-fail behavior. We demonstrate

that this basic, physical mechanism may play a critical role in cellular mechanosensing, providing an initial stiffness-sensitive signal that may be further amplified by mechanotransducing elements leading to cellular response.

Other modeling efforts have also explored the source of mechanosensing, mainly focusing on the growth of focal adhesions in response to forces. Bruinsma proposed a two-state model that involves a switch from a passive to an active state dependent on some critical force [99]. Substrate stiffness sensitivity depends on how quickly this critical force is reached. For example, soft substrates are proposed to have a slow development of tension within the adhesion, leading to dissociation and eventual failure of coupling. On the other hand, a stiff substrate reaches the critical force very quickly, causing the adhesion to switch to the active state, eventually leading to reinforcement of the adhesion, stalling of retrograde flow and transmission of the full traction force. While this is qualitatively similar to predictions in our current model, this two-state model predicts a logarithmic increase in forces as a function of substrate stiffness, an effect that has not yet been demonstrated experimentally.

Nicolas and Safran proposed another model of mechanosensitivity based on treating a focal adhesion as a thin film described by continuum elastic theory [100, 101]. They suggest that contractile forces impose a shear on the upper surface of the adhesion plaque, altering the density of linkers in a thin strip near the front edge, leading to a biochemical response that either grows or shrinks the focal adhesion. They later demonstrated that this effect could theoretically be modulated by substrate stiffness and thickness, concluding that focal adhesions cannot grow below a critical stiffness, and that focal adhesion size saturates to a level that is sensitive to the

mechanics of the substrate. These modeling results are consistent with studies of focal adhesion size in response to forces [71, 72], but the specific potential used to describe interaction with the extracellular matrix couples adhesion strength with the mechanics of the substrate making it difficult to model the effects of stiffness alone. In a similar manner to Bruinsma's two-state model, this system would predict an increasing traction force with substrate stiffness.

In contrast, our experimental results in ECFNs find that traction forces decreased on stiffer substrates (Figure 2-15e), consistent with motor-clutch simulations that predict a biphasic relation in traction force and substrate stiffness (Figure 2-4d). Furthermore, other reports in MC3T3-E1s and SMCs also find that migration is fastest on intermediate stiff substrates, consistent with predictions from our simple model [102, 103]. Although we were not able to observe optima in retrograde flow rate and traction force for ECFNs due to cell death on extremely soft PAGs (≤84 Pa), these results suggest a mechanism where focal adhesion feedback is not always present, allowing for discrimination of an optimal substrate. It may be that cells that exhibit durotaxis, such as fibroblasts [49], construct their motile machines with very stiff optima such that a decrease in traction has not yet been observed experimentally.

For simplicity, we omitted tension-dependent strengthening of focal adhesions in this first model, even though this phenomenon has been observed experimentally [71, 72, 104] and has been the subject of theoretical analysis [105, 106]. At least for the filopodial system that we studied this seems justifiable on the following grounds. First, growth cones are believed to utilize point contacts as coupling structures, which contain some of the proteins found in focal adhesions [82, 107] but have not been demonstrated

to increase in size as a function of force or stiffness. Second, this model addresses the specific question of how forces develop within adhesions as a function of stiffness, an effect upstream of any response of molecular clutches to the applied force. As a result, the mechano-sensitive maturation of adhesion will act as an amplifier of force inputs, but does not establish the input level itself. Future work in modeling cell migration could incorporate focal adhesion response to force as a feedback loop whereby some threshold of traction force promotes the recruitment of additional molecular clutches or some change in molecular clutch properties. In a similar vein, it is possible that gene expression changes have occurred to mediate the observed responses to substrate. However, this again requires some upstream sensing event that presumably depends on the actin-myosin contractility pulling on the substrate. So gene expression could act as an amplifier, but not as the initial sensor.

Wolgemuth and coworkers have also proposed a similar stick-slip model, where the contractile force is driven by depolymerization of the actin gel network at the rear of the lamellipodium [108]. This generates a stress within the actin network that eventually causes rupture of adhesive linkages at some critical force. This approach basically treats the adhesion plaque as a pure frictional element that slips when the driving force exceeds the static coefficient of friction, but does not incorporate a compliant substrate into the analysis. They find that the leading edge of such a system fluctuates periodically, similar to observations in mouse fibroblasts [109]. In fact, the model we present here also displays periodic fluctuations of the leading edge, assuming that actin polymerization remains constant. During coupling failure, the motor-clutch model predicts a transient increase in retrograde flow rate that leads to a slowing, or

slight retraction of the edge, as F-actin polymerization cannot keep up. As clutches reengage, they slow retrograde flow, allowing F-actin polymerization to once again advance the leading edge. These effects were all observed in the study by Sheetz and coworkers [109]. In conjunction with our model incorporating substrate stiffness, this suggests that the periodicity of leading edge fluctuations should be substrate stiffness dependent and would be an important future test of the model.

Finally, Schwarz and coworkers have also preformed very detailed theoretical analysis on single bonds working in adhesion clusters using similar Bell model assumptions [110, 111]. They show that under certain circumstances, adhesion clusters are either stable or rupture, and that the rupture dynamics are sensitive to the stiffness of the environment. While these results are similar to what we found in our theoretical exploration, Schwarz and coworkers treat the force as acting normal to the adhesion cluster. In this case, all bonds have the same strain, and rebinding occurs under load, as a clutch much span the current distance between the substrate and the receptor-plate to rebind. In contrast, we treat the force as acting shear to the adhesion cluster such that clutches behave independently, rebinding with no load. These differences might lead Schwarz's treatment of adhesions to be slightly less stable than our presentation.

In summary, the results of this study indicate that the manner in which forces build within adhesions can vary depending on substrate stiffness, which in turn may lead to differential activation of mechanotransductive elements within adhesive clusters. In this way, the motor-clutch mechanism may serve as a basis for mechanosensing, ultimately leading to altered cell morphology, motility, and fate.

2.6 Acknowledgements

This research was supported by the Institute for Engineering in Medicine at the University of Minnesota, the National Science Foundation (MCB-0615568), and the National Institute of General Medical Sciences (R01-GM-76177). We thank Paul Letourneau, Dennis Bray, and Erkan Tuzel for stimulating discussions; Nerendra Simha for helpful discussions on gel mechanics; Naoko Koyano for assistance with *in ovo* electroporation; and members of the Odde Lab, Dominique Seetapun, Andrew Bicek, Melissa Gardner, and Tyler Dahl for technical assistance.

2.7 Tables and Figures

Table 2-1 Parameters of the Stochastic Motor-Clutch Model.

Model Parameter	Description	Typical Value	Source
v_{poly}	F-actin net assembly rate	70 nm/s	Mallavarapu & Mitchison, 1999, 10-30 nm/s [73]
n_m	Total number of myosin motors	75	Free parameter, set to match estimated mean max filopodial force measured in this study
$\hat{F}_m$	Single myosin motor stall force	-2 pN	Molloy et al., 1995 [112]
v_u	Unloaded myosin motor velocity	-120 nm/s	Cuda et al., 1997, 80-5000 nm/s; This study [113]
n_c	Total number of molecular clutches	75	Free parameter, set to slow retrograde flow to experimentally observed levels
k_{on}	Pseudo first-order on-rate constant of clutch binding to F-actin	1 s^{-1}	Adjusted to match dynamics observed in this study
k_{off}	Pseudo first-order unloaded off-rate constant for clutch dissociation from F-actin	0.1 s^{-1}	Lele et al., 2008, 0.01-0.1 s^{-1} [114]
F_b	Characteristic bond rupture force, clutch to F-actin	-2 pN	Jiang et al., 2003, 2 pN [115]
κ_c	Molecular clutch spring constant	5 pN/nm	Estimated from Fisher et al., 1999, on the order of pN/nm [116]
κ_{sub}	Compliant substrate spring constant	0.01-100 pN/nm	This study; estimated using Cerruti solution (Figure 2-2)

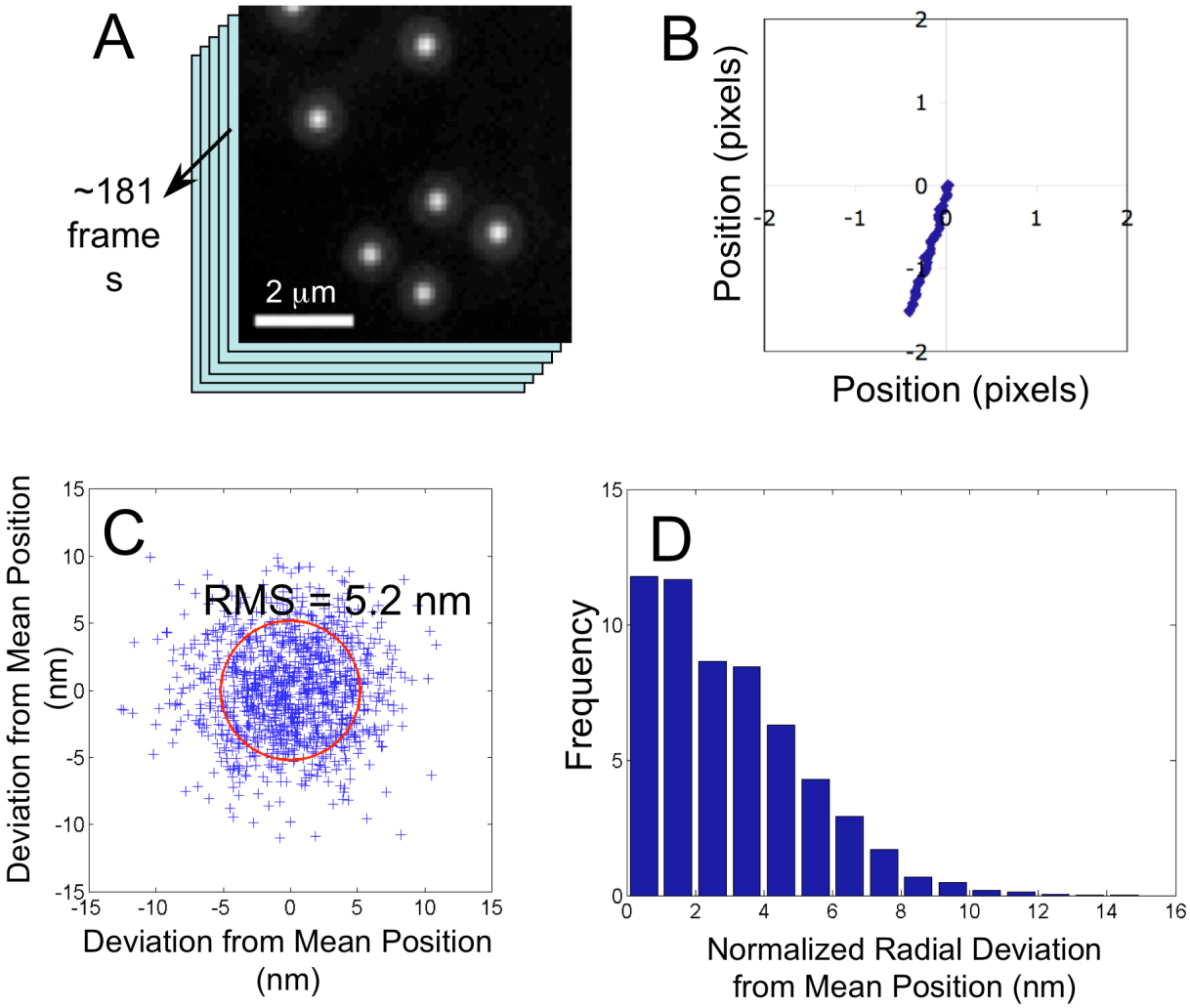

Figure 2-1 Validation of bead tracking algorithm.
(A) Image stack of a reference region far from cells have stationary marker beads. (B) Drift of reference region is estimated as the mean deviation of marker beads from their positions in frame 1, and subtracted from the image stack to correct for drift. (C) Scatter plot of deviations from the mean position of reference beads indicates a RMS deviation of 5.2 nm. (D) Histogram of normalized radial deviation from mean reference bead position are approximately Gaussian.

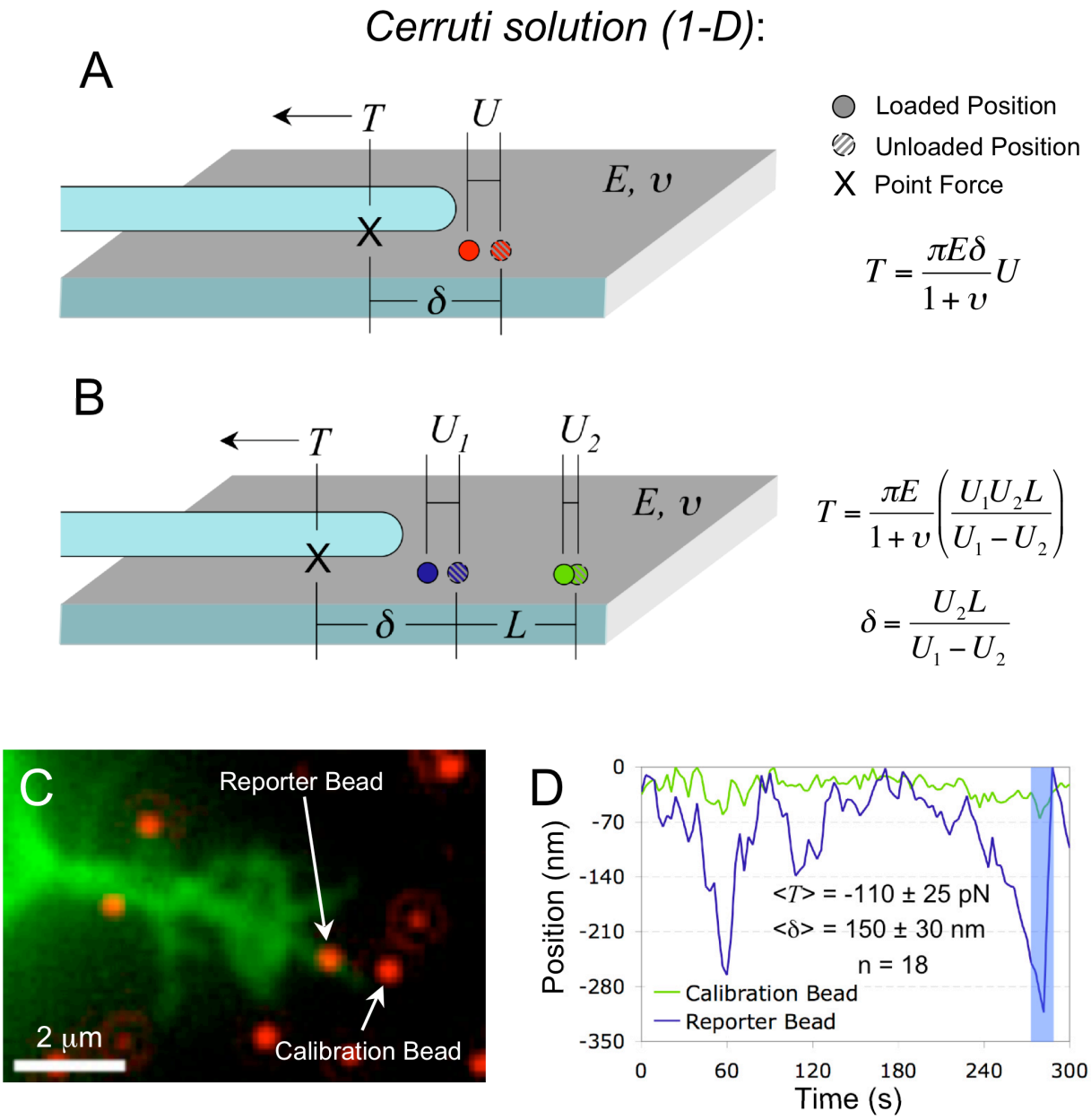

Figure 2-2 Estimation of maximum filopodial traction force using the *Cerruti* solution.
(A) 1-D *Cerruti* solution for a point force acting tangential to a half plane. (B) Solutions for force, T, and distance between point of force application and the closest reporter bead, δ, using a second calibration bead. (C) Example image used for estimation of filopodial force. (D) Positions at maximal strain (light blue region) used to estimate T and δ.

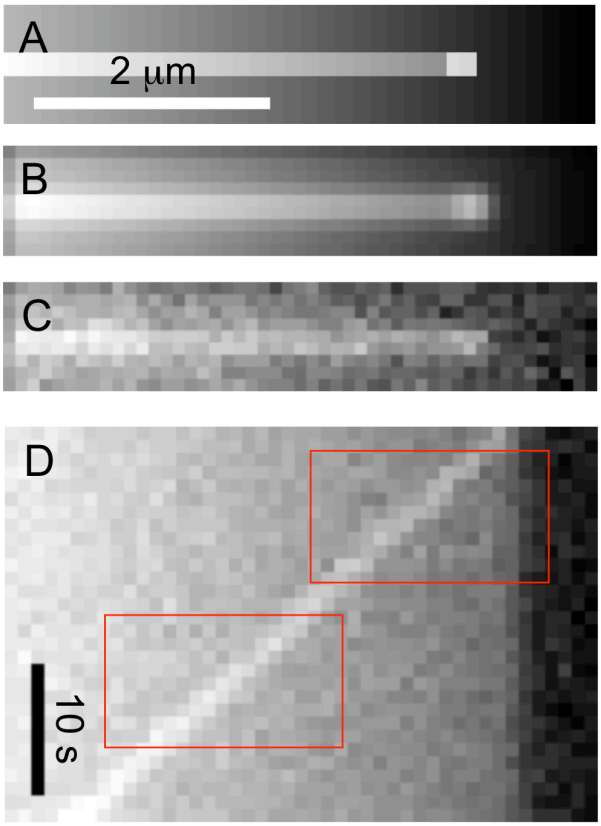

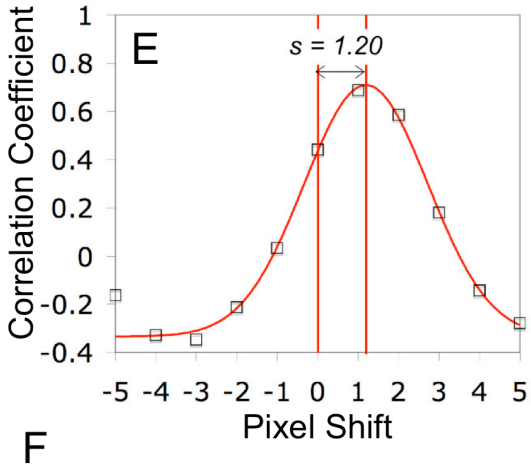

F

Simulated Velocity (nm/s)	Measured Velocity (nm/s)
80	*83±2*
90	*93±1*
100	*106±2*
110	*114±2*

Figure 2-3 Validation of cross-correlation F-actin flow tracking algorithm.
(A) Finemesh representation of a filopodium with a bright F-actin feature at the tip. An overall gradient in light intensity is superimposed to mimic light scattering from the growth cone. (B) Finemesh image from **A** convolved with the point spread function and coarse-grained to 100 nm pixels. (C) Coarse-grained imaged from **B** with added background signal and Gaussian-distributed noise. (D) Kymograph of stack of synthetic images as in **C** with moving F-actin feature. (E) Correlation coefficient profile from windowed cross correlation with fitted Gaussian yields the velocity of the feature. (F) Measured velocity extracted from synthetic image stacks shows agreement to the actual simulated velocity to within 5%.

Figure 2-5

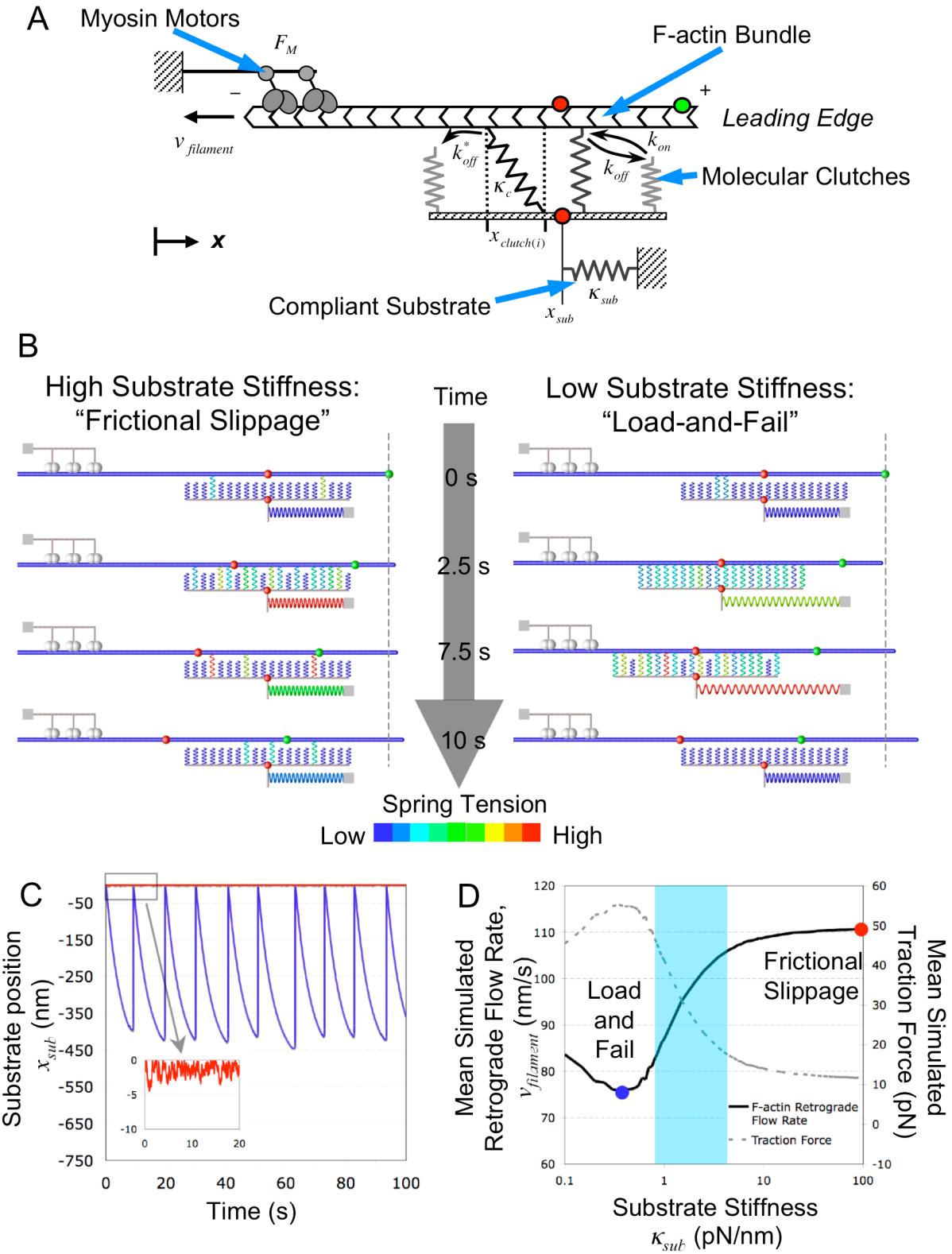
A
Myosin Motors
F-actin Bundle
Leading Edge
Molecular Clutches
Compliant Substrate
B
High Substrate Stiffness:
"Frictional Slippage"
Time
Low Substrate Stiffness:
"Load-and-Fail"
0 s
2.5 s
7.5 s
10 s
Spring Tension
Low
High
C
Substrate position
Time (s)
D
Mean Simulated
Retrograde Flow Rate,
Mean Simulated
Traction Force (pN)
Load
and
Fail
Frictional
Slippage
F-actin Retrograde
Flow Rate
Traction Force
Substrate Stiffness

Figure 2-4 A model for motor-clutch motility on compliant substrates predicts substrate stiffness-dependent dynamics.
(A) Schematic representation of a mechano-chemical motor-clutch model. Myosin motors pull an F-actin filament bundle to the left with force F_M. Molecular clutches reversibly engage the F-actin bundle with rates k_{on} and k_{off} to resist retrograde flow. During loading, the clutches are stretched to strains $x_{clutch(i)}$, and tend to fail with a force dependent off rate, k_{off}*. Transmitted forces induce a local substrate strain, x_{sub}. The mechanical stiffness of the clutches, κ_c, and of the substrate, κ_{sub}, determine the mechanical resistance to loading. (B) Model predicted substrate stiffness-dependent clutch dynamics. Red markers indicate the initial position of the bundle and substrate and highlight their relative motion. Green marker indicates the initial F-actin bundle position. (i) Stiff substrates exhibit "frictional slippage", where the F-actin bundle constantly slides relative to the substrate (red markers move apart). (ii) Soft substrates exhibit "load-and-fail", where the compliant substrate moves with the F-actin bundle until coupling failure. (C) Model predicted substrate position as a function of time highlights load-and-fail on compliant substrates (blue). Stiff substrates exhibit frictional slippage (red, and inset). (D) Load-and-fail clutch dynamics are predicted to lead to slower time averaged F-actin retrograde flow rates and higher traction forces whereas frictional slippage dynamics lead to increased retrograde flow rates and decreased traction force. The transition zone (light blue) defines a region of greatest sensitivity to substrate stiffness.

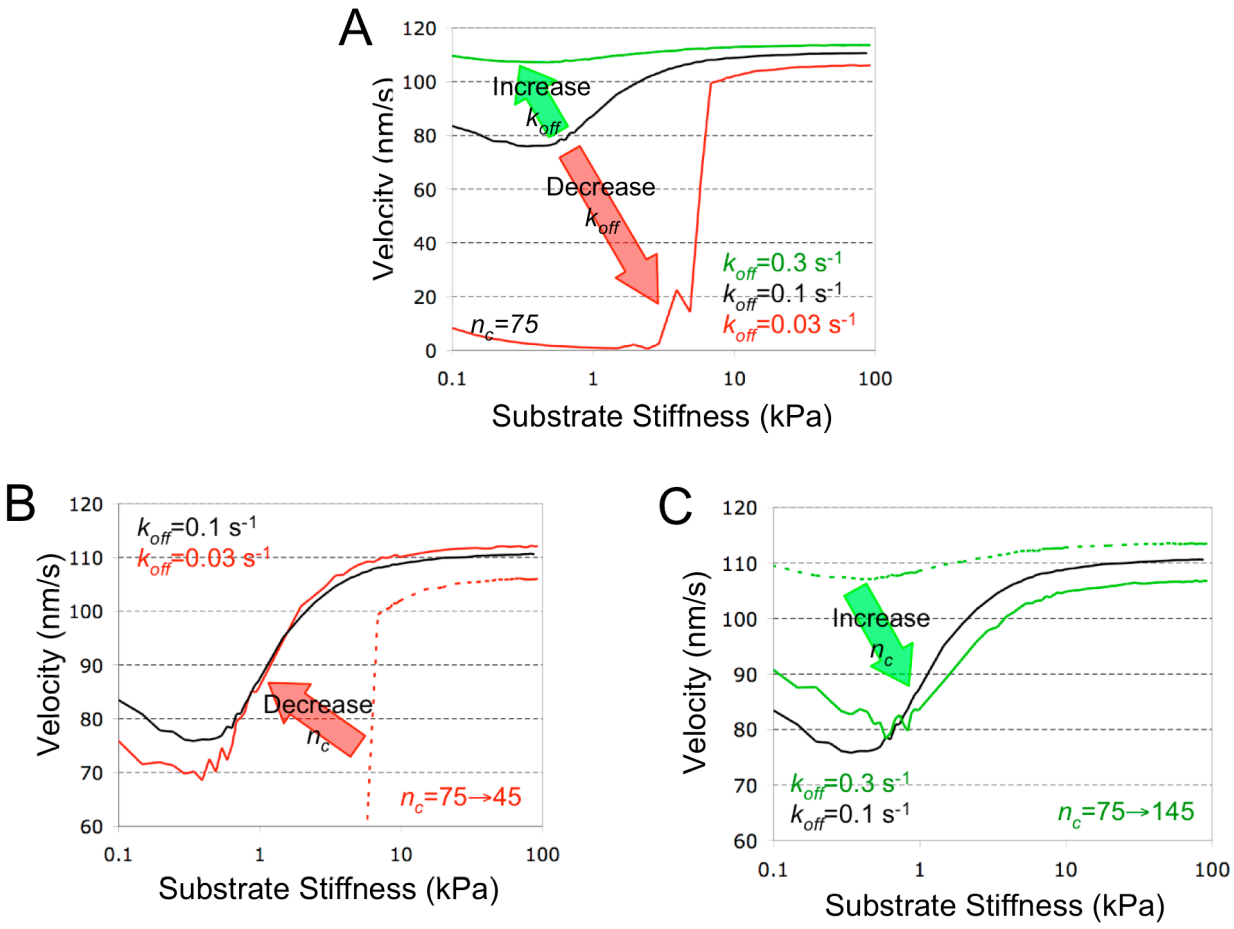

Figure 2-5 Clutch dynamics transition is a robust feature of motor-clutch model.
(A) Varying k_{off} by a factor of 3 can alter model behavior to either continuously slip, or completely stall. (B) Stalling systems can be shifted back to load-and-fail by reducing of the number of clutches, n_c, in the system. (C) Continuously slipping systems can be shifted back into load-and-fail dynamics by increasing n_c.

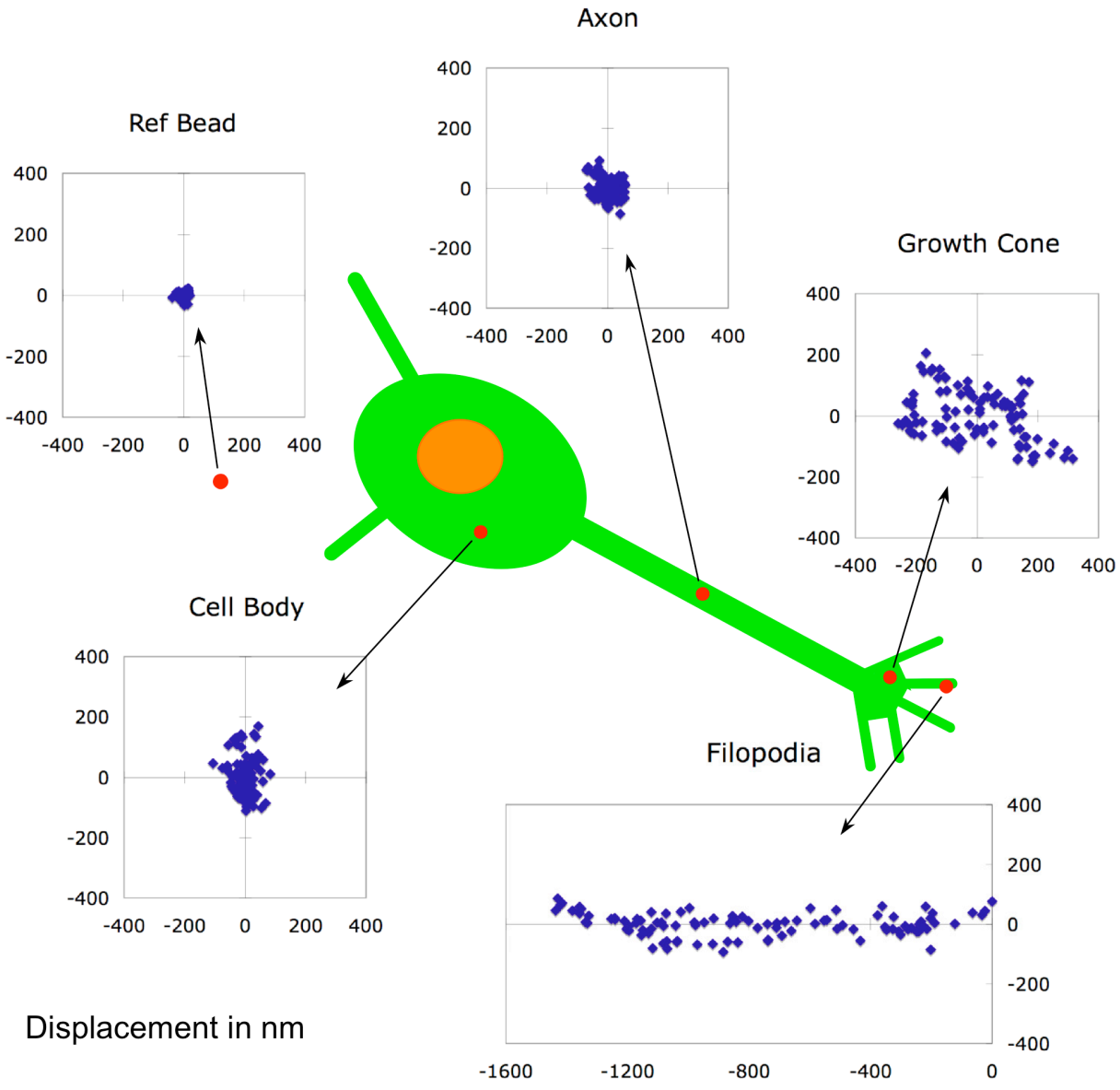

Figure 2-6 Spatial map of neuronal traction force dynamics.
Small random fluctuations occur under the cell body and axon with larger, randomly fluctuating beads under the growth cone. Very large, directed bead motions occur most frequently near growth cone filopodia.

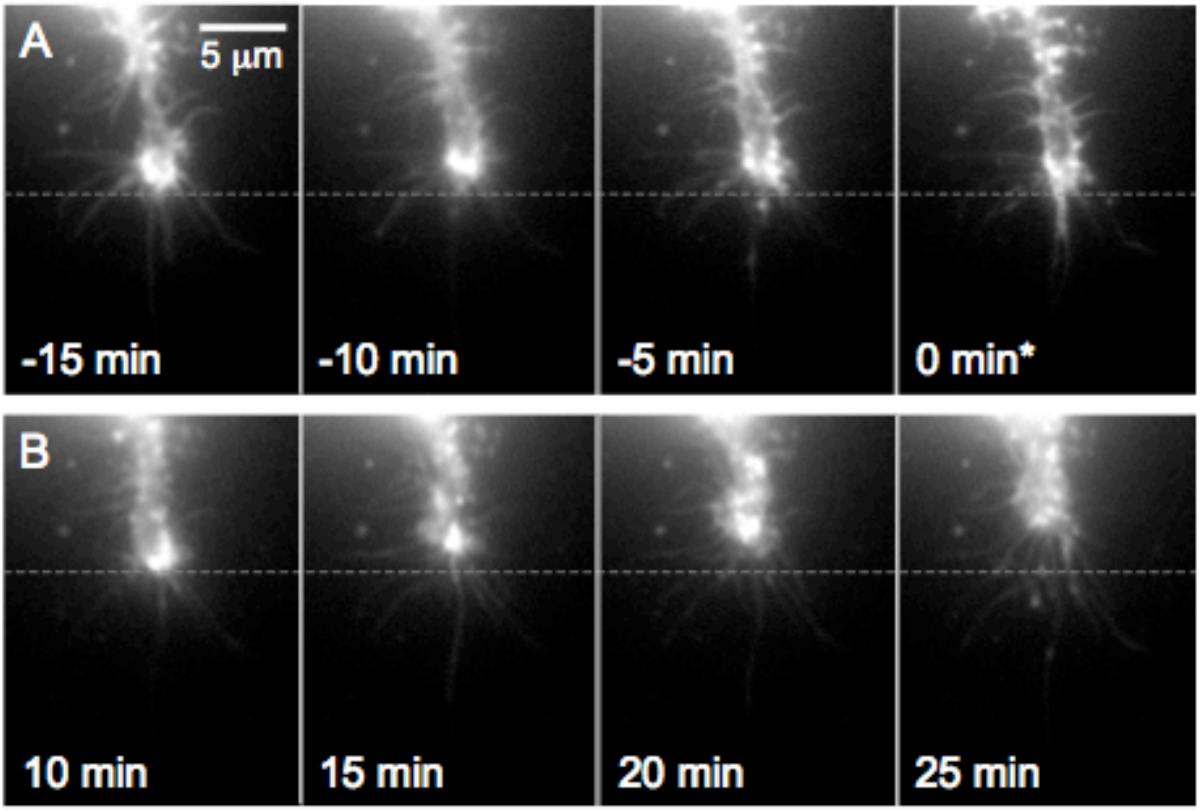

Figure 2-7 ECFN growth cone advance depends on β1-integrins.
(A) ECFN growth cone neither advanced nor retracted 15 min prior to anti-β1 integrin antibody addition. (B) In the presence of anti-β1 integrin antibodies (introduced at *), the growth cone retracts within 25 min.

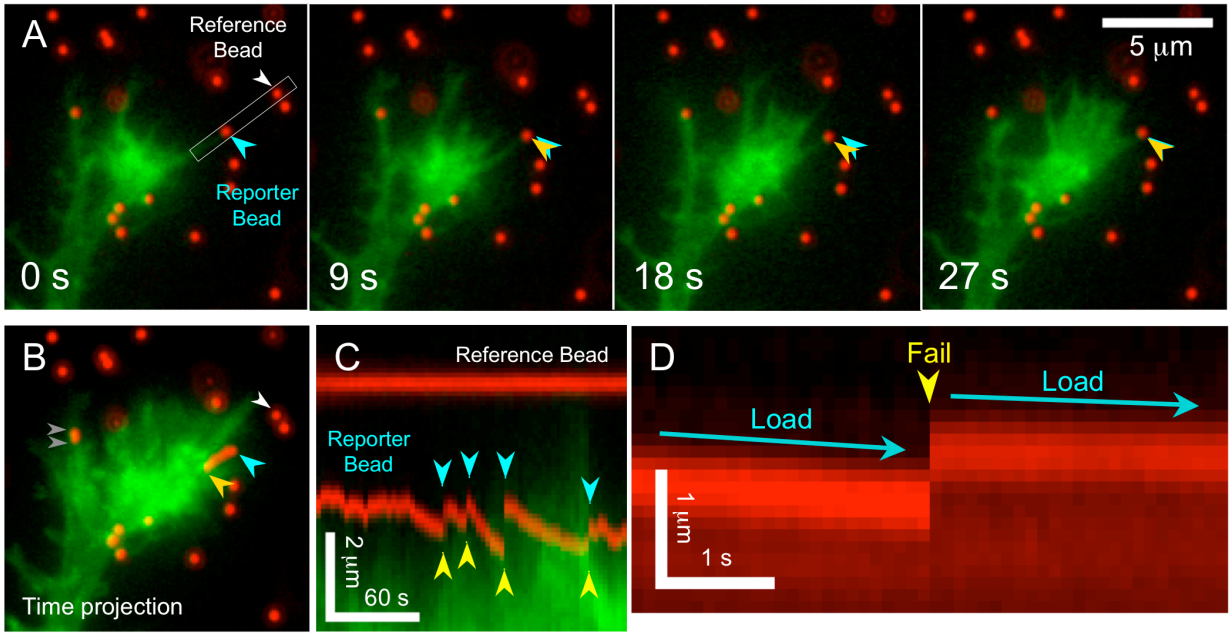

Figure 2-8 Growth cone filopodia on compliant substrates exert traction forces with "load-and-fail" dynamics.
(A) Montage of a GFP-actin transfected ECFN growth cone on a 730 Pa PAG with embedded fiduciary marker beads acquired at 3 s intervals. A reporter bead underneath a growth cone filopodium displays periodic motions. Cyan arrowheads indicate initial position. Yellow arrowheads indicate position at the given time point. (B) Time projection of the image stack over 5 minutes. The marker bead in **A** appears as a line (blue and yellow arrowheads). The reference bead (white arrowhead) appears as a single spot. A second marker bead (gray arrowheads) was also pulled retrogradely, as evidenced by the elongated appearance. (C) Kymograph of the region indicated in **A**. Yellow arrowheads indicate abrupt failure events. (D) Marker bead position recorded at 100 ms intervals.

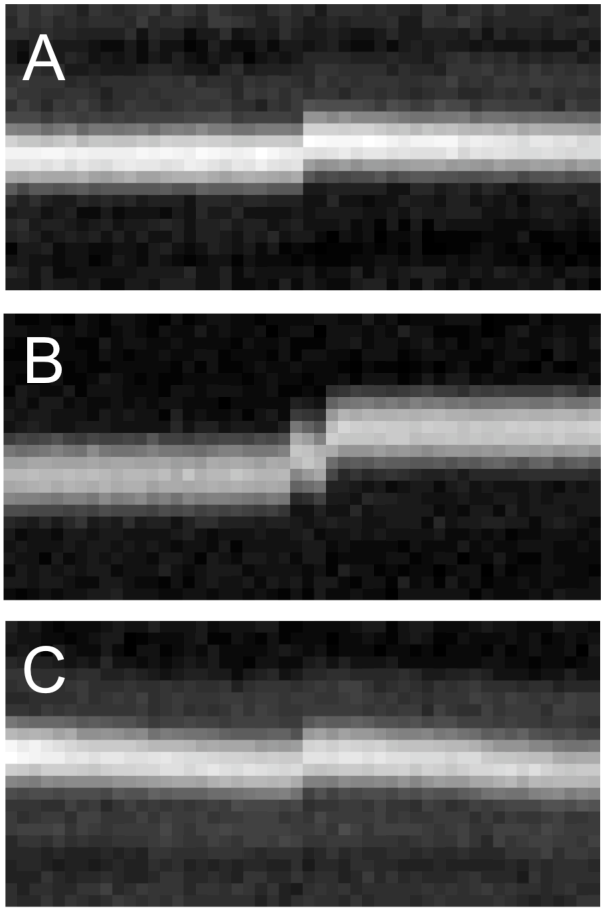

Figure 2-9 High temporal resolution (100 ms) traction force dynamics reveal abrupt failure events. (A & B) Failure events observed on 1300 Pa PAGs (Scale: vertical /spatial dimension: 2.5 μm; horizontal/temporal dimension: 5 s). (C) Failure event observed on 260 Pa PAGs (Scale: vertical /spatial dimension: 2.5 μm; horizontal/temporal dimension: 5 s).

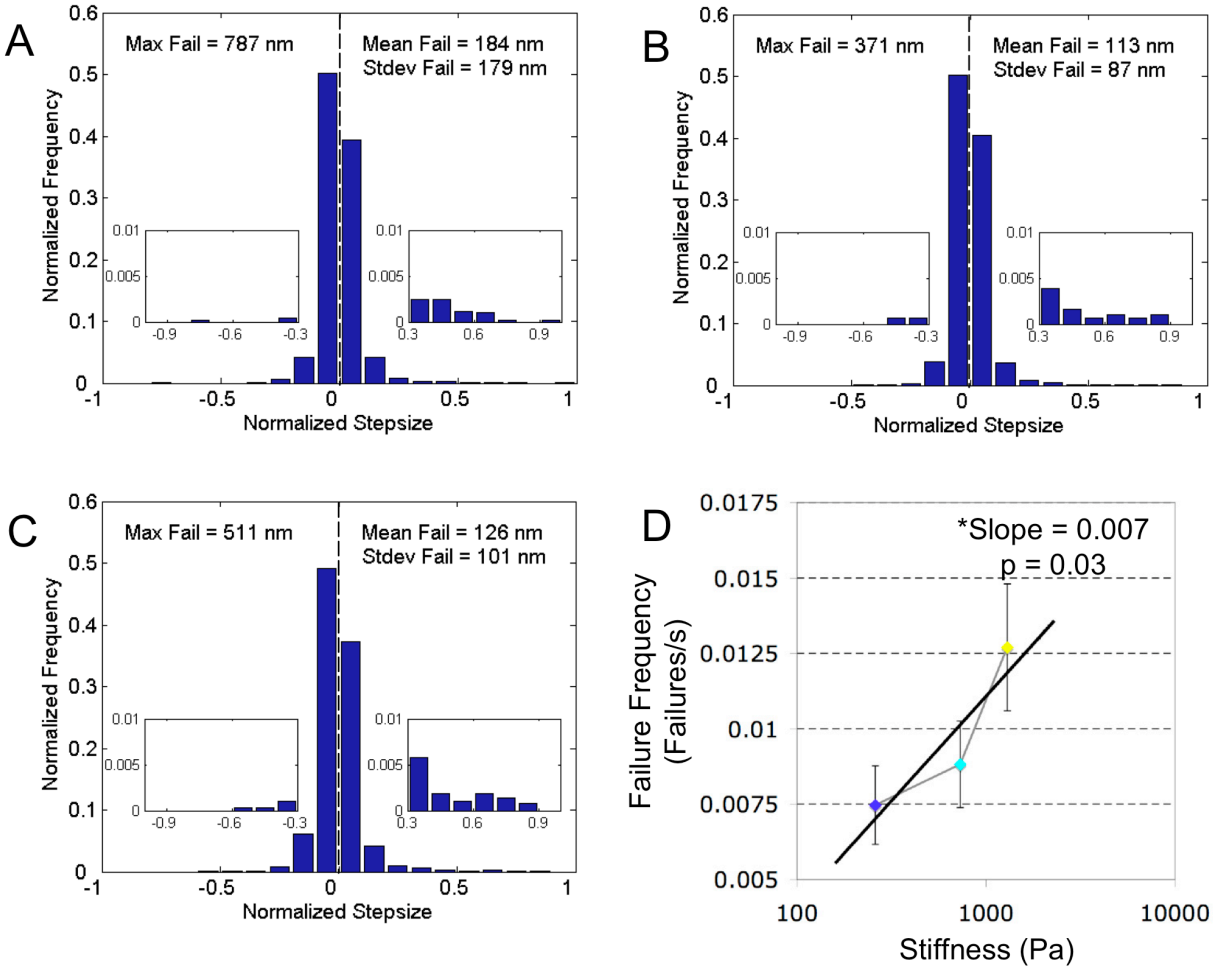

Figure 2-10 Aggregate marker bead single time increment displacement distributions. Aggregate marker bead single time increment displacement distribution for (A) 260 Pa, (B) 730 Pa, and (C) 1300 Pa PAGs. Insets highlight large failure events (>0.3) and small loading events (<0.3). (D) Failure frequency increases with increasing stiffness.

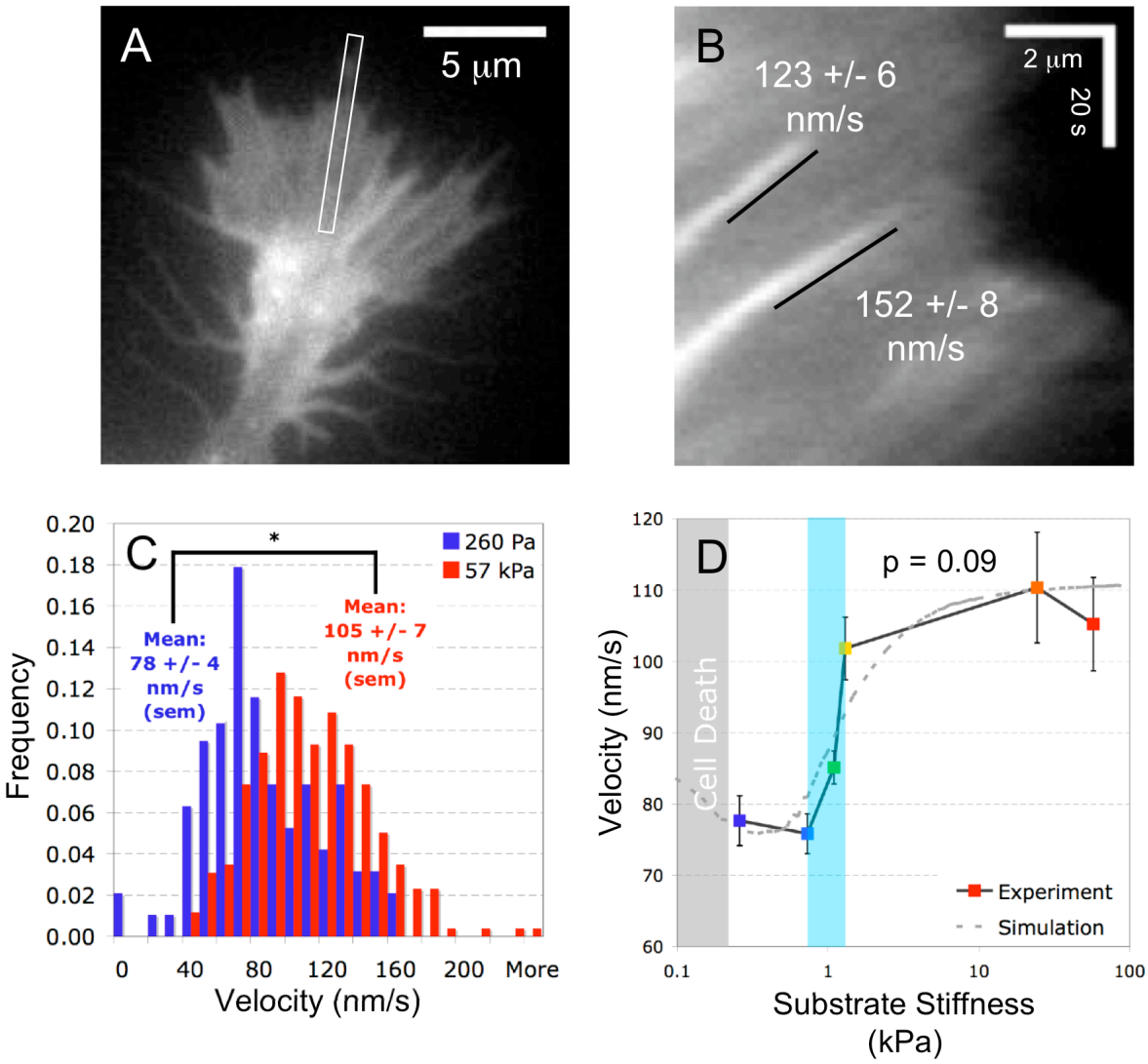

Figure 2-11 Growth cone filopodia F-actin retrograde flow rate abruptly transitions from low to high around an elastic modulus of E=1 kPa.

(A) EGFP-actin transfected ECFN growth cone. (B) Kymograph along region indicated in **A**. GFP-actin features create diagonal streaks, allowing measurement of F-actin retrograde flow. (C) Histogram of measured F-actin retrograde flow rates on stiff and soft substrates (E=260 Pa PAG, n = 95; E=57 kPa PAG, n = 258; $p<0.001$). (D) Measurements of F-actin retrograde flow over a range of stiffness indicate a narrow region of sensitivity (light blue shaded region) and a trend statistically consistent with model predictions. Very low stiffness (gray region) result in poor cell viability.

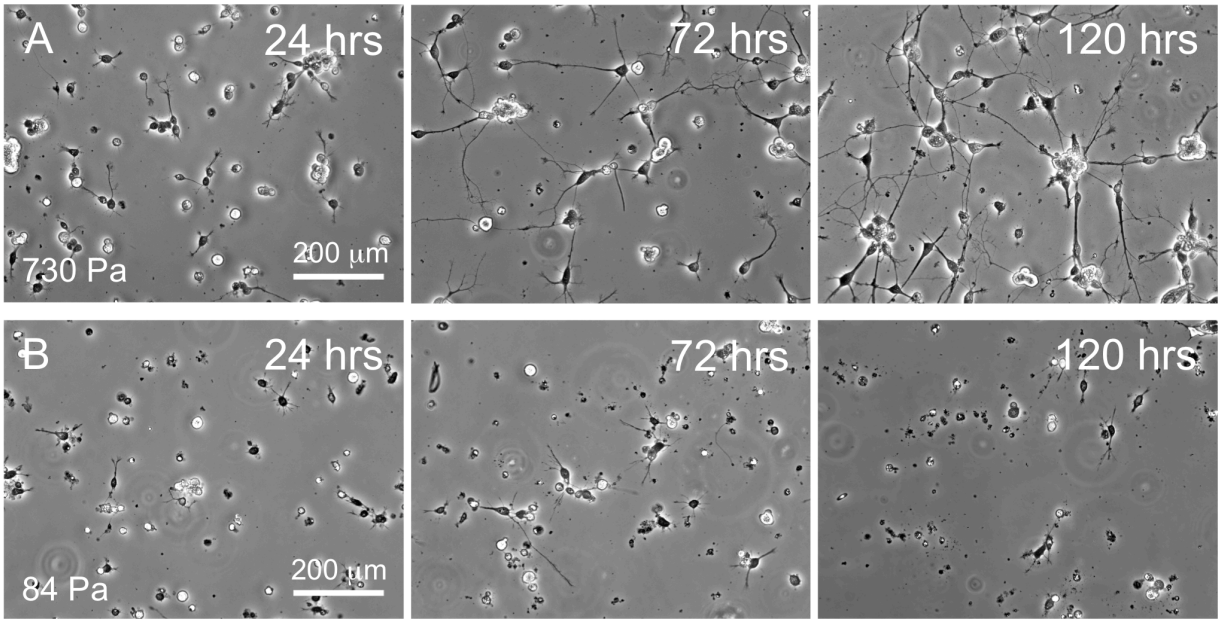

Figure 2-12 ECFNs die on extremely soft PAGs.
(A) ECFNs plated on 730 Pa PAG remain healthy for more than 120 hrs. (B) ECFNs plated on 84 Pa PAG look unhealthy within 24 hrs, dying within 120 hrs.

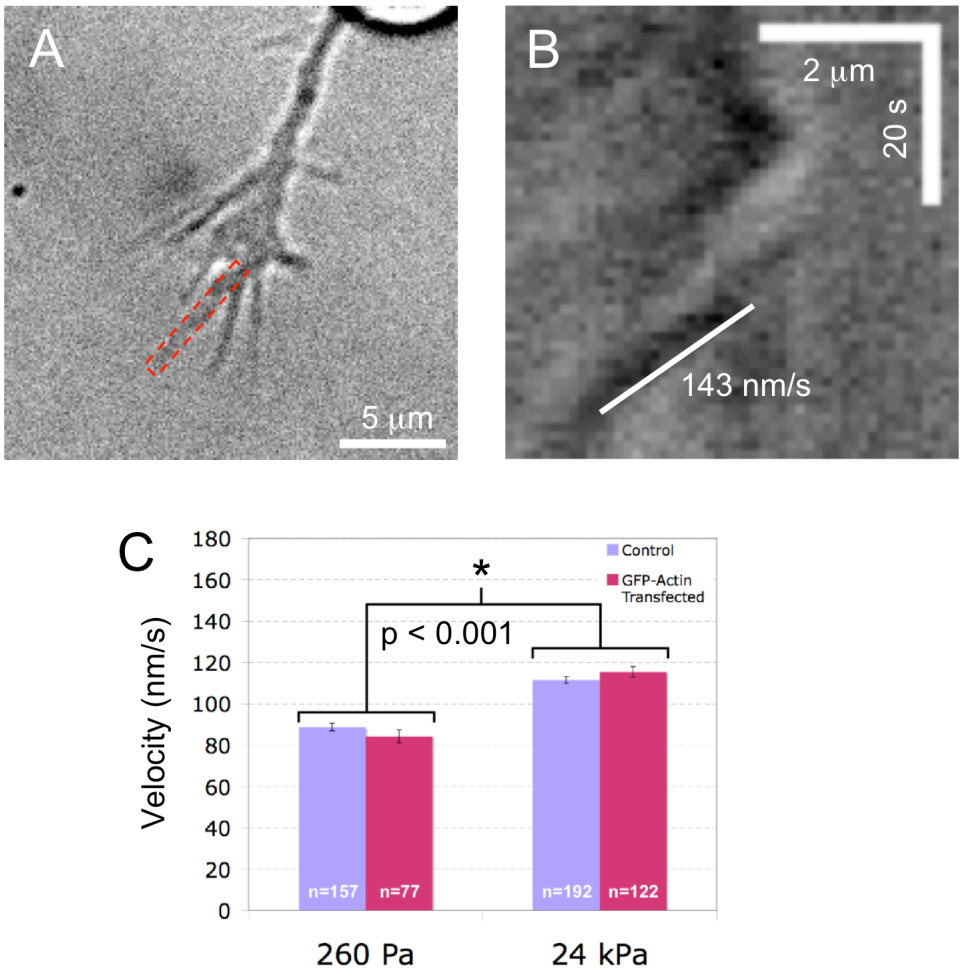

Figure 2-13 Untransfected ECFNs exhibit F-actin retrograde flow substrate stiffness sensitivity. (A) Transmitted micrograph of an ECFN growth cone. (B) Kymograph of region indicated in **A** highlights refractile features that track with retrograde flow. (C) Mean retrograde flow rates on soft versus stiff PAG substrates are significantly different, while in control versus GFP-actin transfected growth cone filopodia are not (Within stiffness p-values - 260 Pa PAG: p=0.2, 24 kPa PAG: p=0.2).

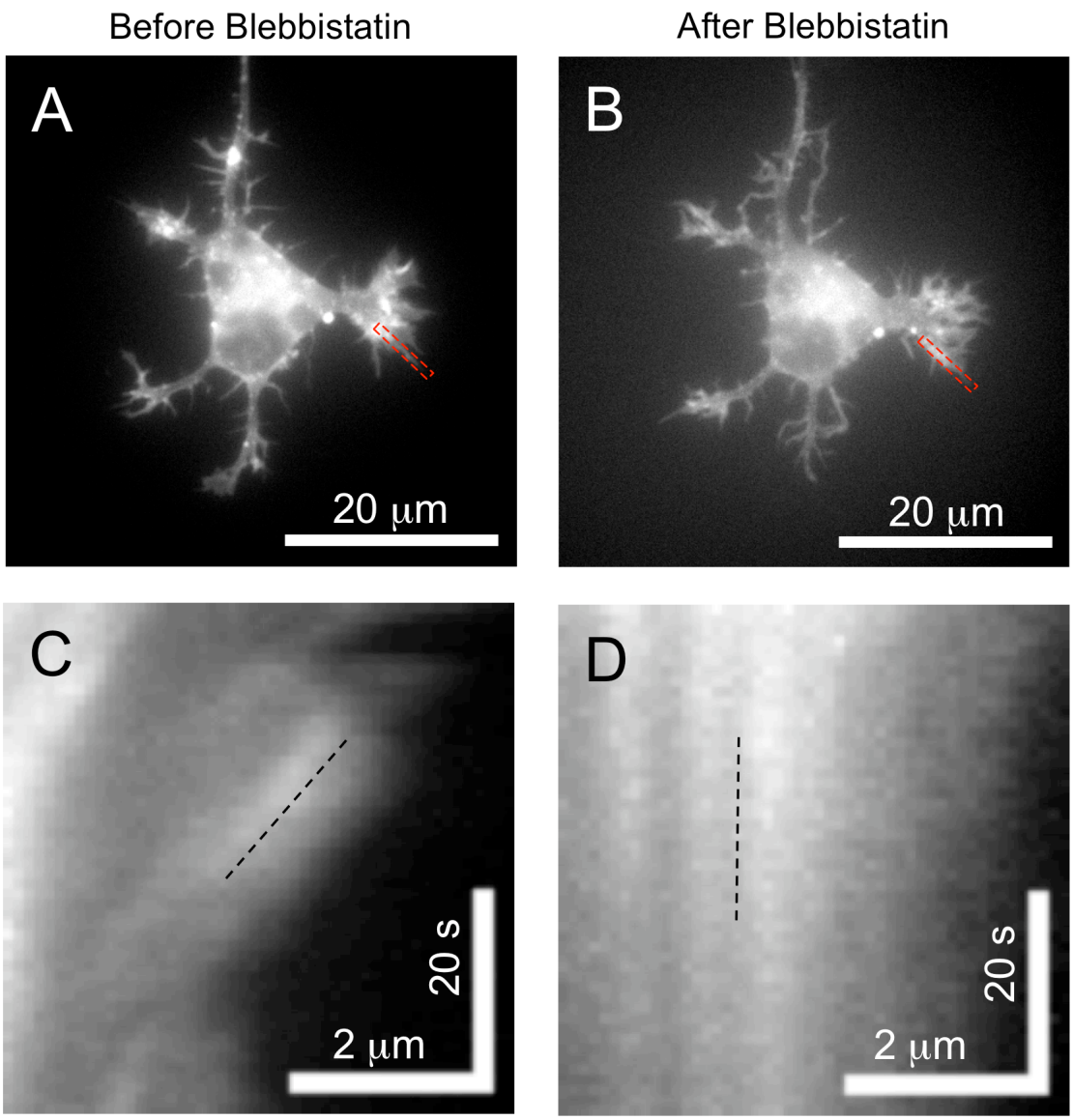

Figure 2-14 F-Actin retrograde flow in ECFN growth cones is myosin II dependent.
(A) GFP-actin transfected ECFN before treatment. (B) ECFN in **A** after 15 min treatment with 100 μM blebbistatin. (C) Kymograph of region indicated in **A** shows retrograde flow of F-actin (dotted line). (D) Kymograph of region indicated in **B** after treatment with 100 μM blebbistatin shows little motion of F-actin (dotted line).

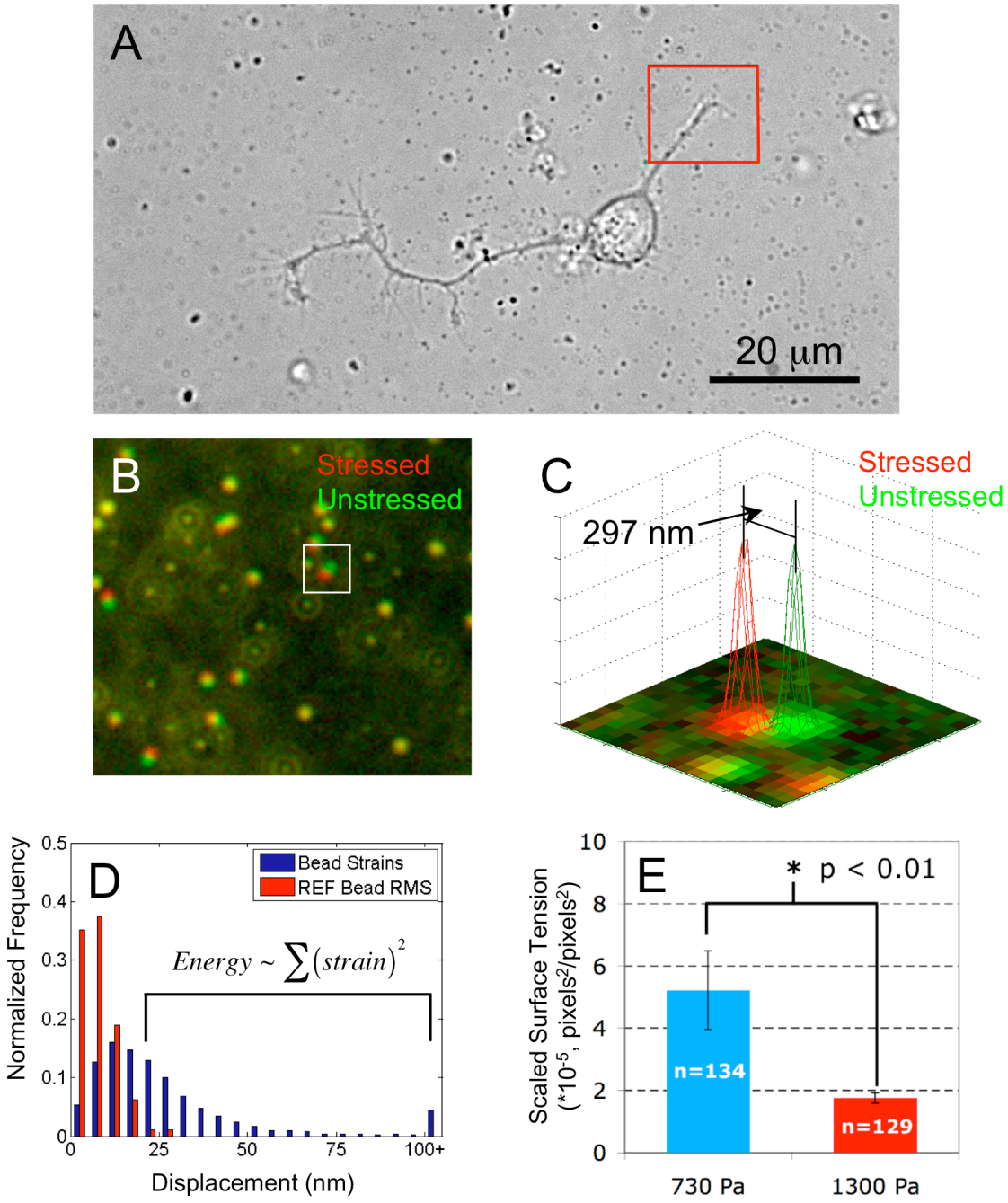

Figure 2-15 Surface tension of ECFNs decreases on stiff PAGs.
(A) Phase image of an ECFN on a PAG substrate. (B) Stressed/Unstressed images of region highlighted in **A** reveals bead strains within the substrate. (C) Image processing of region highlighted in **B** identifies and measures bead strains within the substrate. (D) Sum of all bead strains above reference bead noise are used to estimate the relative elastic energy stored within the substrate. (E) Surface tension significantly decreases on stiff substrates (mean +/- s.e.m.).

- CHAPTER 3 -
MICROTUBULE-LATTICE DIFFUSION AND INTERDIMER ASSOCIATIONS PROMOTE ROBUST KINETOCHORE COUPLING

3.1 Abstract

During mitosis, eukaryotic cells separate sister chromatids by utilizing microtubules (MTs) in conjunction with kinetochore proteins. Of particular interest are the protein complexes Ndc80 and Dam1, which have been suggested to form a direct mechanical linkage between the kinetochore and MTs [27, 35, 117]. While significant progress has been made in identifying components of the kinetochore, the physical mechanism by which these protein complexes work together to maintain attachment to dynamic MTs remains unresolved. To further our understanding of attachment under load, we constructed a computational model where attachment is mediated by dynamic molecular clutches that reversibly bind lattice-bound tubulin either through intradimer association, or interdimer association. Our simulations show that kinetochores with clutches that can also diffuse on the surface of the microtubule maintain better attachment by decreasing the stress along individual linkers to minimize detachment forces. Interestingly, interdimer associations play a key role in kinetochore attachment, providing a mechanism to quickly 'recycle' clutches that become inactive due to association with tubulins that depolymerized from the MT plus-end. We found that simulated kinetochores possessing clutches that undergo MT-lattice diffusion and interdimer association track most robustly and support greater loads than kinetochores that lacked diffusion and/or bound to tubulin within the dimer.

3.2 Background

For several decades, Hill's sleeve model has shaped our perception of the mechanism of kinetochore attachment. Based on knowledge at the time, Hill proposed that the kinetochore consisted of channels or sleeves lined with tubulin binding sites [45]. The position of the kinetochore was thought to be determined by a balance of forces: (1) an insertion force driven by affinity of the sleeve for tubulin, and (2) a resistive force required to break all tubulin interactions to move to the next favorable position. Increasing the MT sleeve overlap would reduce the systems free energy, but required exceeding an ever-increasing energy barrier for breaking all other MT-sleeve interactions. Thus, end-tracking in this system was achieved as the system maintained a steady-state insertion while tubulin depolymerized from the MT-lattice.

More recently, key components of the kinetochore have been identified, including their structure, site of interactions, and unique properties thought to be important in their function [23, 26, 118]. In contrast to the crystalline nature implied in Hill's conceptualization, electron tomographic studies reveal a kinetochore outerplate composed of an open fibrous mesh, providing the space required for tubulin arrivals and departures from the MT-lattice [33]. These structures are thought to be consistent with the long rod-like shape of Ndc80 complex, a highly conserved set of kinetochore proteins found in yeast to humans [119]. Interestingly, advances in cryoelectron microscopy have shown that Ndc80 associates strongly with the tubulin interdimer interface, a property thought to stabilize the MT-lattice [34]. In yeast, the Dam1 complex has also been identified as an essential component for maintaining end-on

attachments [120]. *In vitro* reconstitution of this complex in the presence of MTs lead to the discovery that Dam1 oligomerizes to form an encircling ring that can slide along the length of MTs [35, 121]. Similar rings structures have been found in other model systems dependent on high concentrations of the motor protein kinesin-13, and have been suggested to be the equivalent of Dam1 rings in higher eukaryotes [122].

These recent discoveries have lead to new modeling efforts in an attempt to explain kinetochore attachment and end-tracking to dynamic MTs. In particular, *in vitro* observations of Dam1 rings have lead many to postulate a mechanism where a ring device converts the natural curvature of protofilaments of depolymerizing MTs into useful work [41-43]. These models argue that by utilizing the energy of hydrolysis, a ring coupling device could produce ~75 pN of force, significantly greater than forces predicted in Hill's sleeve model (12 pN). These forces are consistent with measurements of the required force of ~50 pN/MT to stall a grasshopper spermatocyte chromosome in anaphase [123].

While these models seek to incorporate recent findings, complete encircling Dam1 rings have not been observed in *in vivo* studies. New studies also find that Dam1 complexes are able to track MTs without forming a ring structure [44], questioning the importance of such a structure. Finally, estimates of the energy stored during MT polymerization vary considerably [124], suggesting forces produced may actually be substantially lowered than anticipated. Here we present a cellular dynamics adhesion model of kinetochore attachment, incorporating the fundamental principles outlined in Hill's model with our current understanding of the functional properties of key kinetochore components. From this theoretical approach, we predict how MT-lattice

diffusion and interdimer association might benefit kinetochore function, and further establish these properties as key elements of robust MT attachment and end-tracking.

3.3 Methods

3.3.1 Mathematical Model

Model Assumptions

In this model, we treat the microtubule as a rigid rod, depolymerizing from its plus-end with constant velocity. Molecular clutches are treated as Hookean springs, bound to a rigid kinetochore, with their free MT associating end subject to thermal motions. Thus, under thermal motion, the free-ends of clutches occupy a space centered about their rest position with a Gaussian distribution having standard deviation

$$\sigma = \sqrt{\frac{k_B T}{\kappa_{clutch}}} \qquad \text{(Eq. 3-1)}$$

where k_B is Boltzmann's constant, T is the temperature (37 °C), and κ_{clutch} is the spring constant of the molecular clutches. Proximal clutches whose probable positions completely lie under the MT have full access to the microtubule and associate with the filament with rate constant k_{on}. The probable positions of distal clutches have less overlap with the MT and thus have a lower probability of coming in contact and binding. Thus, the effective association rate of the *i*th clutch along the kinetochore can be defined as the integral of its probability density function from -∞ to the plus-end of the MT, or:

$$k^*_{on(i)} = k_{on} \cdot \frac{1}{\sigma\sqrt{2\pi}} \int_{-\infty}^{x_{MT}} e^{\frac{-(x - x_{rest(i)})^2}{2\sigma^2}} dx \qquad \text{(Eq. 3-2)}$$

where x_{MT} is the position of the MT plus-end, and $x_{rest(i)}$ is the rest position of the *i*th clutch. Once engaged to the MT, forces that shift the position of the kinetochore can reduce or increase the strain along an individual linker. As the linkers develop tension, we assume that their dissociation rate increases exponentially according to a Bell Model [58]:

$$k_{off(i)}^{*} = k_{off} \cdot e^{F_{clutch(i)} / F_b} \quad \text{(Eq. 3-3)}$$

where k_{off} is the unloaded dissociation rate, F_b is the characteristic bond rupture force, and $F_{clutch(i)}$ is the tension along an individual clutch defined as:

$$F_{clutch(i)} = \kappa_{clutch} \cdot x_{clutch(i)} \quad \text{(Eq. 3-4)}$$

where $x_{clutch(i)}$ is the strain of the *i*th clutch.

When allowed, clutches can also diffuse along the MT-lattice with rate k_{diff}, biased by the stress experienced by the individual clutch. To determine which direction the clutch head will diffuse, we estimate the probability of stepping a distance delta in either direction based on the change in free energy by:

$$p\left(x_{clutch(i)} + \delta\right) \sim e^{-U(x_{clutch(i)} + \delta) / k_B T} \quad \text{(Eq. 3-5)}$$

in the case for diffusing to the right, or:

$$p\left(x_{clutch(i)} - \delta\right) \sim e^{-U(x_{clutch(i)} - \delta) / k_B T} \quad \text{(Eq. 3-6)}$$

in the case of diffusing to the left. We define U as the energy potential of the spring-like clutch as:

$$U = \frac{1}{2} \kappa_{clutch} x^2 \quad \text{(Eq. 3-7)}$$

where δ is the step size of the diffusive process. By taking the ratio of these probabilities and using the relation that the probabilities must sum to 1, we can solve this system of equations to calculate the probability of stepping to the left as:

$$p\left(x_{clutch(i)}-\delta\right)=\left(e^{\frac{-\left(U\left(x_{clutch(i)}+\delta\right)-U\left(x_{clutch(i)}-\delta\right)\right)}{k_BT}}+1\right)^{-1} \quad \text{(Eq. 3-8)}$$

Finally, clutches can also disengage from the filament due to depolymerization of their associated tubulin dimer from the plus-end of the MT. In the case where clutches prefer intradimer association, we assume that tubulin dissociation from the MT-lattice does not alter the intradimer interface. Thus, the released tubulin dimer remains associated with the clutch, with the freed tubulin dimer eventually leaving the clutch at the unloaded dissociation rate, k_{off}. In kinetochore-clutch systems that prefer interdimer association, we assume that tubulin dissociation from the lattice eliminates the interdimer interface. In this case, we assume that the clutch leaves with the released dimer, but that the clutch-tubulin dimer association is half as favorable such that:

$$\Delta G' = \frac{\Delta G^\circ}{2} \quad \text{(Eq. 3-9)}$$

where ΔG° is the free energy of bonding between the clutch and the MT lattice. Given that:

$$\Delta G^\circ = -k_BT \cdot \ln\frac{k_{on}}{k_{off}} \quad \text{(Eq. 3-10)}$$

solving for the dissociation rate of an interdimer associating linker from a single tubulin dimer yields:

$$k_{off}' = \sqrt{k_{on} \cdot k_{off}} \qquad \text{(Eq. 3-11)}$$

Model Methodology

We set up a Monte-Carlo simulation with the kinetics described above using an event stepping method with variable time increments. Briefly, at every event step, times for all possible events are calculated as:

$$t_j = \frac{\ln(1 - p_j)}{k_j} \qquad \text{(Eq. 3-12)}$$

where k_j is the rate constant of event j, and p_j is a random number from 0 to 1. Valid events include association/dissociation from the MT, diffusion along the MT-lattice, and dissociation of released tubulin dimers from disengaged clutches.

Once all event times are calculated, the event with the shortest time is executed. In the case of diffusion along the microtubule, an additional test is performed to determine the direction of stepping as indicated in Eq 3-8. Once the event is executed, forces are balanced in the reference frame of the rigid kinetochore to determine its change in position by:

$$\Delta x_{kin} = \frac{F_{Load} - \kappa_c \cdot \sum_i^{n_{eng}} \left(x_{clutch(i)} \right)}{n_{eng} \cdot \kappa_c} \qquad \text{(Eq. 3-13)}$$

where F_{load} is the load resisting the motion of the kinetochore, and n_{eng} is the number of engaged clutches.

Once the forces have been balanced, the MT shortens by:

$$\Delta x_{MT} = v_{depoly} \cdot dt \qquad \text{(Eq. 3-14)}$$

where v_{depoly} is the depolymerization velocity of the MT, and dt is the minimum of event times, t_j. Any engaged clutches that disengaged due to this depolymerization step are set to the inactive state for the next event step.

This process is repeated for a total of 10^7 event steps, until all clutches disengage from the MT, or until 20 s of simulated time is reached.

Model Parameters

Values and sources of model parameters used in simulation are listed in Table 3-1. Ranges of values for parameters that are not well established experimentally were estimated on theoretical grounds.

Estimation of clutch-tubulin association rate, k_{on}

Since we assume the molecular clutch remains bound to the kinetochore throughout the simulation, tubulin and clutches remain closely apposed to one another even when not directly associated. This could theoretically lead to very high association rates. Experimentally measured association rates when the target protein is fixed are typically on the order of 10^5-10^7 M^{-1} s^{-1} [75, 125, 126]. In order to estimate the pseudo first order rate constant on a molecular clutch fixed in the vicinity of a tubulin lattice, we estimated the concentration of tubulin binding sites in the search volume one molecular clutch would occupy due to thermal motion. Assuming a clutch spring constant, κ_c, of 1 pN/nm, at two standard deviations, we estimate a search volume of ~23 nm^3. Assuming the molecular clutch has access to tubulins on one half of the microtubule surface, approximately 4 tubulin binding sites would be within this

search volume. Therefore, we estimate the concentration of tubulin sites to be ~2×10^{-1} sites/nm^3 or about ~0.33 M. Thus, a pseudo first order rate constant of two apposing surfaces would be in excess of 10^5 s^{-1}. In order to make this problem computationally tractable, we set the pseudo first order association rate of a molecular clutch to the tubulin lattice to be 1×10^4 s^{-1}.

Estimation of MT-lattice diffusion rate, k_{diff}

The diffusion coefficient of a typical protein in water is on the order of ~10 $\mu m^2/s$ [75]. From this, the time it would take for a kinetochore-clutch to diffuse 8 nm to the next tubulin association site in one dimension, is:

$$\tau = \frac{\Delta x^2}{2D} \qquad \text{(Eq. 3-15)}$$

where Δx is the step size of the diffusive process and D is the diffusion coefficient of the particle. From our estimate above, we calculate a diffusion time of approximately 3×10^{-6} s, or a stepping rate of 3×10^5 s^{-1}. Since this diffusive process occurs near the MT-lattice surface, we can expect the step rate to decrease by one to two orders of magnitude. In our simulations, we treat the diffusion step rate, k_{diff}, as a free parameter, varying its value from 10^1 - 10^5 s^{-1}, spanning the range of stepping rates we would expect based on the above analysis. In fact, experimental studies of the kinetochore associating Dam1 complex have estimated its MT-lattice diffusing step rate at approximating 1800-2500 s^{-1} [44]. For comparison, the simulations presented here use a step rate of 1000 s^{-1}.

3.4 Results

3.4.1 Stochastic Model of Kinetochore-Clutch Adhesion Dynamics

The Ndc80 and Dam1 complexes have both been found to directly interact with microtubules, forming an essential link that couples the dynamics of microtubules to chromatid segregation [28, 35]. Recent advances have allowed, for the first time, detailed characterization of these complexes indicating their site of MT association [34, 127], and unique properties, such as MT-lattice diffusion, in the case of Dam1 [44].

To build our understanding of how these properties promote attachment and persistent end-tracking of depolymerizing microtubules, we constructed a stochastic model of kinetochore attachment mediated through molecular clutches (Figure 3-1). Briefly, we treat molecular clutches as Hookean springs that can reversibly engage a MT. Stably attached clutches develop strain with kinetochore motion, building tension that increases their dissociation rate according to a Bell model [58]. We also constructed the model such that clutches could diffuse along the MT-lattice. To determine how the location of clutch-tubulin association affected kinetochore end-tracking, we allowed clutches either of two modes association: (1) intradimer association, where the clutch binds within a single tubulin unit, or (2) interdimer association, where the clutch is only allowed to bind along the interface between tubulin units. This mainly affects the distal portion of the kinetochore where MT plus-end depolymerization might release tubulin along with an associated clutch. Differences in the location of tubulin association leads to altered clutch dissociation rates from the individual tubulin dimers. From these simulations, we can visualize and quantitatively measure how a kinetochore tracks a depolymerizing MT under load.

3.4.2 MT-lattice diffusion expands the parameter space of successful kinetochore end-tracking

To determine what effect MT-lattice diffusion might have on kinetochore end-tracking, we first simulated a kinetochore-clutch system comprised of intradimer associating clutches lacking MT-lattice diffusion at a load force of 3 pN (Figure 3-2a). Interestingly, in these non-diffusive kinetochore-clutch systems, we noted that clutches along the proximal portion of the kinetochore tended to exhibit large positive strains (Figure 3-3a). These configurations developed since the clutch tail, fixed to a moving kinetochore, moved past its stationary MT-associating head as the kinetochore tracked with the depolymerizing MT. Clutches in these configurations tended to be in the proximal portion of the kinetochore, and produced a 'detachment' force that resisted kinetochore-MT overlap (Figure 3-3b). When we simulated over a range of dissociation rates and clutch stiffness at a load force of 3 pN, we noted that non-diffusive intradimer kinetochore-clutch systems maintained attachment in only a narrow range of the parameter space (Figure 3-2c).

In contrast, simulations with diffusion of intradimer kinetochore-clutches with the same parameters showed lower proximal clutch strains and deeper MT insertion (Figure 3-2b). Since clutches were allowed to diffuse along the MT-lattice, they tended to diffuse in the direction that relaxed stretching. This reduces the strains along proximal clutches, lowering the overall detachment force (Figure 3-3b). Lower bond stresses also had the effect of increasing bond-lifetimes, thus increasing the average number of engaged clutches (Figure 3-3c). Therefore, the ability of molecular clutches to diffuse along the MT-lattice reduces detachment forces by relaxation, dramatically

expanding the range where MT-lattice diffusing kinetochore-clutch systems successfully end-tracked (Figure 3-2d).

To determine what effect allowing MT-lattice diffusion had on the maximum force an intradimer kinetochore-clutch system could support, we simulated kinetochore end-tracking over the entire parameter space while increasing the load force. In the case of intradimer kinetochores lacking diffusive clutches, we found that the optimal system had high dissociation rate (k_{off}=100 s^{-1}) and soft clutches (κ_c=0.1 pN/nm) and could only support a maximum force of 3 pN (Figure 3-4a). In contrast, with MT-lattice diffusion, the optimal kinetochore-clutch system was able to support a maximum load of 18 pN (Figure 3-4b). Since MT-lattice diffusion minimized proximal clutch detachment forces over a broad range, diffusive systems are able to utilize stiffer clutches (κ_c=10 pN/nm) with longer-lived bonds (k_{off}=0.1 s^{-1}). This has the effect of creating longer-lived attachments that remain close to the MT plus-end, increasing the number of clutches able to bind the MT to resist detachment. Furthermore, switching from a non-MT-lattice diffusing kinetochore system to a system with MT-lattice diffusion greatly increased the parameter space over which we observed successful end-tracking (Figure 3-4c,d). Together, these results show that MT-lattice diffusion significantly improves the ability of kinetochore-clutch systems to maintain attachments and bear loads by reducing detachment forces and increasing MT-clutch bond lifetimes.

3.4.3 Interdimer association prevents clutch poisoning

Next, we tested to see how the site of clutch-tubulin association alone affected kinetochore-clutch adhesion dynamics by comparing intradimer associating

kinetochore-clutch systems with interdimer associating kinetochore-clutch systems without the effects of MT-lattice diffusion. From the previous simulations of non-diffusive intradimer kinetochores, we had noted that a number of the distal clutches shifted into an inactive state as engaged clutches released from the plus-end due to MT depolymerization (Figure 3-2a). In the case of intradimer associating clutches, the released tubulin dimer and clutch have the same affinity for one another as when the tubulin was part of the MT-lattice. Thus, the clutches and released tubulin dimers remain associated from some time, effectively 'poisoning' a significant number of clutches and rendering them unable to rebind the MT to promote attachment.

As expected, interdimer kinetochore systems lacking MT-lattice diffusion also exhibited strained proximal clutches similar to non-diffusive intradimer systems. Interestingly, we noted a substantial decrease in the number of inactive "poisoned" clutches in the distal portion of interdimer kinetochore-clutch systems (Figure 3-5a, Figure 3-2a). In this case, the release of tubulin dimers from the MT-lattice due to depolymerization eliminates the interdimer interface the clutch prefers. This dramatically increases the dissociation rate of the released tubulin dimer from the clutch, decreasing the time spent in the inactive state. This rapid 'recycling' of inactive clutches allows a greater portion of distal clutches to engage the MT (Figure 3-5b). As a result, interdimer associating kinetochore systems are predicted to have deeper MT insertions and successfully end-track over a wider range of parameter space when compared with a similar system of intradimer associating clutches working against a load force of 3 pN (Figure 3-5c, Figure 3-2c).

Following this result, we then increased the loads on interdimer associating kinetochores to determine whether this mode of association increased or decreased the maximum sustainable loads. While the optimal non-diffusing intradimer kinetochore only supported a maximum load of 3 pN (Figure 3-4a), an optimal non-diffusing interdimer kinetochore is able to support loads up to 12 pN (Figure 3-7a). Interestingly, the optimal parameters for an interdimer associating kinetochore shifts slightly, preferring somewhat stronger bonds (k_{off}=10 s^{-1}) with soft clutches of equal stiffness (κ_c=0.1 pN/nm) compared with non-diffusing intradimer systems (white box, Figure 3-5c; yellow box, Figure 3-2c). Since the distal clutches of interdimer bonds recycle more quickly to an active state, more distal clutches engage the MT, producing larger attachment forces (Figure 3-5b, Figure 3-6). Switching from a non-MT-lattice diffusing intradimer kinetochore system to a system with interdimer associating clutches greatly increased the parameter space over which we observed successful end-tracking (Figure 3-4c, Figure 3-7b). Thus, interdimer systems can utilize clutches with longer-lived clutch-tubulin association without dramatically increasing the number of clutches that end up in the inactive state, allowing these systems to sustain greater loads.

These simulation results show that the ability of a kinetochore-clutch to recognize the interdimer interface, rather than the intradimer interface, provides a significant advantage in that clutches will have an innate preference for the polymer form of tubulin, quickly dissociating from tubulins released from the MT-lattice. This increases the number of distal clutches able to bind to the MT in productive coupling, resulting in stronger adhesions over a wider range of parameter space.

3.4.4 A kinetochore of interdimer associating, MT-lattice diffusing clutches end-tracks most robustly

Finally, we simulated a kinetochore-clutch system with both MT-lattice diffusion and interdimer association at 10 pN of load force to determine whether possessing both properties would be beneficial to attachment and end-tracking (Figure 3-8a). We found that increasing the load force shifted the optimal parameter set and reduced the valid parameter space for MT-lattice diffusing intradimer systems (Figure 3-10). When we switched to interdimer tubulin association, kinetochores were again able to end-track over a wide parameter space (Figure 3-8b). When we simulated over the entire parameter space to determine the maximum load forces that this system could sustain, we found that the optimal interdimer MT-lattice diffusing system used long lived bonds (k_{off}=0.1 s^{-1}) with stiff clutches (κ_c=10 pN/nm) (Figure 3-8c). Systems with interdimer MT-lattice diffusing clutches were able to withstand forces up to 32 pN of load and were able to successfully end-track over the widest range of parameter space (Figure 3-9a,b). Furthermore, these systems also tracked MTs depolymerizing at faster rates (Figure 3-11), demonstrating that these systems could play a role in end-tracking in a number of model cell systems. Thus, combining the effects of decreased detachment forces of proximal clutches and reducing the time distal clutches spend in an inactive state further helps kinetochore systems to maintain better attachment and support greater loads. From these simulations, we find that a kinetchore possessing clutches that both diffuses over the MT-lattice and binds the interdimer interface results in a robust kinetchore that is able to successfully maintain attachment over the widest range of forces.

In summary, in this theoretical investigation, we explore what properties are important for successful MT end-tracking. We find that when molecular clutch dynamics are too slow, proximal clutches tend to produce a detachment force while distal clutches tend to shift into an inactive state. Simulations suggest that evolution has solved these problems with a multifaceted approach. First, by allowing molecular clutches to diffuse along the MT-lattice, detachment forces are minimized while still maintaining attachment to the MT. Second, preferential tubulin interdimer clutch association confers a built-in mechanism for recognizing tubulin polymer, allowing distal clutches to rapidly recycle into an active state. We find that a kinetochore system of MT-lattice diffusing, interdimer-associating clutches end-tracks over the widest parameter space and supports the greatest loads, allowing such a system to robustly maintain end on attachment while quickly responding to changes in load throughout mitosis.

3.5 Discussion

A number of recent models have focused on the Dam1 ring and how it may be the ideal coupling device [41-43]. These 'conformational wave' or 'forced-walk' models postulate that the formation of a ring around MTs can convert the curling of protofilaments into work as the MT depolymerizes. Since the motion in this system is driven by the free energy released by GTP hydrolyses, theoretical considerations suggest that this mechanism can produce sufficient forces to pull chromosomes apart. While these results are appealing, the lack of observed rings *in vivo*, even under conditions where they should have been easily detected, brings into question the

importance of such a mechanism. Furthermore, recent studies have demonstrated end-tracking by individual Dam1 complexes [44], further bringing doubts on the significance of a ring mechanism.

Based on recent electron tomography results, another study suggests that kinetochore attachment is mediated by long fibrils connected directly to the inner kinetochore [128]. They go on further to model this attachment as mediated by long flexible linkers, in a similar manner to our model, but with significant differences in key assumptions. First, the arrangement of the fibril model necessitates that molecular clutches strain along their axial dimension. In contrast, we model clutches as bending transversely, similar to beam bending, which should require significantly less energy. As such, the search volumes of flexible clutches in the transverse direction due to thermal motion would be significantly larger than in the axial direction. This suggests that large amounts of energy would be require for a fibril to rebind the MT once dissociated. Furthermore, in the fibril model, affinity for the MT was modeled with association rates only, with the assumption that dissociation occurs instantaneously only after tubulin depolymerization from the lattice. This ignores biochemical data, which suggests that molecular clutches have finite affinities for MTs on the order of 1-10 nM [44, 129] and assumes MT depolymerization is very fast, compared to clutch dissociation.

In this work, we present analysis of a kinetochore-clutch model of attachment and end-tracking, incorporating the fundamental concepts of Hill's sleeve model, with newly discovered molecular clutch properties. In place of a sleeve of binding sites that must bind and rebind in concert, we model coupling as being mediated by long, spring-

like clutches that independently associate/dissociate from the MT and provide enough space for tubulin exchange. Interestingly, our proposed system also possesses a barrier to insertion, similar to Hill's model, in the form of clutches that produce a detachment force leading to a steady-state insertion that tracks with MT depolymerization. Results from this study suggest that kinetochore-clutches that diffuse along the MT-lattice, such as Dam1, may lower this barrier by relaxing strains along individual linkers, an effect not predicted by other models.

We also account for clutch associations with tubulins recently released from the MT-lattice, an effect that has been widely ignored. If a coupling molecule has affinity for a site within a tubulin dimer, then a clutch associated with a tubulin dimer that recently depolymerized from the lattice would remain associated. Dam1 complexes have affinity for free tubulin *in vitro*, suggesting that these effects need to be considered [44]. Indeed, our theoretical studies find that intradimer associating kinetochore-clutch systems support less load due to poisoning of distal clutches released from the MT plus-end. Thus, our results provide a natural explanation for the functional significance in the recent findings of strong Ndc80 binding to the interdimer interface [34].

When both these effects work in concert, we find that a kinetochore-clutch system can withstand loads of up to 32 pN, significantly greater than those reported in Hill's study. These effects are likely due to the relaxation of the detachment force by diffusion, which significantly lowers the insertion barrier. Furthermore, we also consider the close apposition of binding surfaces distributed across two dimers, which greatly increases the effective association between the two surfaces. This has the effect of greatly increasing the free energy of the system, suggesting that biased diffusion

models may be able to support greater loads than previously considered. These estimates of load are still lower than the required force to stall kinetochore motion in grasshopper spermatocytes, but are still consistent in that multiple MTs insert into kinetochores of higher eukaryotes.

In summary, we find that both MT-lattice diffusion and tubulin interdimer recognition are important features for a robust kinetochore coupler. While MT-lattice diffusion is faster than the build-up of tension along an individual clutch, diffusion will prolong the lifetime of that bond by relieving the stress along the linker. Interdimer bonding further helps kinetochore attachment, building in a mechanism for recycling clutches occupied by depolymerized tubulin. In this way, a MT-lattice diffusing interdimer kinetochore-clutch can maintain stable attachment to dynamic MTs under load.

3.6 Acknowledgements

This research was supported by the National Science Foundation (MCB-0615568), and the National Institute of General Medical Sciences (R01-GM-76177). We thank members of the Odde Lab, Melissa Gardner and Erkan Tuzel for stimulating discussions and technical assistance.

3.7 Tables and Figures

Table 3-1 Parameters of the Stochastic Kinetochore-Clutch Model.

Model Parameter	Description	Typical Value	Source
v_{depoly}	Microtubule depolymerization rate	-20 nm/s	Free parameter; Can vary widely; 20-300 nm/s
n_c	Number of clutches along the kinetochore	32	Half of Hill's number to allow MT dynamics; in yeast 10-18 clutches per MT [117]
L_{kin}	Length of the kinetochore	40 nm	Depth of outerplate, 35-40 nm [130]
k_{on}	Pseudo first-order rate constant for clutch-tubulin association	10000 s^{-1}	Estimated in this study; *See Methods*
k_{off}	Pseudo first-order rate constant for clutch-tubulin dissociation	0.01-1000 s^{-1}	Free parameter; typical range for Dam1 0.06-1.2 s^{-1} [44]
F_b	Characteristic clutch-tubulin bond rupture force	2 pN	Not well establish; 2 pN for an actin clutch [115]
k_{diff}	Clutch-MT-lattice diffusion rate constant	10-10000 s^{-1}	Free parameter; Estimated in this study; typical values ~2500 s^{-1} for Dam1 [44]
δ	Clutch diffusion step size	8 nm	Length of a tubulin dimer
κ_c	Clutch spring constant	0.1-100 pN/nm	Free parameter; Fisher et al., 1999, on the order of pN/nm [116]
F_{load}	Load force due to chromatin resistance	0-30 pN	700 pN over 10-25 MTs [123]

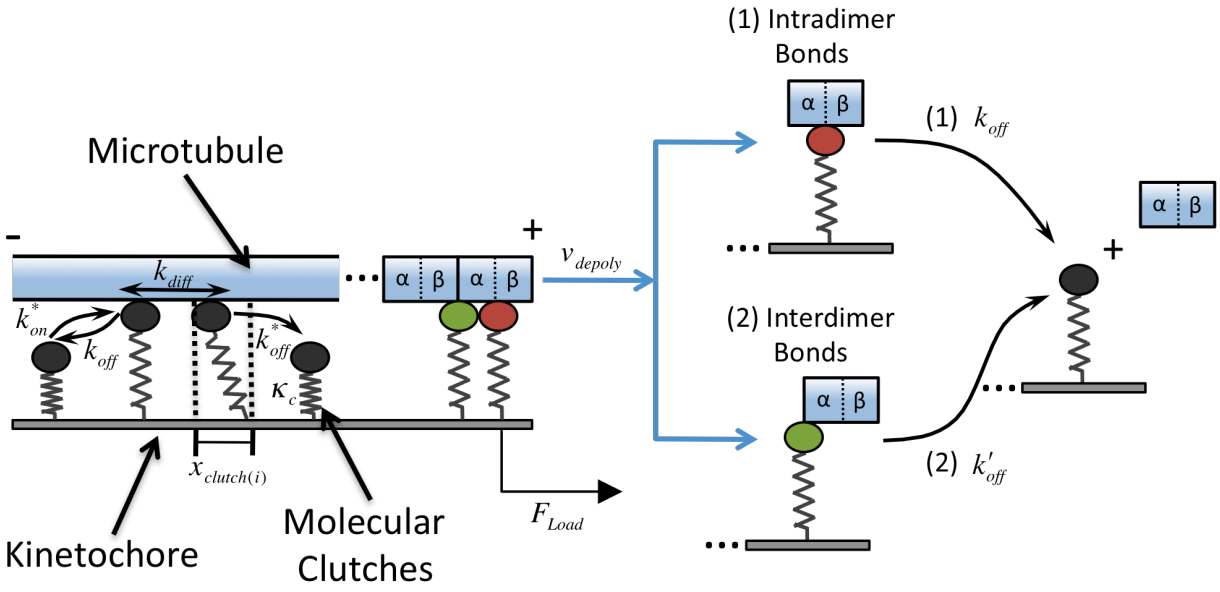

Figure 3-1 Schematic representation of a molecular kinetochore-clutch model. Molecular clutches reversibly associate with a MT with rates k_{on} and k_{off}. Tracking of the depolymerizing MT plus end by the kinetochore against load force, F_{load}, stretches engaged clutches by $x_{clutch(i)}$, imparting a force due to the stiffness of the clutch κ_c, increasing its effective dissociation rate to k_{off}*. In some cases, diffusion along the MT-lattice is allowed at rate, k_{diff}. At the plus-end, depolymerization of the MT occasionally releases engaged clutches still associated with tubulin dimers. These clutches remain 'inactive' until the associated tubulin dissociates with rate k_{off}, in the case of systems with intradimer binding, or k_{off}', in systems where clutches prefer interdimer binding.

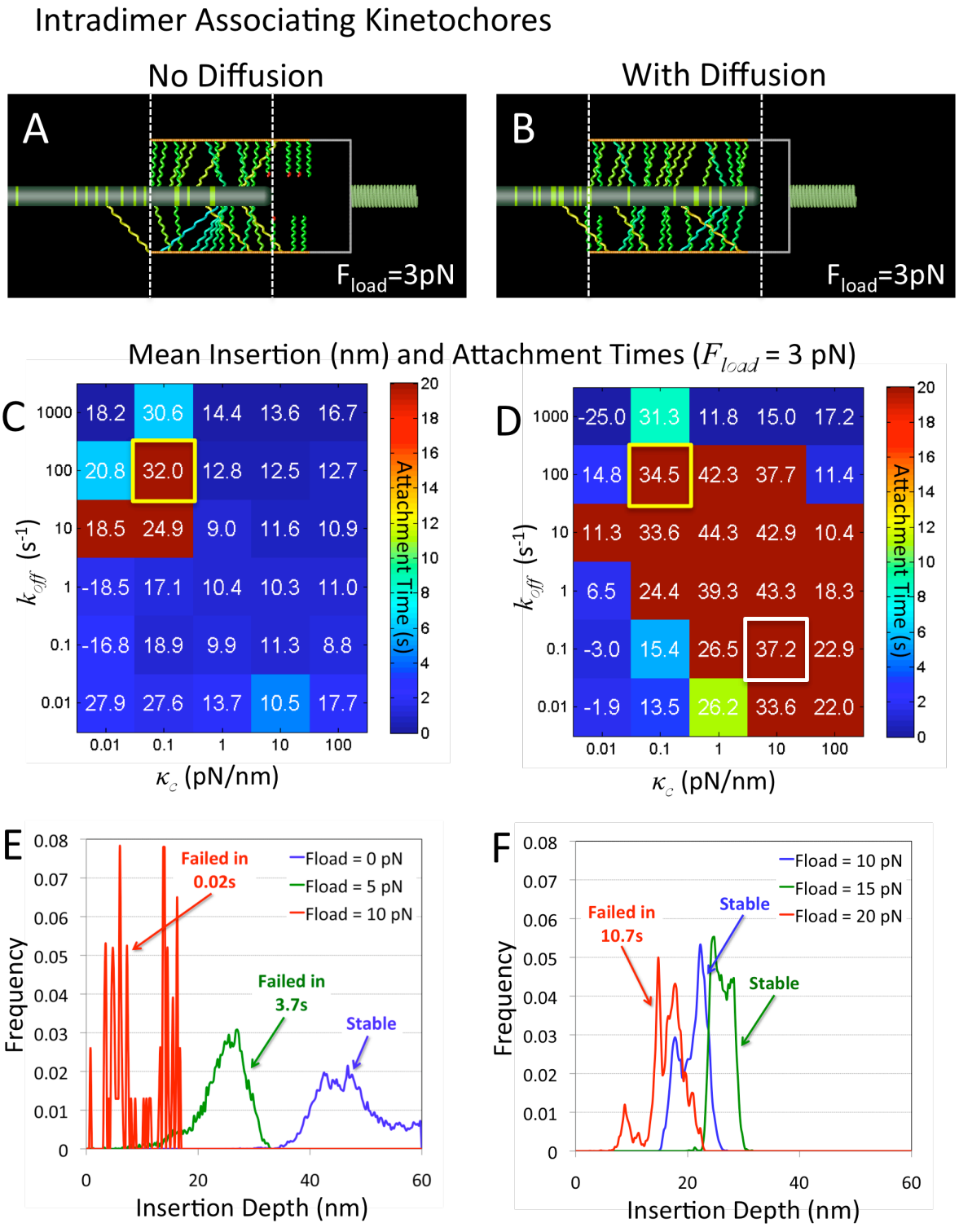
Intradimer Associating Kinetochores
No Diffusion
With Diffusion
A
B
F_load=3pN
F_load=3pN
Mean Insertion (nm) and Attachment Times (F_load = 3 pN)
C
D
k_off (s^-1)
κ_c (pN/nm)
Attachment Time (s)
1000 18.2 30.6 14.4 13.6 16.7
100 20.8 32.0 12.8 12.5 12.7
10 18.5 24.9 9.0 11.6 10.9
1 -18.5 17.1 10.4 10.3 11.0
0.1 -16.8 18.9 9.9 11.3 8.8
0.01 27.9 27.6 13.7 10.5 17.7
1000 -25.0 31.3 11.8 15.0 17.2
100 14.8 34.5 42.3 37.7 11.4
10 11.3 33.6 44.3 42.9 10.4
1 6.5 24.4 39.3 43.3 18.3
0.1 -3.0 15.4 26.5 37.2 22.9
0.01 -1.9 13.5 26.2 33.6 22.0
0.01 0.1 1 10 100
0 2 4 6 8 10 12 14 16 18 20
E
F
Frequency
Insertion Depth (nm)
Failed in 0.02s
Failed in 3.7s
Stable
Failed in 10.7s
Stable
Stable
Fload = 0 pN
Fload = 5 pN
Fload = 10 pN
Fload = 10 pN
Fload = 15 pN
Fload = 20 pN
0 0.01 0.02 0.03 0.04 0.05 0.06 0.07 0.08
0 20 40 60

Figure 3-2 Molecular clutch MT-lattice diffusion improves kinetochore tracking.
(A&B) Representative images of a simulated kinetochore of intradimer associating clutches without and with MT-lattice diffusion, respectively (k_{off}=100 s^{-1} and κ_c=0.1 pN/nm, yellow boxes **C** & **D**). (C & D) Mean MT insertion into the kinetochore and attachment times for an intradimer associating kinetochore without diffusion and with diffusion at F_{load}=3 pN, respectively. Mean insertions (white text) and attachment times (color tiles) as a function of k_{off} and κ_c. (E & F) Distribution of MT insertion depths of optimal intradimer kinteochores without and with MT-lattice diffusion (yellow box in **E**, white box in **F**, respectively) as a function of load force.

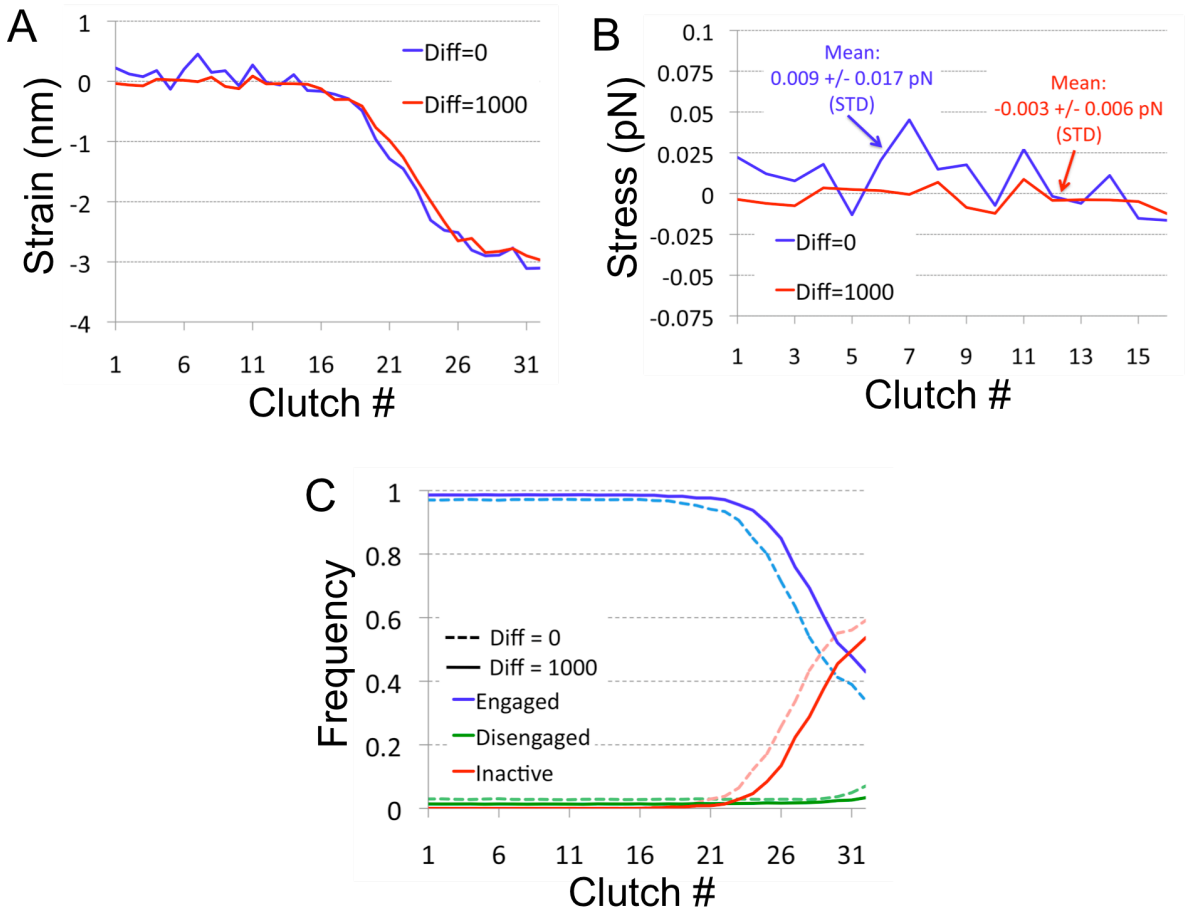

Figure 3-3 MT-lattice diffusion relieves clutch stress increasing the frequency of engagement.
(A) Clutch strains as a function of position along the kinetochore with and without MT-lattice diffusion. (B) Proximal clutch stress as a function of position with and without MT-lattice diffusion. (C) Clutch state frequencies with of without MT-lattice diffusion. All simulations using k_{off}=100 s^{-1}, κ_c=0.1 pN/nm, and F_{load}=3 pN.

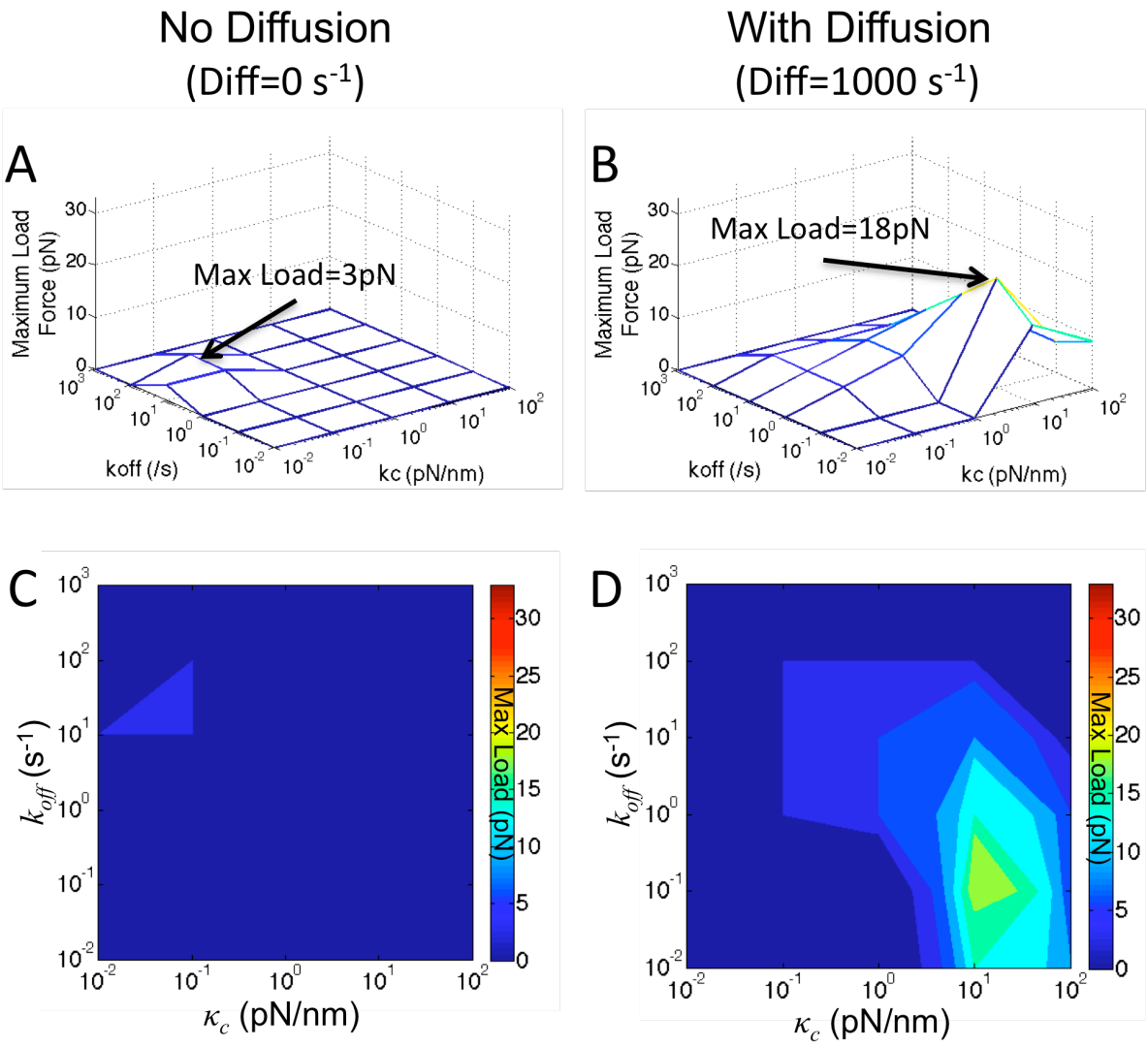

Figure 3-4 Kinetochore systems with MT-lattice diffusion support greater loads over a wider range of parameter space.
(A & B) Maximum sustainable loads as a function of k_{off} and κ_c for intradimer kinetochore system without and with MT-lattice, respectively. (C & D) Top-down view of the maximum sustainable loads as a function of k_{off} and κ_c for intradimer kinetochore system without and with MT-lattice, respectively. Color indicates largest load where attachment was maintained for at least 20 s.

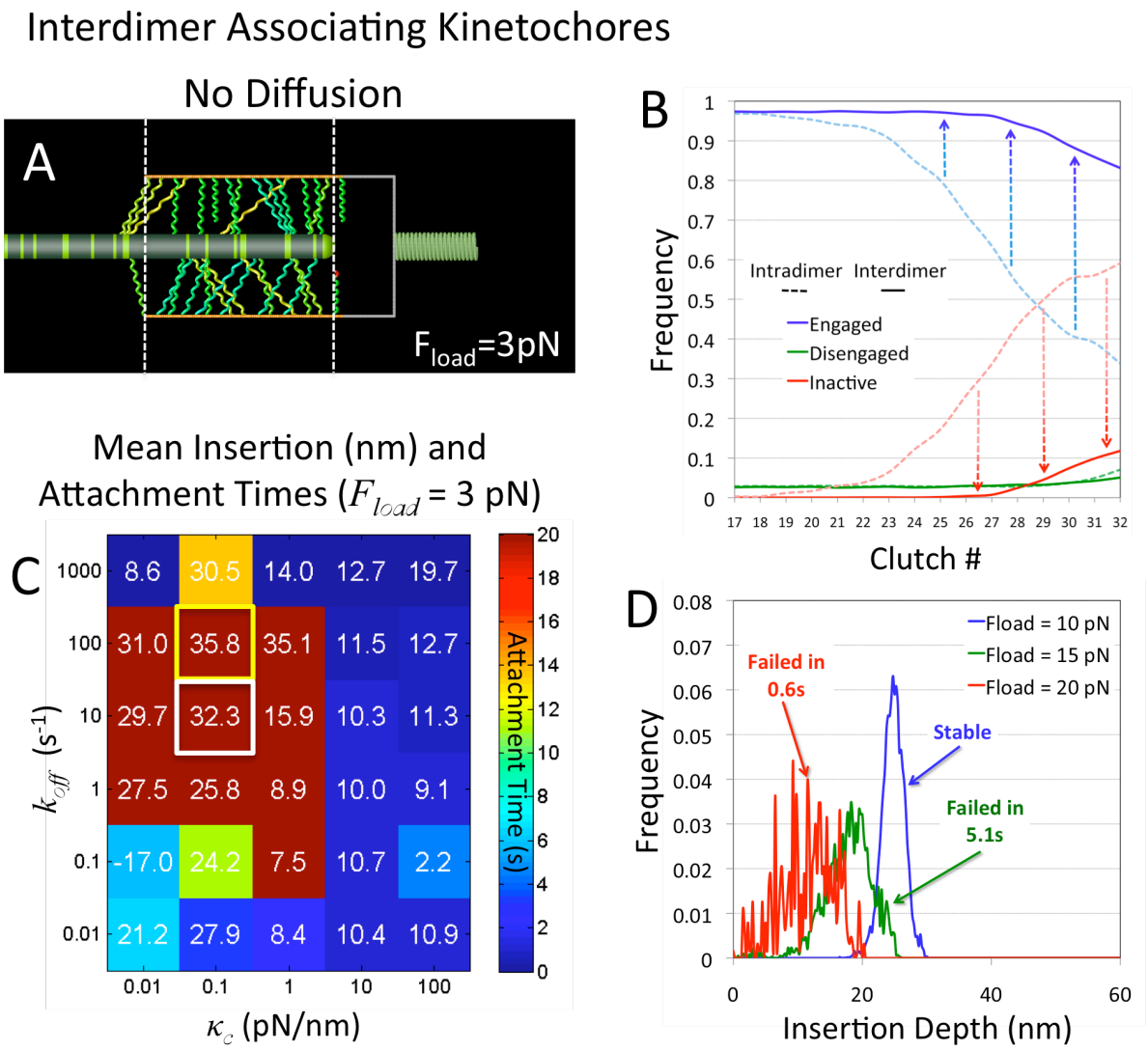

Figure 3-5 Interdimer associating clutches improve MT end-tracking by recycling inactive clutches. (A) Representative image of a simulated kinetochore of interdimer associating clutches with no diffusion (k_{off}=100 s^{-1} and κ_c=0.1 pN/nm, yellow box in **C**). (B) Frequency of engaged, disengaged and inactive states for distal kinetochore clutches for intradimer associating clutches and interdimer associating clutches (k_{off}=100 s^{-1} and κ_c=0.1 pN/nm, yellow box, **Fig 2B**, yellow box in **C**, respectively). (C) Mean MT insertion into the kinetochore and attachment times for an interdimer associating kinetochore without diffusion at F_{load}=3 pN. Mean insertions (white text) and attachment times (color tiles) as a function of k_{off} and κ_c. (D) Distribution of MT insertion depths of the optimal interdimer kinteochore without MT-lattice diffusion (white box in **C**) as a function of load force.

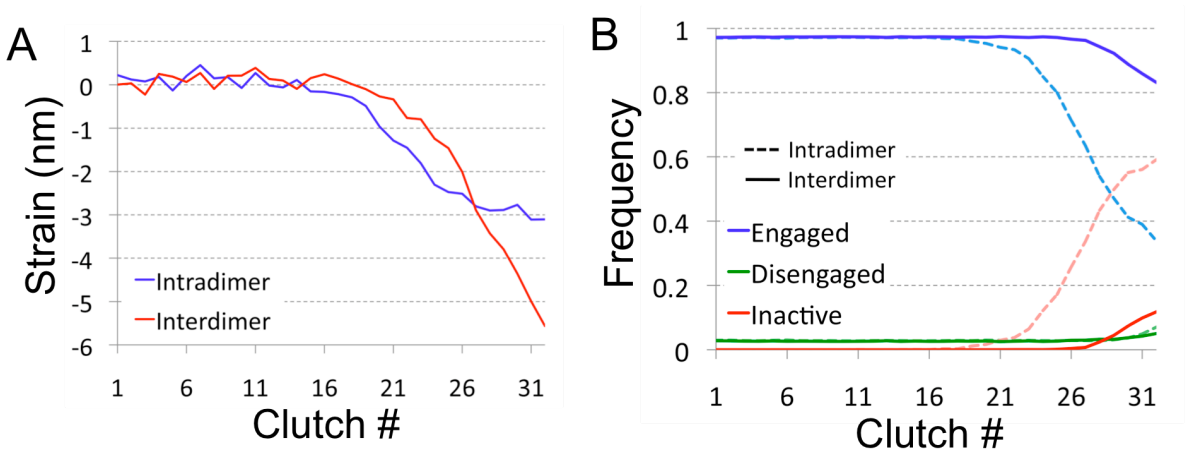

Figure 3-6 Interdimer associating kinetochores quickly recycles inactive distal clutches.
(A) Clutch strains of kinetochores of either intradimer or interdimer associating clutches as a function of position. (B) Clutch state frequencies of kinetochores of intradimer or interdimer associating clutches. All simulations using k_{off}=100 s^{-1}, κ_c=0.1 pN/nm, and F_{load}=3 pN.

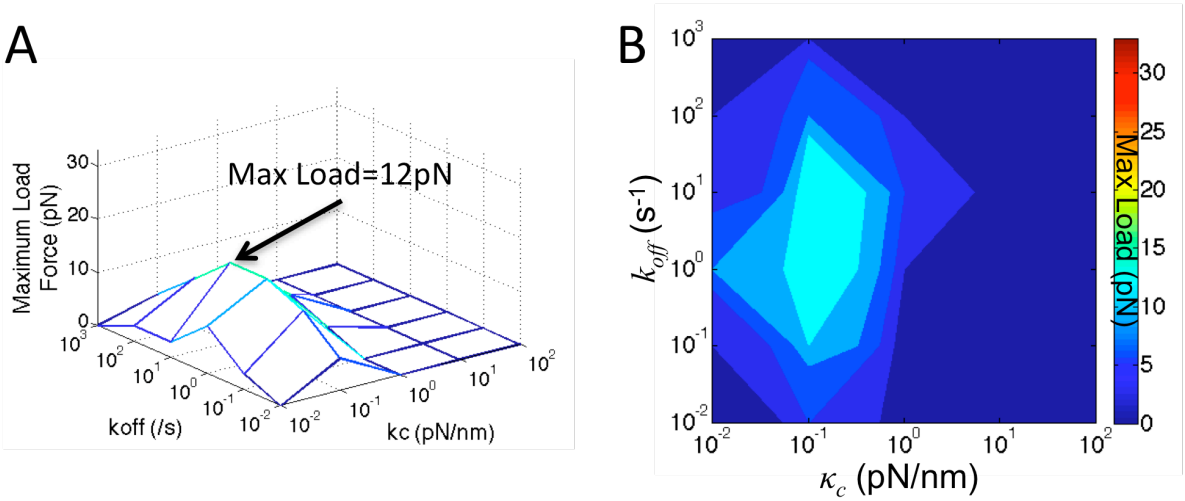

Figure 3-7 Kinetochore systems with interdimer associating clutches support greater loads over a wider range of parameter space.
(A) Maximum sustainable loads as a function of k_{off} and κ_c for an interdimer kinetochore system without MT-lattice. (B) Top-down view of the maximum sustainable loads as a function of k_{off} and κ_c for an interdimer kinetochore system without MT-lattice. Color indicates largest load where attachment was maintained for at least 20 s.

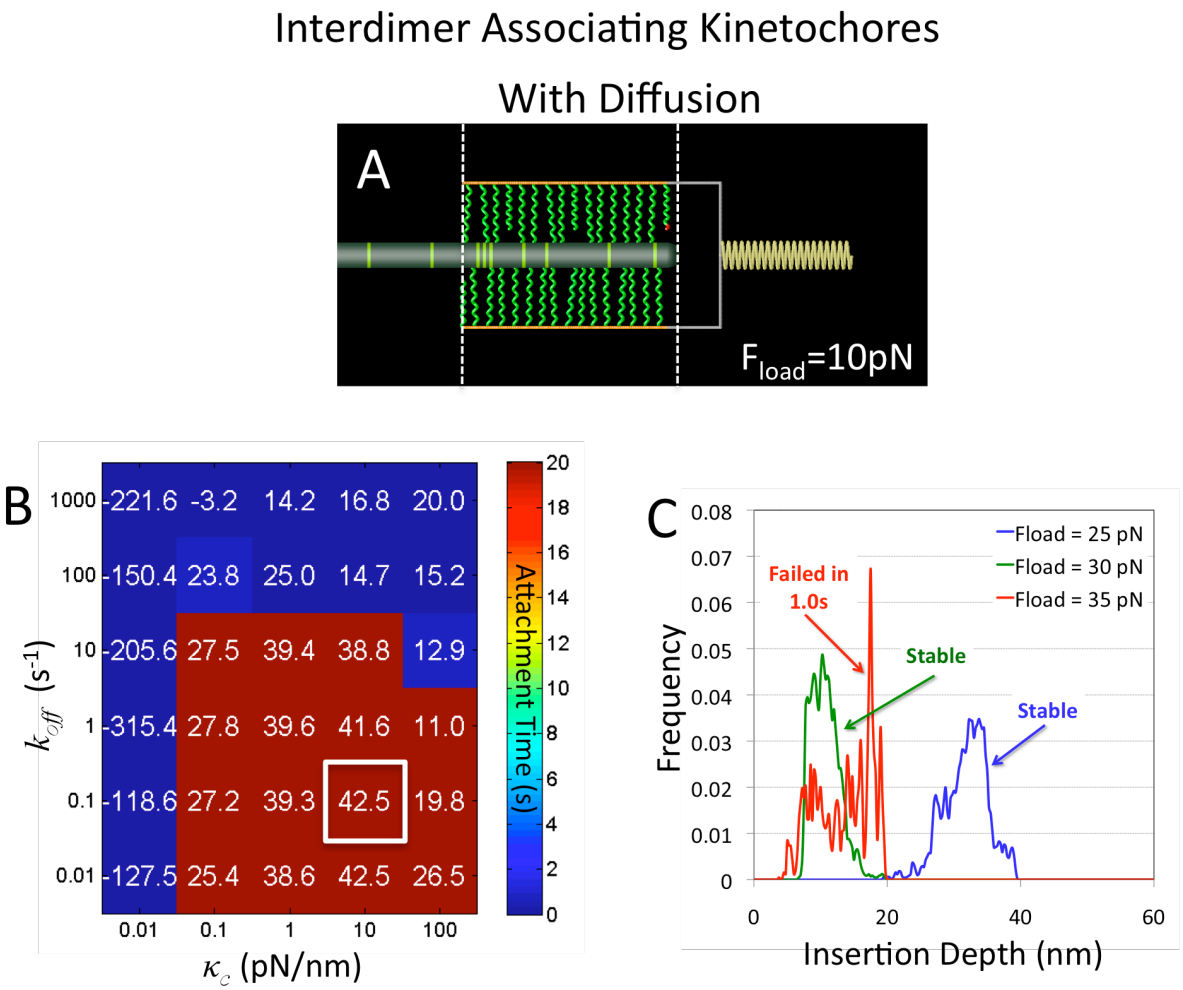

Figure 3-8 A kinetochore of MT-lattice diffusing interdimer associating clutches supports the greatest loads.

(A) Representative image of a simulated kinetochore of interdimer associating clutches with MT-lattice diffusion (k_{off}=0.10 s^{-1} and κ_c=10 pN/nm, white box in **B**). (B) Mean MT insertion into the kinetochore and attachment times for an interdimer-MT-lattice diffusing kinetochore at F_{load}=10 pN. Mean insertions (white text) and attachment times (color tiles) as a function of k_{off} and κ_c. (C) Distribution of MT insertion depths of the optimal interdimer MT-lattice diffusing kinteochores as a function of load force.

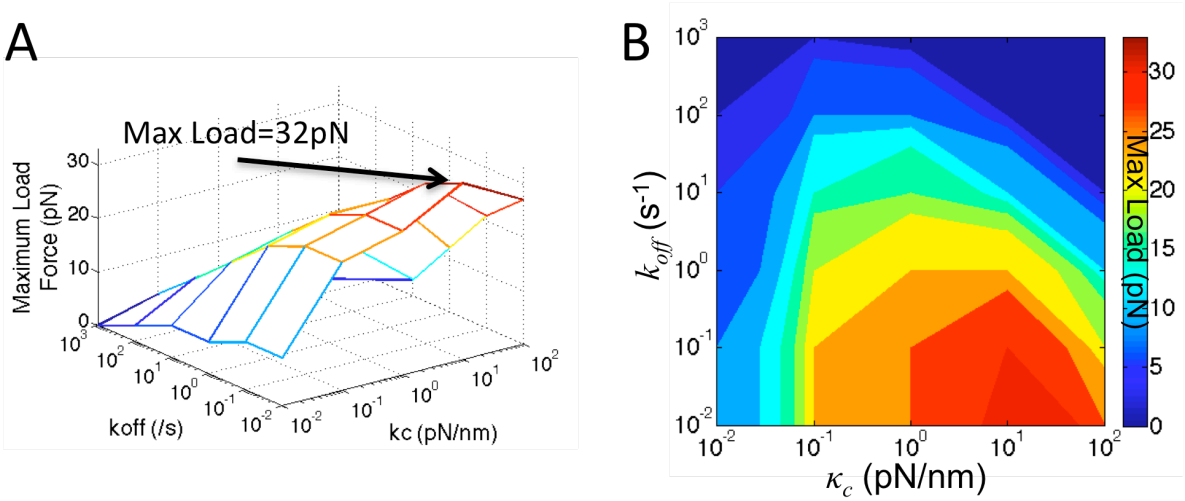

Figure 3-9 Kinetochore systems with interdimer associating clutches that diffusion along the MT-lattice support the greatest loads over a wider range of parameter space.
(A) Maximum sustainable loads as a function of k_{off} and κ_c for a MT-lattice diffusing interdimer kinetochore system. (B) Top-down view of the maximum sustainable loads as a function of k_{off} and κ_c for a MT-lattice diffusing interdimer kinetochore system. Color indicates largest load where attachment was maintained for at least 20 s.

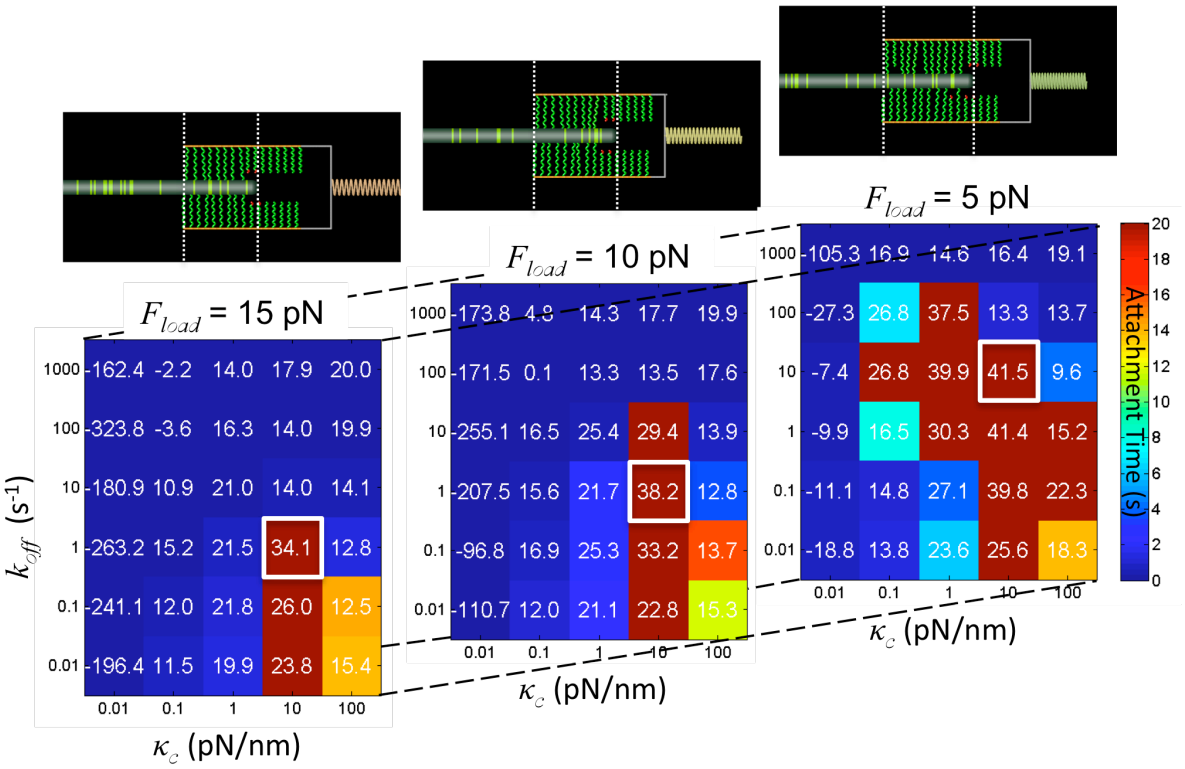

Figure 3-10 Increasing loads reduces the valid parameter space and shifts the optimum. Representative images of optimal kinetochore systems of intradimer associating clutches with MT-lattice diffusion (top row). Mean MT insertion into the kinetochore and attachment times for intradimer-MT-lattice diffusing kinetochore systems from 5-15 pN of load (bottom row). Mean insertions (white text) and attachment times (color tiles) as a function of k_{off} and κ_c. Optimal parameter set (white box).

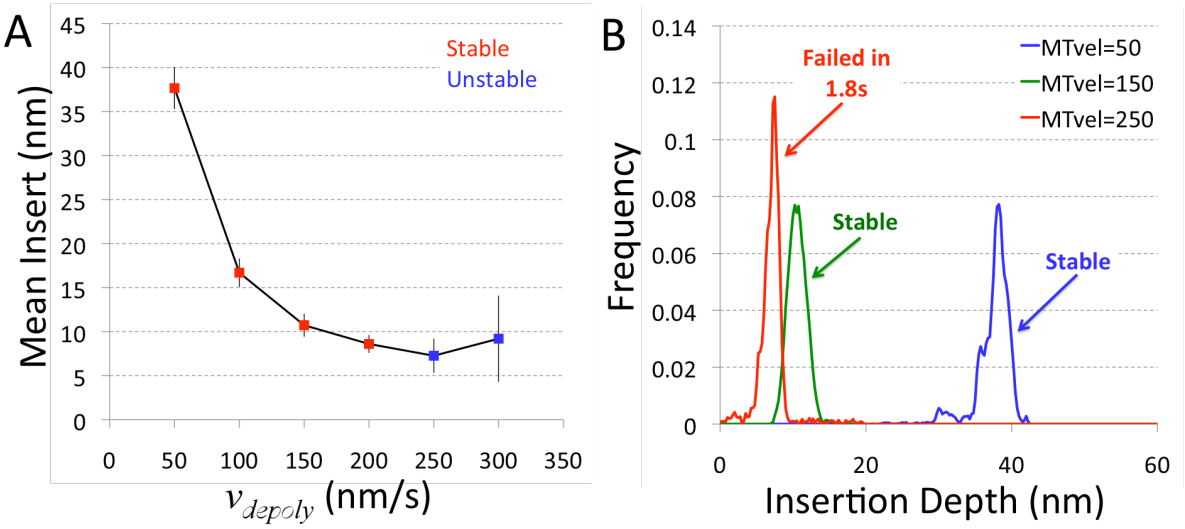

Figure 3-11 An interdimer MT-lattice diffusing kinetochore-clutch system end-tracks at high MT depolymerization rates.

(A) Mean insertion depth as a function of MT depolymerization velocity. (B) Distribution of MT-insertion depths for v_{depoly}=50, 150, and 250 nm/s.

- CHAPTER 4 -
SUMMARY AND CONCLUSIONS

Advances in imaging and genetic manipulation of cellular systems has led to a plethora of data, suggesting complex regulatory networks that control cell behavior and fate. The field of "systems biology" seeks to reduce this complexity by utilizing computational approaches to identify the key features of these mechanisms. Cellular adhesions provide a unique opportunity to study the interface of biochemistry and physics, where chemical reactions alter the physical output of a system.

In chapter 2, an integrated computational/experimental approach was used to better understand cellular motility and traction force generation on compliant substrates. Surprisingly, simulations predicted the appearance of load-and-fail dynamics on soft substrates, which altered the overall dynamics of the system. These predictions guided our experimental approach, eventually confirming the existence of load-and-fail dynamics and its effects on motor-clutch system dynamics. This data was the first direct evidence of load-and-fail dynamics, and brings further significance to the motor-clutch model of cellular motility. Furthermore, this investigation was the first to provide evidence that cellular mechanosensing might occur at the level of adhesive dynamics, a mechanism not previously considered.

In the future, it will be interesting to incorporate multiple motor-clutch modules into an integrated model for cell motility. Furthermore, focal adhesions exhibit many interesting phenomenon, such as tension-dependent strengthening thought to be

mediated through biochemical signaling originating from some mechanotransductive element found within the adhesion. We view these effects as feedback networks which can regulate certain parameters in our model. Incorporating these and other well established signaling networks into this model would build a more complete understanding of substrate adhesion and traction force generaton.

Next, we investigated kinetochore-MT attachment, an area of study that has recently seen a rapid growth in highly sophisticated data, but continues to lack a definitive mechanism for dynamic and persistent attachment. While many groups take the approach of building very specific models based on specific data, we took the approach of applying our general adhesive dynamics framework to highlight important properties that are fundamental to the process. Through this investigation, we identified specific functional consequences for molecular clutch properties that were previously not well understood. In contrast to common inference, we find that MT-lattice diffusion actually strengthens attachment to the MT by promoting increased clutch lifetimes and the numbers of bound clutches. Furthermore, we find that interdimer association is essential for recycling inactive molecular clutches, preventing the build up of poisoned clutches that would eventually lead to coupling failure.

With such rich structural data, future work will focus on incorporating a more realistic picture of the MT and its dynamics. Furthermore, it will be interesting to investigate which parameters are important for the different phases of mitosis, where kinetochore composition and dynamics may vary considerably. Lastly, evidence points to regulation of both Dam1 and Ndc80 affinity and MT-lattice diffusion coefficients by

Aurora B kinase [30, 131]. Incorporation of these and other regulatory biochemical signaling networks would be of additional interest.

In this work, I presented computational analysis of two cellular adhesion systems; (1) motor-clutch based substrate adhesion, and (2) kinetochore-clutch based attachment to MTs. Interestingly, while we modeled these adhesive systems with very similar components, the specific requirements of each system led to different properties being important for mediating system behavior. In the case of substrate adhesion, the need to sense the stiffness of the environment necessitates a system with stiffness sensitive dynamics. In this case, clutches that fail under load, and how they work cooperatively were found to be vitally important, leading to the discover of load-and-fail dynamics that respond to substrate stiffness. In the case of kinetochore attachment, coupling failure during late metaphase and early anaphase would lead to missegregation and aneuploidy [21]. For this system, maintaining attachment over a wide range of loads is most important. We found that allowing diffusion along the MT, a property that would have eliminated load-and-fail behavior altogether in the motor-clutch system, solved this problem. When challenged with maintaining attachment under load, allowing diffusion along the cytoskeletal element plays a beneficial role, relaxing the stress along individual clutches, prolonging bond lifetimes, which in turn increases the overall number of bound clutches. This distributes the load over larger numbers of clutches for robust attachment. This highlights how cells may build specialized machinery using similar mechanism with different properties for specific tasks.

In conclusion, this work illustrates the value of computational analysis in the study of complex cellular systems. When integrated with experimental approaches,

theoretical analysis can lead to surprising predictions that challenge our current understanding. In a similar manner, experimental findings shape our understanding to suggest new mechanisms that can be tested theoretically. By this iterative process we achieve improved understanding of complex cellular systems. In future work, integration of the systems presented here with other known biochemical feedback networks will bring a more complete bio-chemical-physical understanding of these important processes.

Appendix A

NANOSCALE MARKER BEAD DYNAMICS ON SOFT AND STIFF SUBSTRATES

Filopodial traction force dynamics on soft and stiff substrates

Filopodial traction force dynamics on stiff and soft substrates were recorded by measuring marker bead displacements from over 70 filopodia on 260 Pa, 730 Pa, and 1300 Pa PAGs, the results of which are summarized here (Figure A.1). The first column indicates all recorded positions of the substrate marker bead through the course of the time-lapse. From these traces, it became clear that traction force dynamics could vary significantly from one filopodium to the next. In order to identify failure events, we normalized each marker bead trace by its maximum displacement (second column) and calculated the distribution of bead displacements from one time point to the next (third column). From these data, we found that the frequency of positive single time increments above 30% of the maximum displacement dropped off abruptly (Figure 2-10a-c), indicating the presence of infrequent failure events, and used this criterion to identify failure events in the data set (arrowheads, second column). From this analysis, we found that the frequency of failure events significantly increased with increasing substrate stiffness (Figure 2-10d).

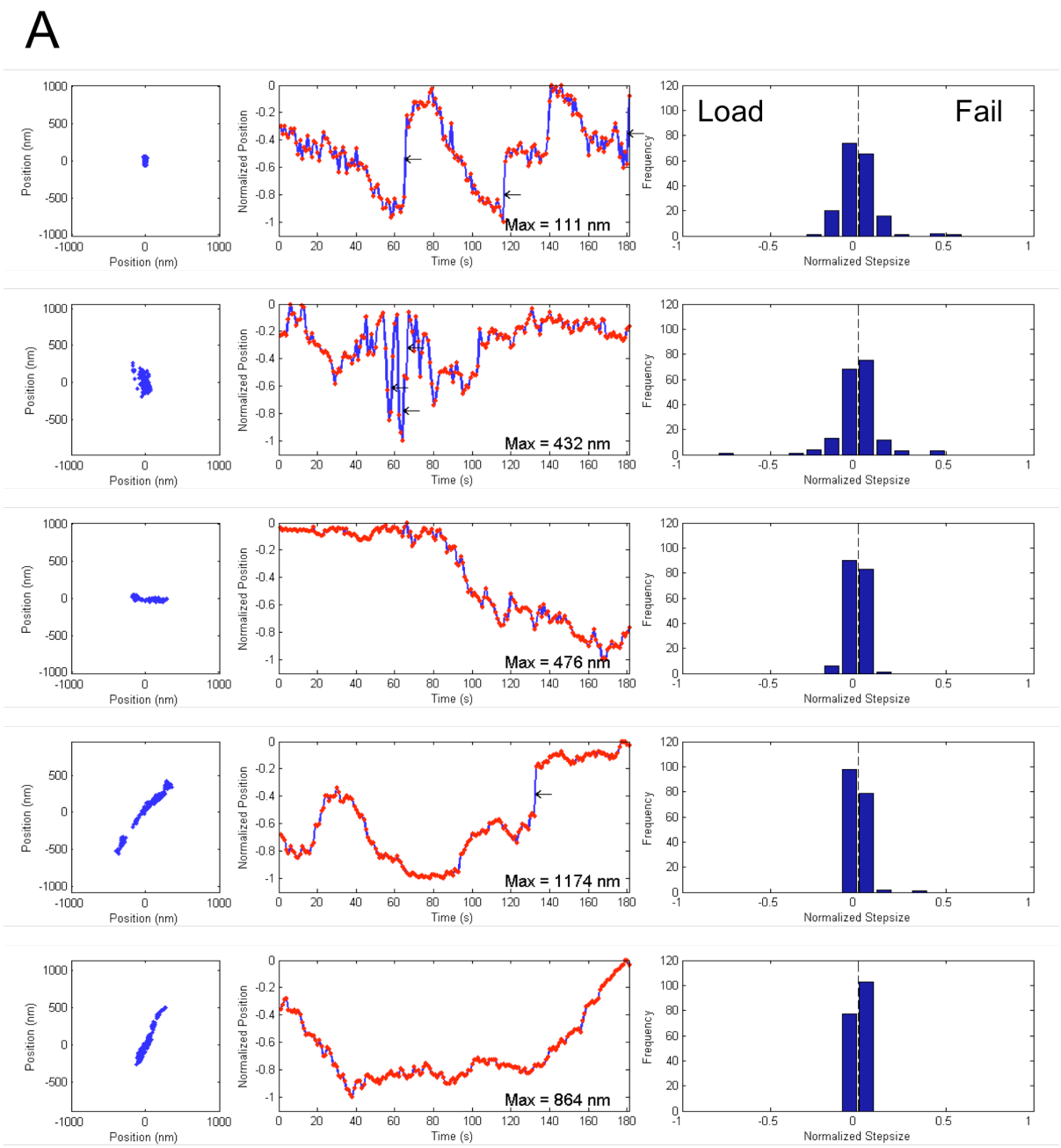

Figure A.1 Marker bead positions, trajectories and single time increment displacement distributions on (A) 260 Pa, (B) 730 Pa and (C) 1300 Pa PAGs.
First Column: Marker bead positions over the course of time-lapse recording. Second Column: Normalized marker bead position as a function of time. Arrowheads indicate coupling failures. Third Column: Histogram of single time increment sizes. Large positive increments indicate infrequent coupling failure events.

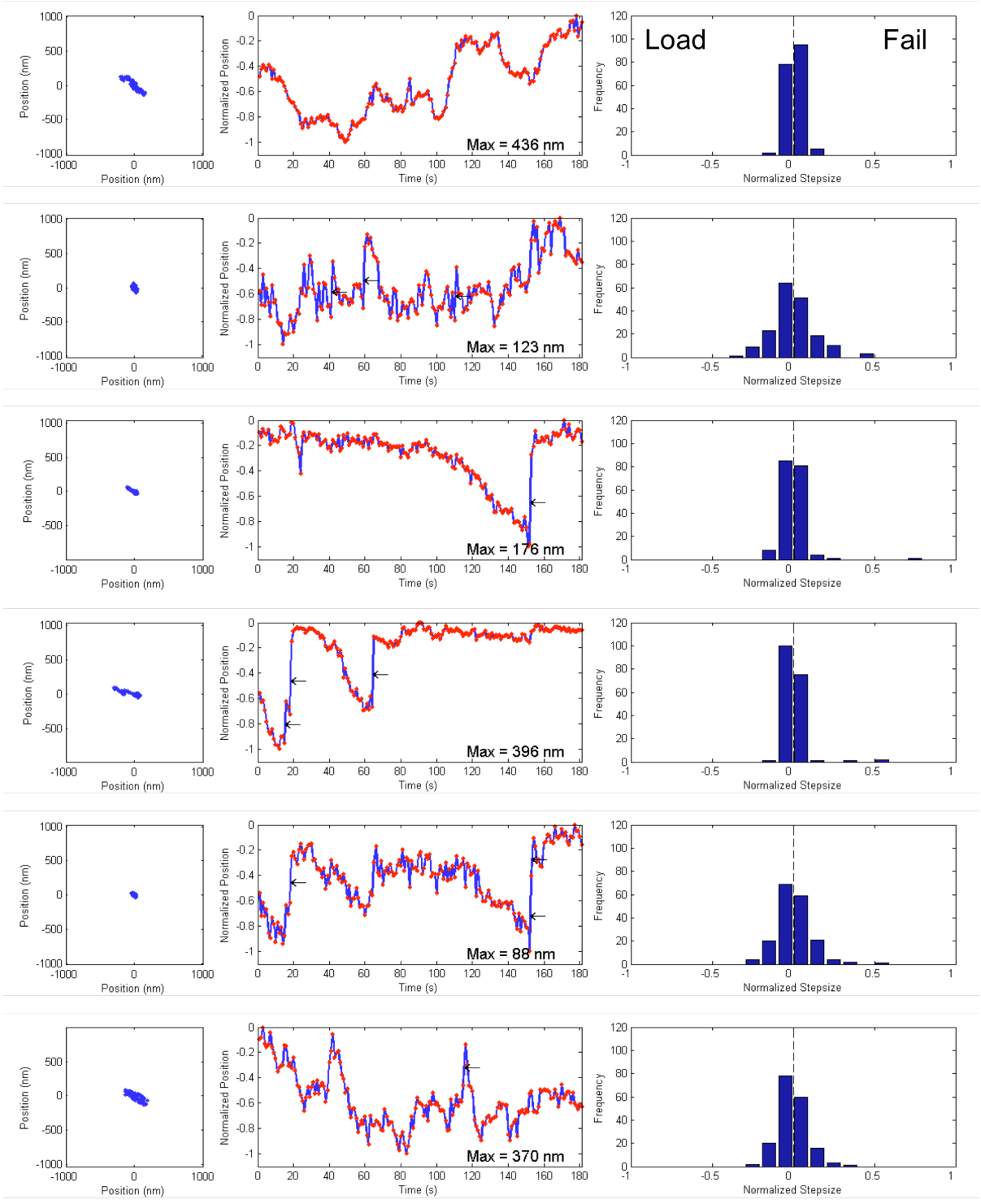
Load
Fail
Position (nm)
Normalized Position
Time (s)
Frequency
Normalized Stepsize
Max = 436 nm
Max = 123 nm
Max = 176 nm
Max = 396 nm
Max = 88 nm
Max = 370 nm

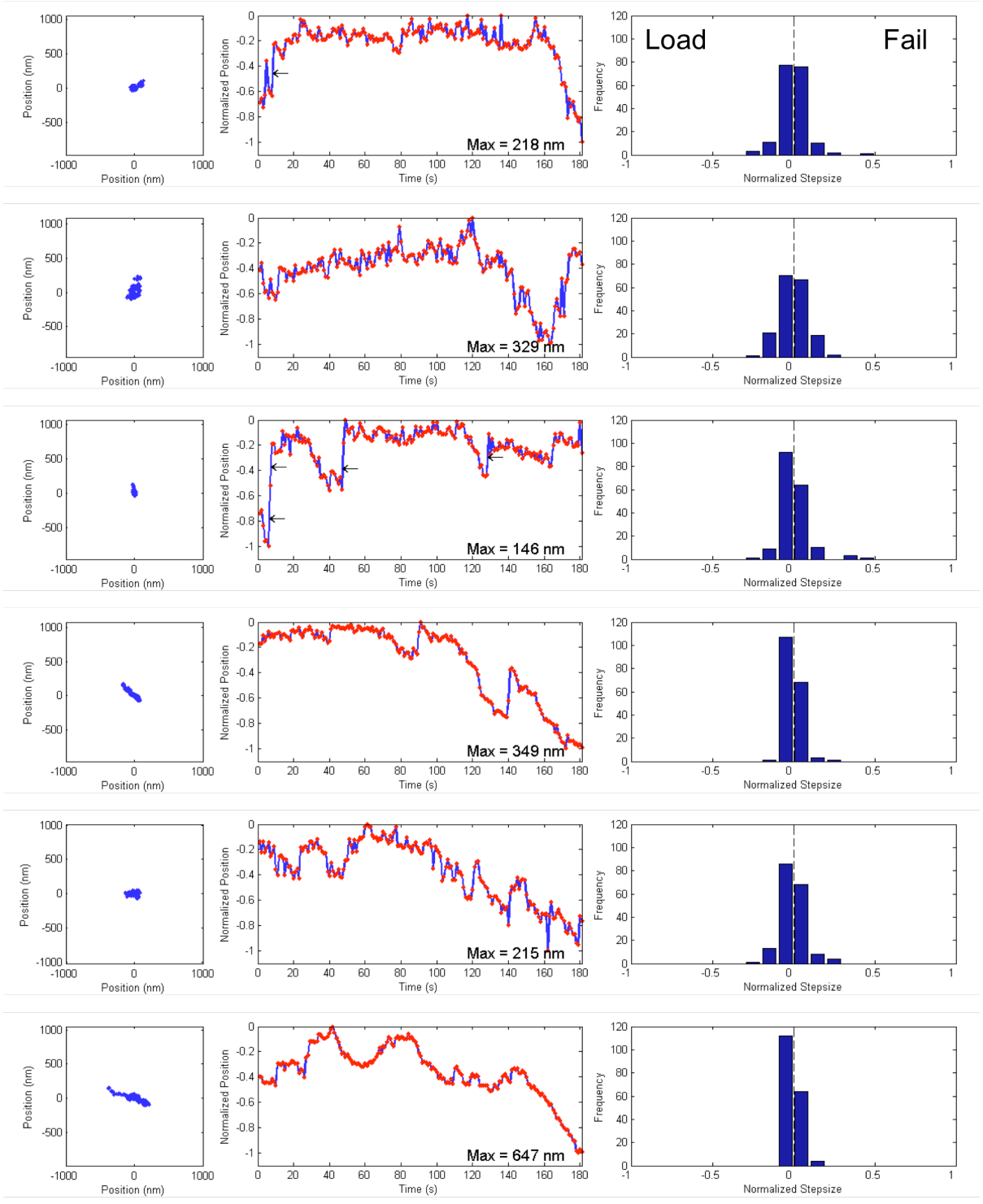
Load
Fail
Position (nm)
Normalized Position
Time (s)
Frequency
Normalized Stepsize
Max = 218 nm
Max = 329 nm
Max = 146 nm
Max = 349 nm
Max = 215 nm
Max = 647 nm

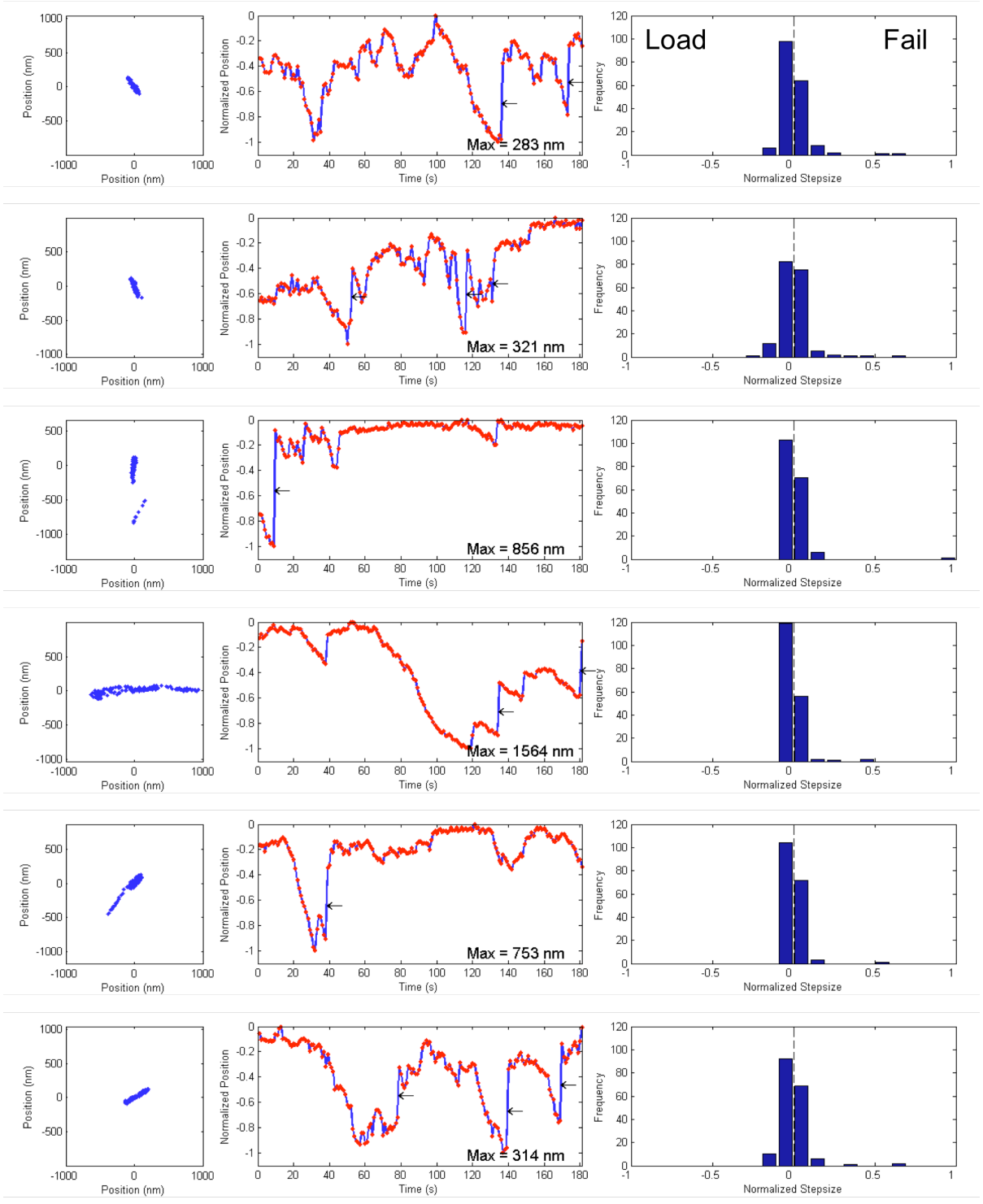
Load
Fail
Max = 283 nm
Max = 321 nm
Max = 856 nm
Max = 1564 nm
Max = 753 nm
Max = 314 nm
Position (nm)
Normalized Position
Time (s)
Frequency
Normalized Stepsize

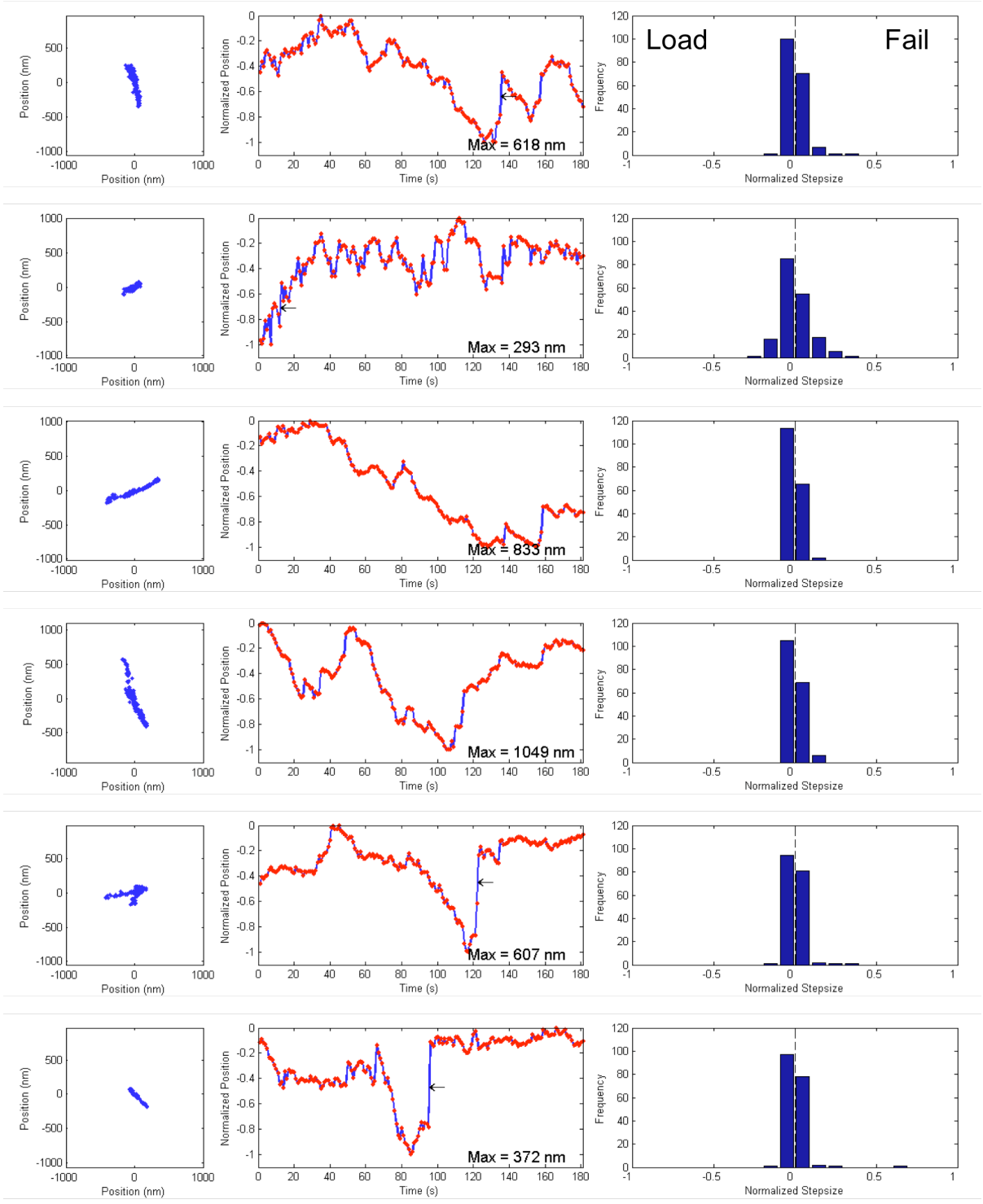
Load
Fail
Max = 618 nm
Max = 293 nm
Max = 833 nm
Max = 1049 nm
Max = 607 nm
Max = 372 nm
Position (nm)
Normalized Position
Time (s)
Frequency
Normalized Stepsize

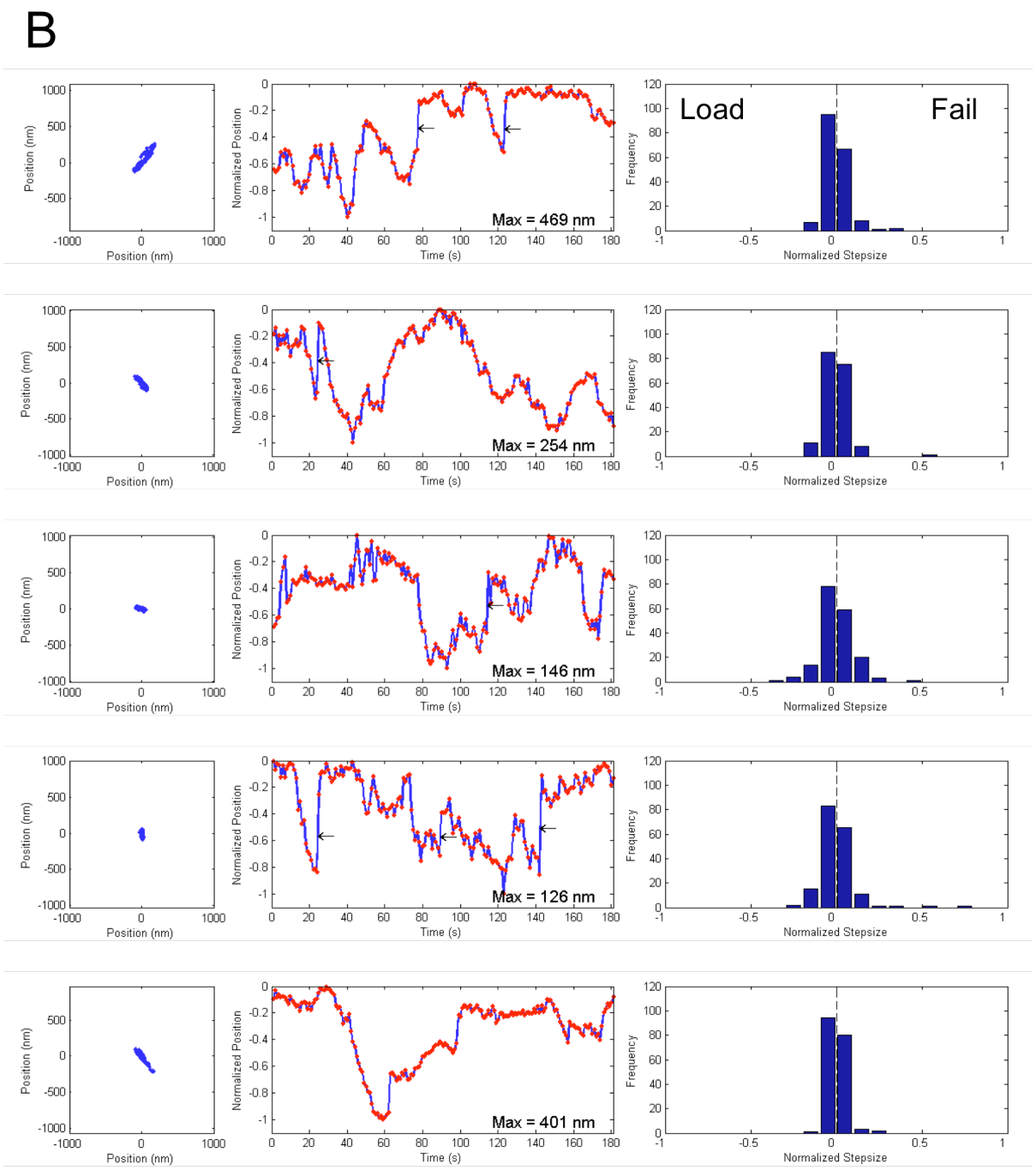

Figure A.1 Marker bead positions, trajectories and single time increment displacement distributions on (A) 260 Pa, (B) 730 Pa and (C) 1300 Pa PAGs.
First Column: Marker bead positions over the course of time-lapse recording. Second Column: Normalized marker bead position as a function of time. Arrowheads indicate coupling failures. Third Column: Histogram of single time increment sizes. Large positive increments indicate infrequent coupling failure events.

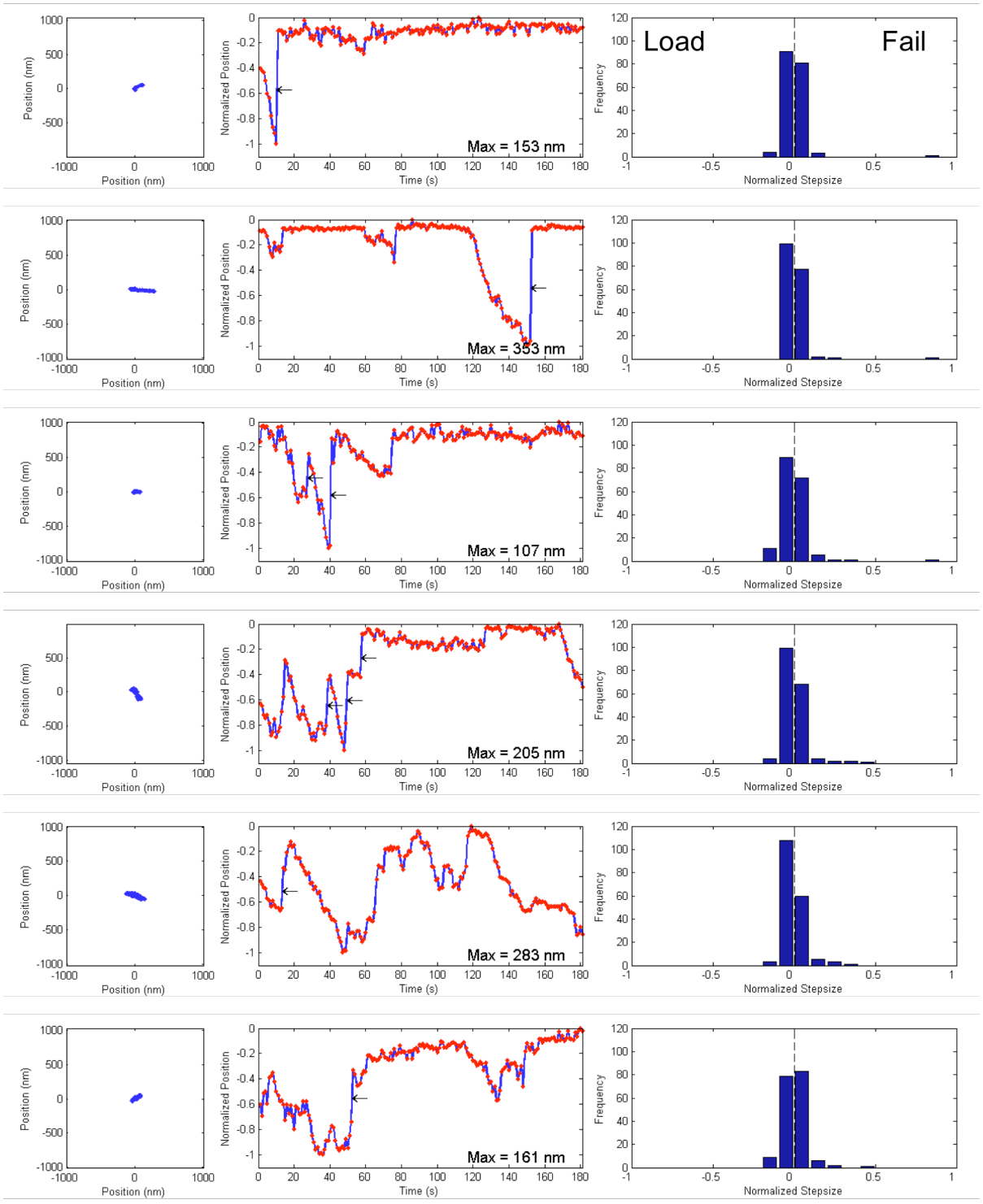
Load
Fail
Max = 153 nm
Max = 353 nm
Max = 107 nm
Max = 205 nm
Max = 283 nm
Max = 161 nm
Position (nm)
Normalized Position
Time (s)
Frequency
Normalized Stepsize

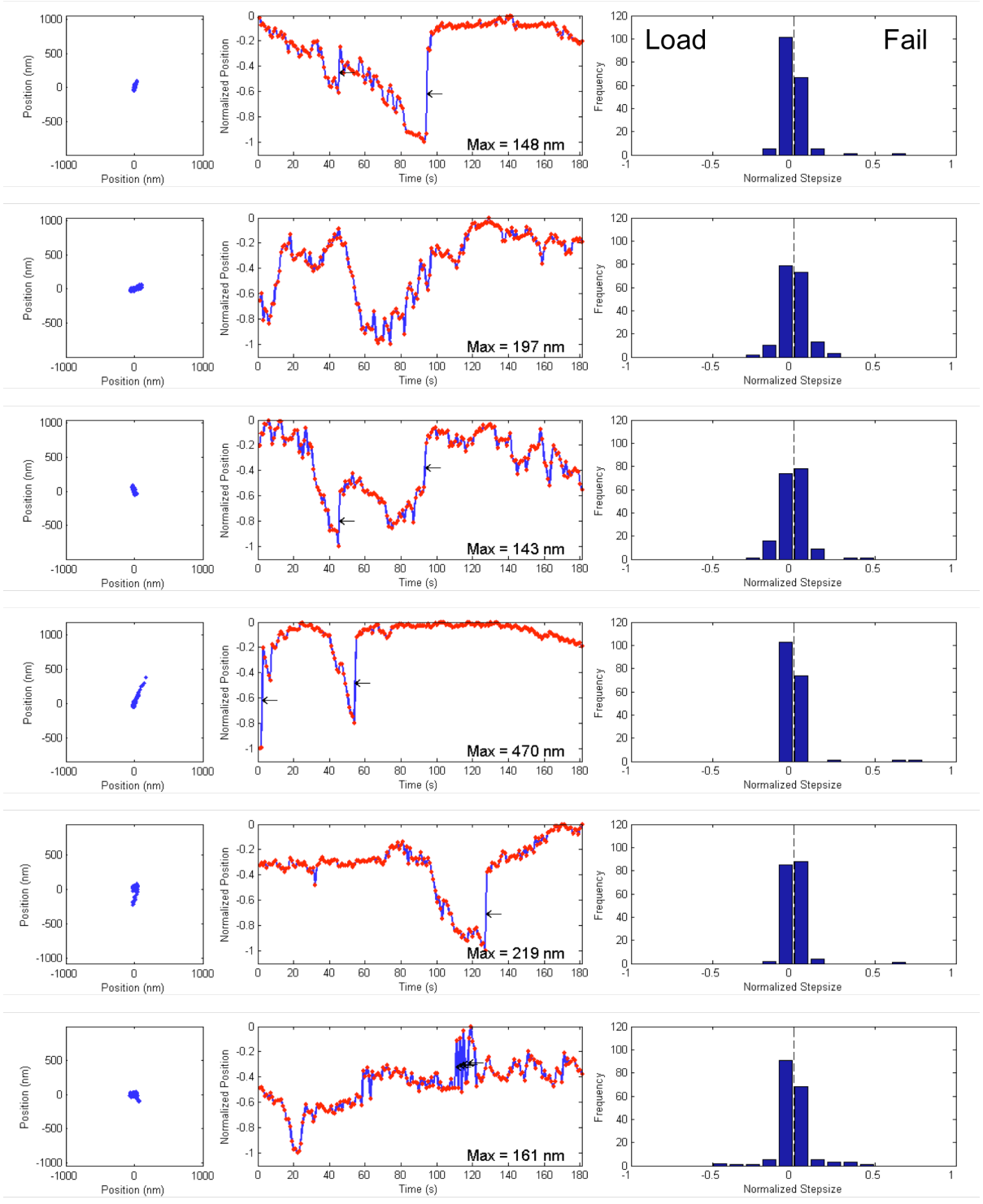
Load
Fail
Position (nm)
Normalized Position
Time (s)
Frequency
Normalized Stepsize
Max = 148 nm
Max = 197 nm
Max = 143 nm
Max = 470 nm
Max = 219 nm
Max = 161 nm

C

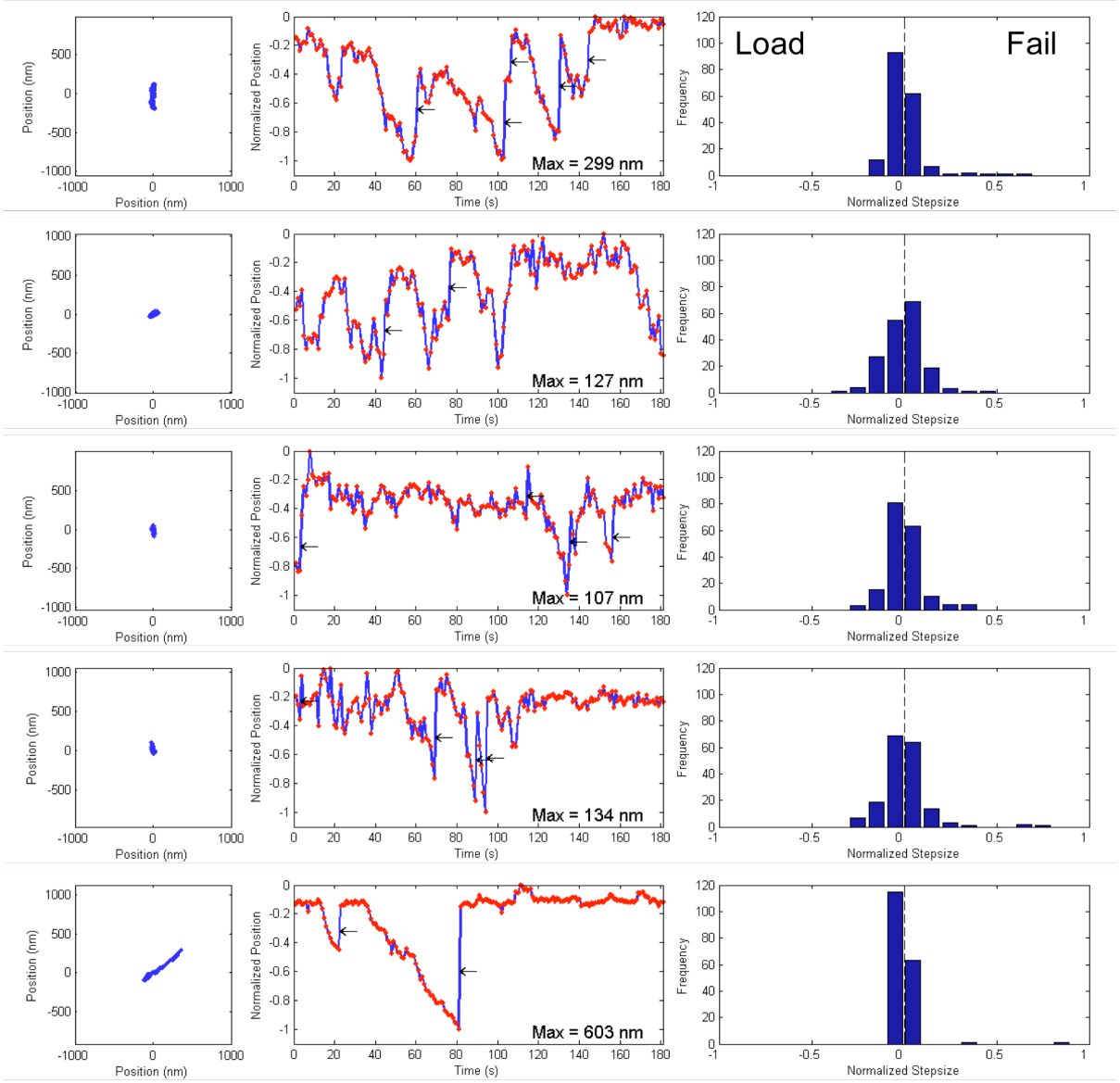

Figure A.1 Marker bead positions, trajectories and single time increment displacement distributions on (A) 260 Pa, (B) 730 Pa and (C) 1300 Pa PAGs.
First Column: Marker bead positions over the course of time-lapse recording. Second Column: Normalized marker bead position as a function of time. Arrowheads indicate coupling failures. Third Column: Histogram of single time increment sizes. Large positive increments indicate infrequent coupling failure events.

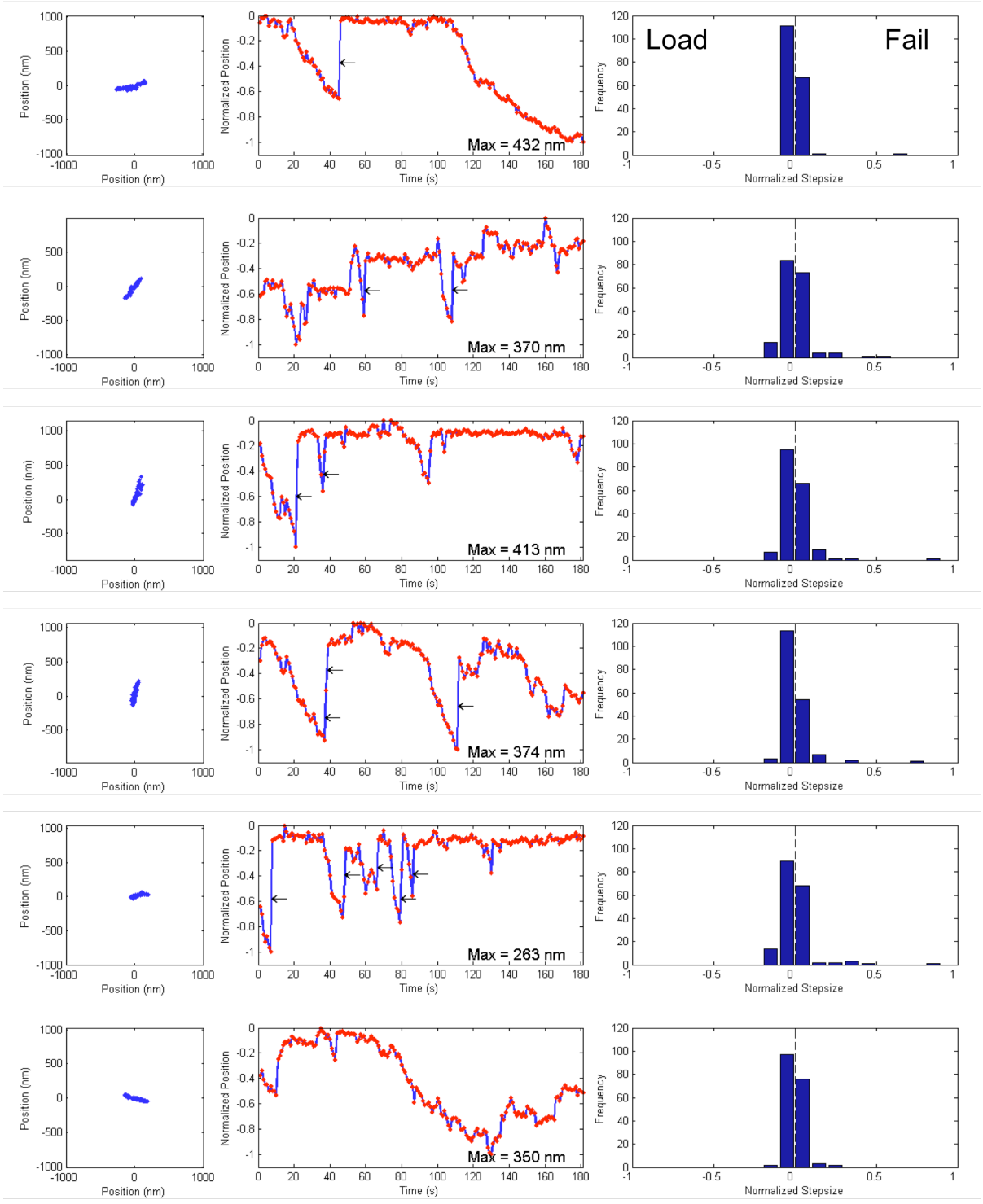
Load
Fail
Position (nm)
Normalized Position
Time (s)
Frequency
Normalized Stepsize
Max = 432 nm
Max = 370 nm
Max = 413 nm
Max = 374 nm
Max = 263 nm
Max = 350 nm

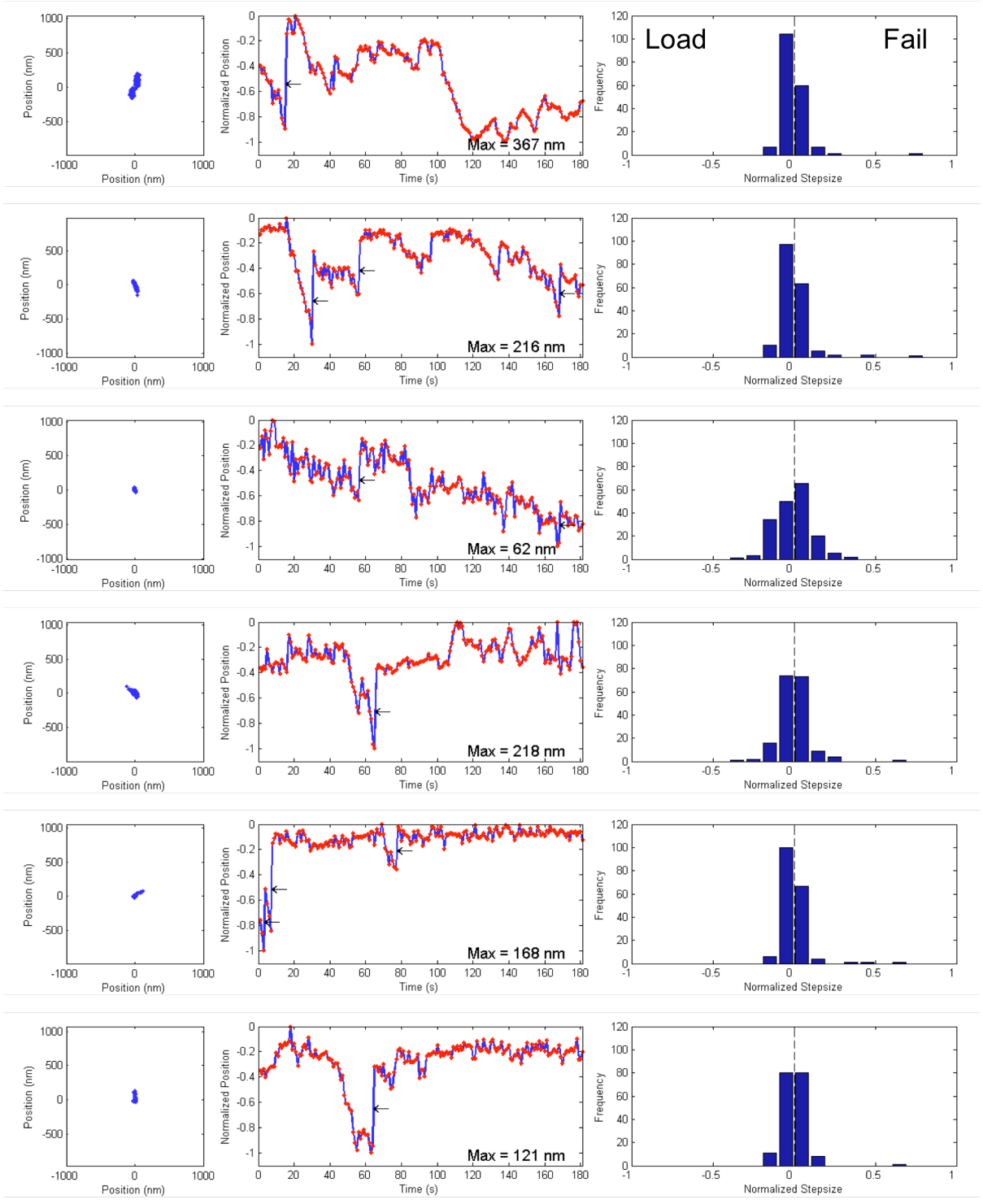
Load
Fail
Position (nm)
Normalized Position
Time (s)
Frequency
Normalized Stepsize
Max = 367 nm
Max = 216 nm
Max = 62 nm
Max = 218 nm
Max = 168 nm
Max = 121 nm

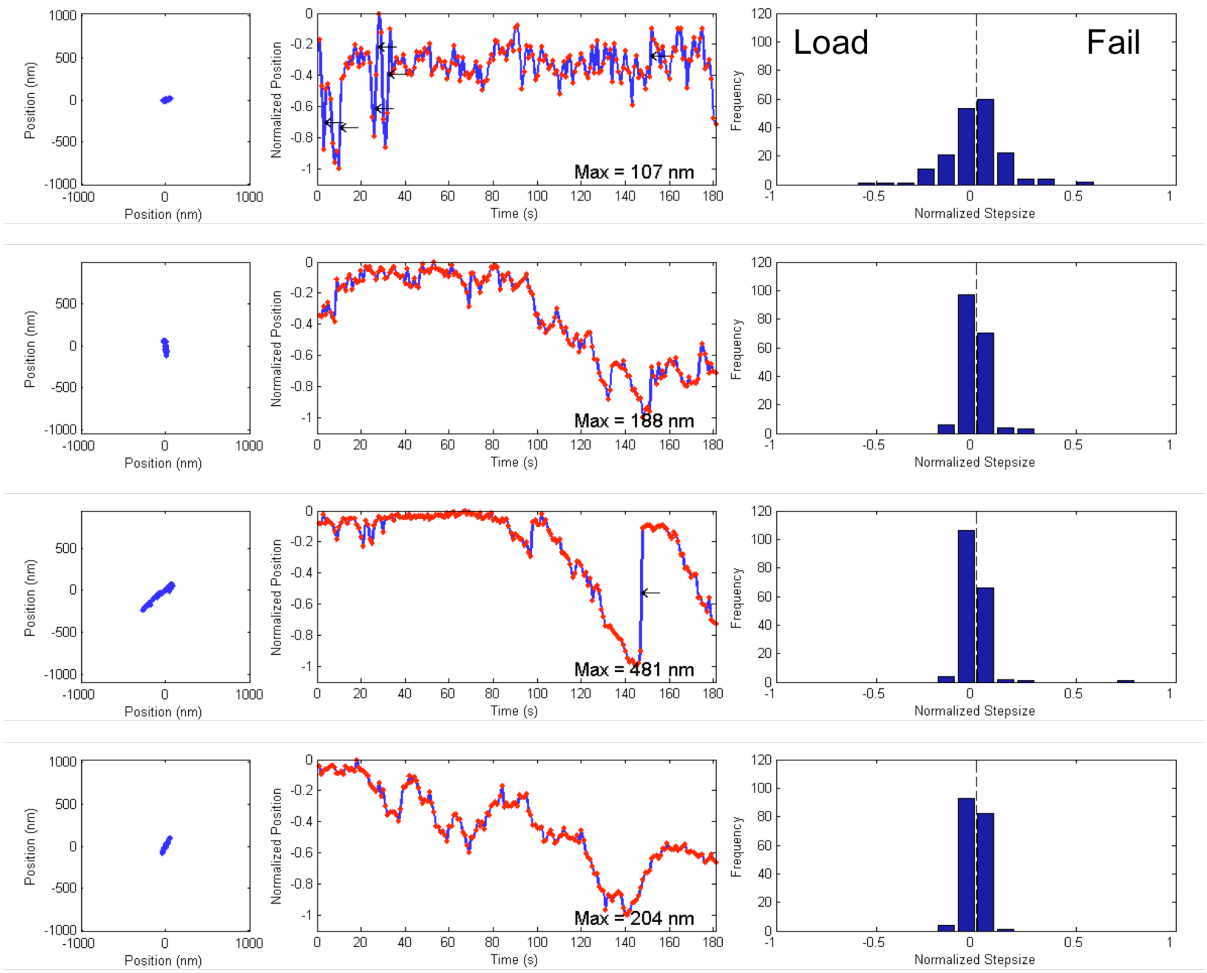
Position (nm)
Position (nm)
Normalized Position
Time (s)
Max = 107 nm
Frequency
Normalized Stepsize
Load
Fail
Max = 188 nm
Max = 481 nm
Max = 204 nm

Appendix B

EFFECTS OF SUBSTRATE STIFFNESS ON U251 GLIOMA MORPHOLOGY AND MOTILITY

(Contributing Authors: Erkan Tüzel, Clarence Chan, Kwaku Opoku, and David Odde)

Abstract

Substrate stiffness is an important physical factor in determining the cell morphology and behavior. We have investigated the morphology and motility of U251 glioma cells on collagen coated polyacrylamide gels with stiffness ranging from 0.26 to 100 kPa. Using an automated algorithm, we have tracked cells and monitored the changes in area, eccentricity and centroid position as a function of time. Our results show that on stiffer substrates, U251 glioma cells spread and elongated to a greater extent. At long times, U251 motility could be described as a simple diffusive process, with diffusion coefficients almost two orders of magnitude in the stiffness range we studied. Diffusion coefficients as high as ~6 μm^2/min have been observed. Our preliminary results also show that cell division is not affected by substrate stiffness, with all cells dividing at a rate about one division per day.

Methods

Cell Culture

U251 glioma cell cultures were maintained in a 1:1 mixture of Dublecco's modified Eagles's medium (Gibco#: 11995) and Ham's F12 media supplemented with

L-glutamine (Gibco#: 11765) and 8% fetal bovine heat inactivated serum (Gibco#: 10438). All cultures were incubated in a 5% CO_2 incubator (Forma Scientific) at 37 °C prior to and during experiments.

Preparation and Characterization of PAGs

Polyacrylamide gel (PAG) substrates were fabricated according to the procedures outlined previously (See Chapter 2, *Methods*).

To better mimic the natural environment of U251 gliomas, PAGs were covalently coated with collagen using the heterobifunctional crosslinker, sulpho-SANPAH (sulfosuccinimidyl-6-[4'-azido'-nitrophenylamino]hexanoate) (Pierce#: 22589). Briefly, PAGs was washed and covered with a thin layer of 0.5 mg/ml sulpho-SANPAH solution in 50 mM HEPES. To bind the crosslinker to the gel, the PAGs were then exposed to UV light for 8 minutes. Following this, PAGs were washed in three exchanges of 50 mM HEPES. To ensure even covered, PAGs were treated again with a thin layer of sulpho-SANPAH solution and exposed to UV for an additional 8 minutes. Next, the activated PAGs were washed in three exchanges of PBS and covered with 1 ml of 0.2 mg/ml collagen (BD Biosciences, Rat tail collagen#: 354236) in PBS. PAGs were then incubated at 4 °C with gentle rocking overnight. Prior to plating, PAGs were washed in PBS, sterilized under UV for 15 minutes, and incubated in culture media for 1 hr at 37 °C.

PAG stiffness was determined using a microsphere indentation described previously (See Chapter 2, *Methods*).

Live Cell Imaging

Images for morphological measurements were captured via phase microscopy using a 0.5 NA 20x Plan fluor objective mounted on a Nikon TE200 inverted microscope captured using a 14 bit, cooled CCD digital camera (CoolSnap HQ2, PhotoMetrics) controlled by MetaMorph software (Universal Imaging). Time-lapse recordings for motility measurements were captured on the same apparatus with a 0.3 NA 10x Plan fluor objective at 15 min time intervals over a total time of 15 hrs. Typical exposure times for recording images were 30-50 ms.

Image Analysis

In order to measure cell morphological features and track their position with time, we developed a custom cell-tracking algorithm in MATLAB. Briefly, phase images were segmented using a Sobel edge detector (*edge.m, Image Processing Toolbox*), and further processed to close, fill and filter regions of a minimize size. Following this procedure, we extract region areas, major and minor axes lengths, and centroid position. Cell eccentricity was calculated as the major axis normalized to the minor axis.

Results

Effects of substrate stiffness on U251 morphology and cell division

In order to determine what effect substrate stiffness might have on U251 morphology, we cultured U251 gliomas on collagen coated PAG substrates of stiffness ranging from 0.26-100 kPa (Figure B.1). Using our custom cell tracking tool, we found that U251 on soft PAGs remained rounded and spread to only about 500 μm^2 over the

course of 3 days. On substrates of greater stiffness, gliomas spread to a greater degree and elongated more with increasing substrate stiffness. On the stiffest substrate, cells spread and elongated almost 2-3x greater than on the softest substrate, a trend that was maintained over the course of 3 days.

Next, we investigated the effects of substrate stiffness on U251 cell division by recording 10-15 random fields in each stiffness condition, and measured cell numbers over time. Normalizing the results to the first day, we found the cell division was not significantly different over the range of stiffness (Figure B.2). These results suggest that U251 gliomas divide at a rate of about 1 division per day regardless of the stiffness of the local environment.

Effects of substrate stiffness on U251 motility

Many cells exhibit a behavior known as durotaxis, preferentially migrating towards regions of higher stiffness. To determine how U251 glioma motility is affected by substrate stiffness, we imaged cultures over our stiffness range, each for over 15 hrs. Using our tracking algorithm, we found a striking difference in the range U251 gliomas explored as a function of substrate stiffness (Figure B.3). While most gliomas on 260 Pa PAGs hardly moved, gliomas on 100 kPa PAGs explored regions within 200 μm of their beginning position. Calculating their displacement over time, we found that gliomas crawled faster over stiffness substrates (Figure B.4). When modeled as a diffusive processes, we found that their diffusion coefficients spanned almost 3 orders of magnitude (Figure B.5).

Summary

Together these results show to U251 human gliomas sense and respond to substrate stiffness. On stiffer substrates, gliomas spread further and elongate to a greater degree. In addition, gliomas become more motile on stiffer substrates, exploring larger areas and crawling faster as the substrate stiffness increased. Future work will focus on what focal adhesions contribute to this behavior and whether myosin motors provide the driving force for motility. By further understanding the fundamentals of this process, it is hope that therapies for this aggressive cancer can be developed.

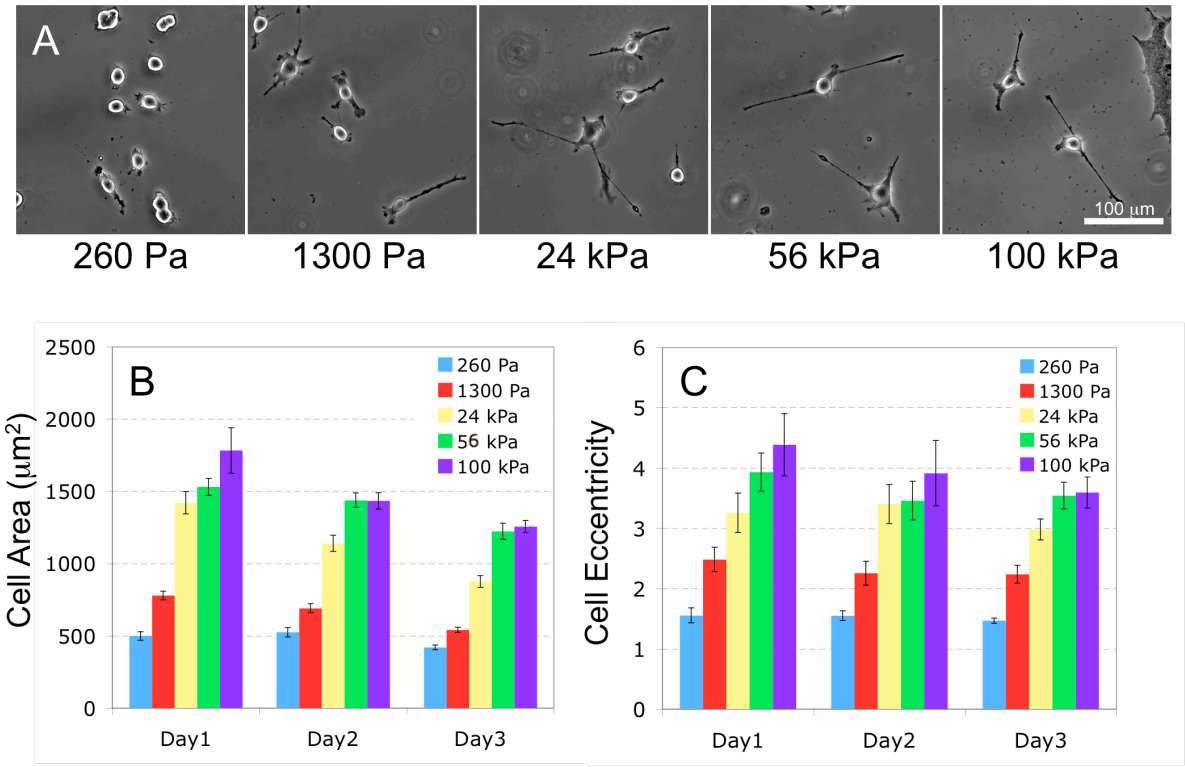

Figure B.1 U251 glioma area and shape are altered by substrate stiffness.
(A) Representative images of U251 glioma cells on PAG substrates with stiffness values in the range 0.26-100 kPa. (B) Cell area as a function of stiffness and time. (C) Cell eccentricity as a function of stiffness and time.

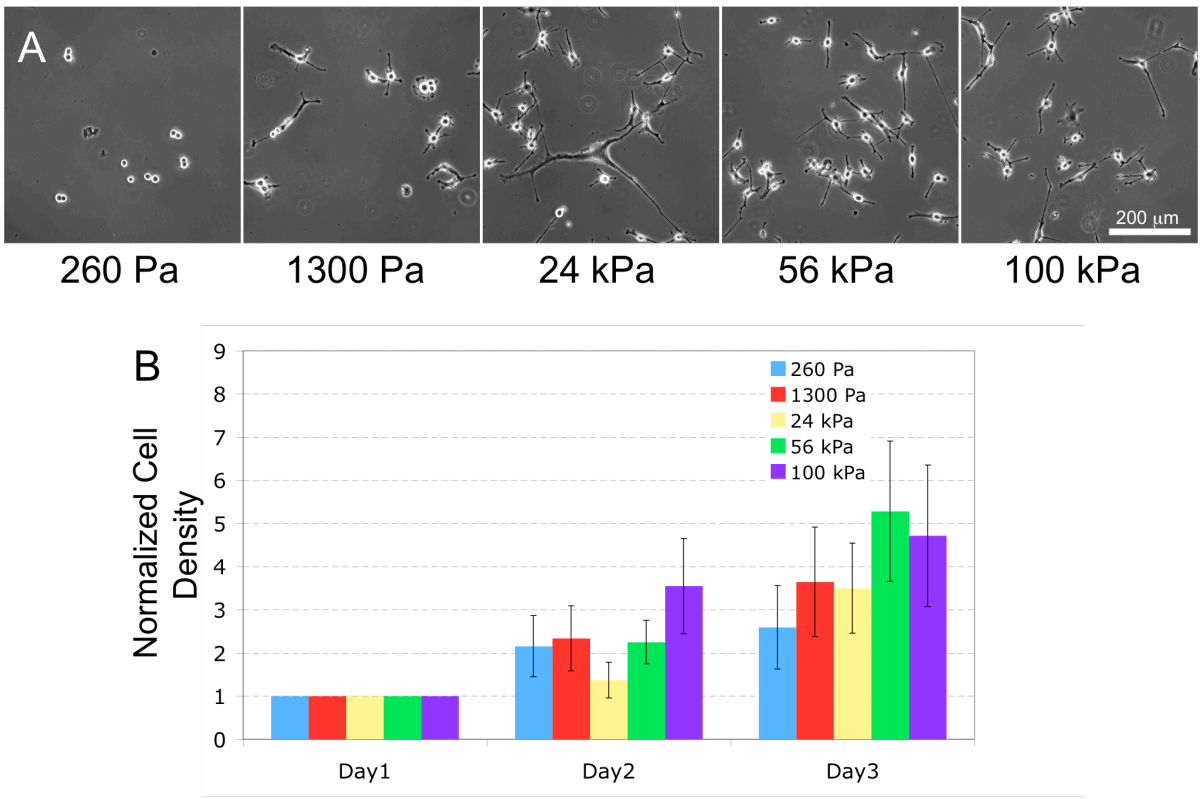

Figure B.2 U251 glioma expansion times are not significantly altered by substrate stiffness. (A) Representative images of U251 glioma cell density on PAG substrates with stiffness values in the range 0.26-100 kPa. (B) Normalized cell densities as a function of time.

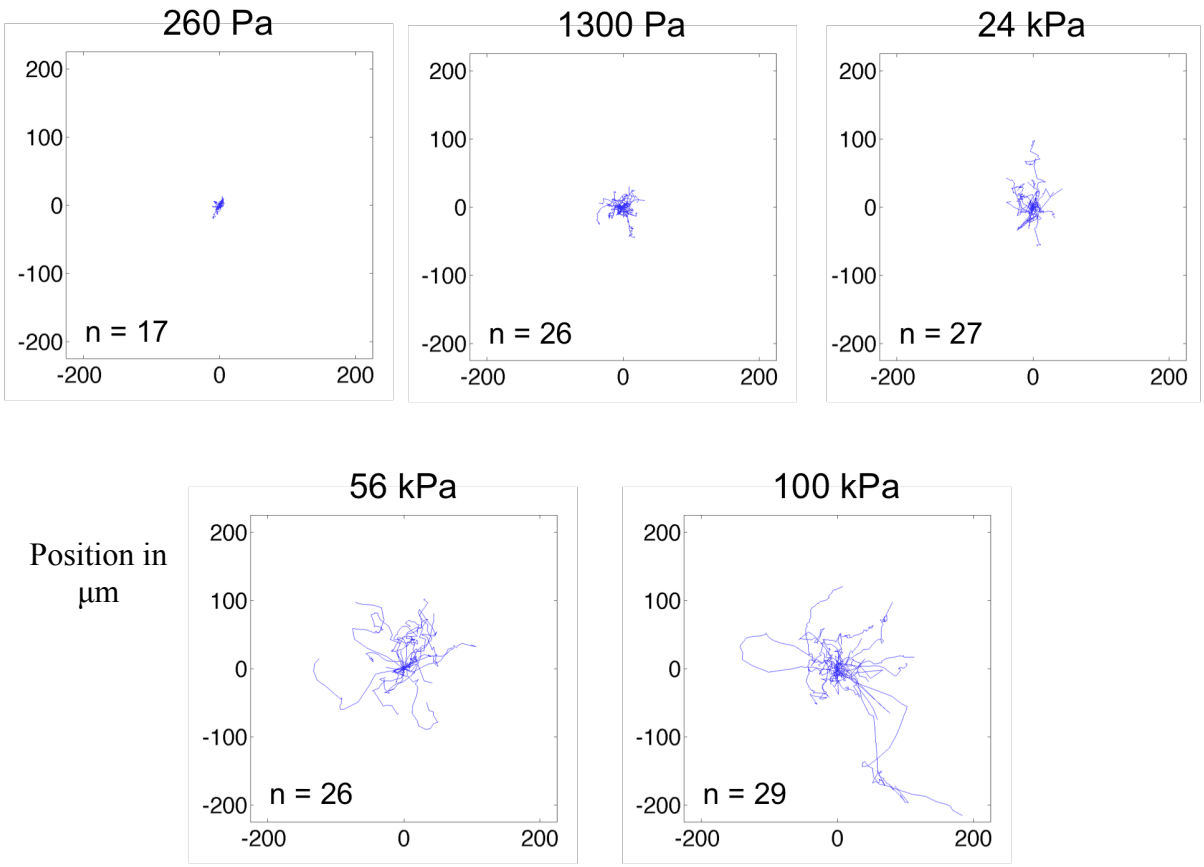

Figure B.3 U251 gliomas explore a larger surface area as PAG substrate stiffness increases. Traces of the paths of different cells shifted to the same origin are shown for stiffness values in the range 0.26-100 kPa.

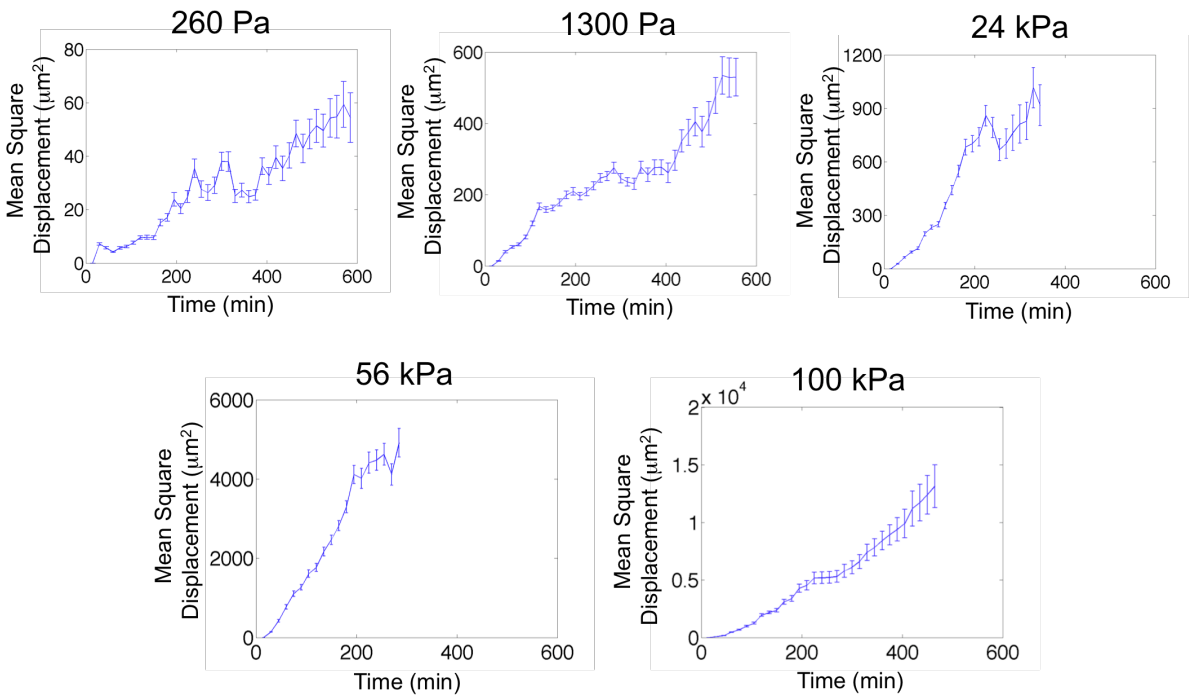

Figure B.4 U251 glioma cells move faster as substrate stiffness increases.
Mean square displacement of U251 glioma cells as a function of time for PAG substrates with stiffness values in the range 0.26-100 kPa.

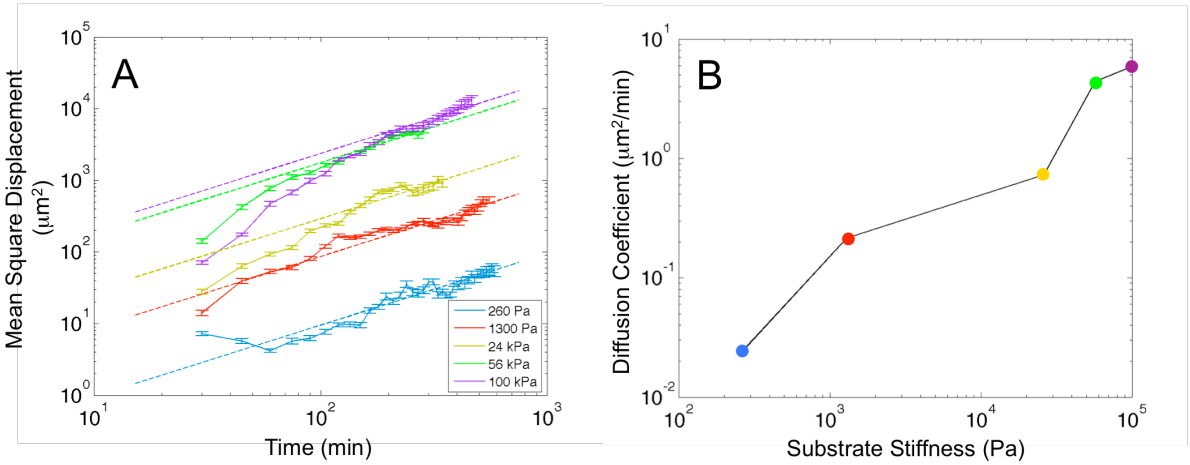

Figure B.5 U251 glioma cells "diffuse" faster over stiffer PAG substrates.
(A) Average mean square displacement of cells as a function of time for stiffness values in the range 0.26-100 kPa. (B) Diffusion coefficients obtained from the linear fits in (A) as a function of substrate stiffness.

REFERENCES

1. Small, J.V., *The actin cytoskeleton.* Electron Microsc Rev, 1988. **1**(1): p. 155-74.

2. Pollard, T.D. and G.G. Borisy, *Cellular motility driven by assembly and disassembly of actin filaments.* Cell, 2003. **112**(4): p. 453-65.

3. Gundersen, R.W. and J.N. Barrett, *Characterization of the turning response of dorsal root neurites toward nerve growth factor.* J Cell Biol, 1980. **87**(3 Pt 1): p. 546-54.

4. Zheng, J.Q., J.J. Wan, and M.M. Poo, *Essential role of filopodia in chemotropic turning of nerve growth cone induced by a glutamate gradient.* J Neurosci, 1996. **16**(3): p. 1140-9.

5. Mallavarapu, A. and T. Mitchison, *Regulated actin cytoskeleton assembly at filopodium tips controls their extension and retraction.* J Cell Biol, 1999. **146**(5): p. 1097-106.

6. Strasser, G.A., et al., *Arp2/3 is a negative regulator of growth cone translocation.* Neuron, 2004. **43**(1): p. 81-94.

7. Borisy, G.G. and T.M. Svitkina, *Actin machinery: pushing the envelope.* Curr Opin Cell Biol, 2000. **12**(1): p. 104-12.

8. Wang, Y.L., *Exchange of actin subunits at the leading edge of living fibroblasts: possible role of treadmilling.* J Cell Biol, 1985. **101**(2): p. 597-602.

9. Pasternak, C., J.A. Spudich, and E.L. Elson, *Capping of surface receptors and concomitant cortical tension are generated by conventional myosin.* Nature, 1989. **341**(6242): p. 549-51.

10. Critchley, D.R., *Focal adhesions - the cytoskeletal connection.* Current Opinion in Cell Biology, 2000. **12**(1): p. 133-139.

11. van der Flier, A. and A. Sonnenberg, *Function and interactions of integrins.* Cell Tissue Res, 2001. **305**(3): p. 285-98.

12. Abercrombie, M., J.E. Heaysman, and S.M. Pegrum, *The locomotion of fibroblasts in culture. IV. Electron microscopy of the leading lamella.* Exp Cell Res, 1971. **67**(2): p. 359-67.

13. Critchley, D.R., *Focal adhesions - the cytoskeletal connection.* Curr Opin Cell Biol, 2000. **12**(1): p. 133-9.

14. Carragher, N.O. and M.C. Frame, *Focal adhesion and actin dynamics: a place where kinases and proteases meet to promote invasion.* Trends Cell Biol, 2004. **14**(5): p. 241-9.

15. Mitchison, T. and M. Kirschner, *Cytoskeletal dynamics and nerve growth.* Neuron, 1988. **1**(9): p. 761-72.

16. Brummendorf, T. and F.G. Rathjen, *Cell adhesion molecules 1: immunoglobulin superfamily.* Protein Profile, 1995. **2**(9): p. 963-1108.

17. Brummendorf, T. and F.G. Rathjen, *Structure/function relationships of axon-associated adhesion receptors of the immunoglobulin superfamily.* Curr Opin Neurobiol, 1996. **6**(5): p. 584-93.

18. Thompson, C., C.H. Lin, and P. Forscher, *An Aplysia cell adhesion molecule associated with site-directed actin filament assembly in neuronal growth cones.* J Cell Sci, 1996. **109 (Pt 12)**: p. 2843-54.

19. Suter, D.M., et al., *The Ig superfamily cell adhesion molecule, apCAM, mediates growth cone steering by substrate-cytoskeletal coupling.* J Cell Biol, 1998. **141**(1): p. 227-40.

20. Scholey, J., I. Brust-Mascher, and A. Mogilner, *Cell division.* Nature, 2003. **422**(6933): p. 746-752.

21. Thompson, S. and D. Compton, *Examining the link between chromosomal instability and aneuploidy in human cells.* The Journal of Cell Biology, 2008. **180**(4): p. 665.

22. Compton, D., *Spindle assembly in animal cells.* Annu Rev Biochem, 2000. **69**: p. 95-114.

23. Tanaka, T.U. and A. Desai, *Kinetochore-microtubule interactions: the means to the end.* Current Opinion in Cell Biology, 2008. **20**(1): p. 53-63.

24. Maiato, H., et al., *The dynamic kinetochore-microtubule interface*. 2004, © The Company of Biologists Limited 2004. p. 5461-5477.

25. Gardner, M., et al., *Tension-dependent Regulation of Microtubule Dynamics at Kinetochores Can Explain Metaphase Congression in Yeast.* Molecular Biology of the Cell, 2005. **16**(8): p. 3764-3775.

26. Ciferri, C., A. Musacchio, and A. Petrovic, *The Ndc80 complex: Hub of kinetochore activity.* FEBS Letters, 2007. **581**(15): p. 2862-2869.

27. Wei, R.R., J. Al-Bassam, and S.C. Harrison, *The Ndc80/HEC1 complex is a contact point for kinetochore-microtubule attachment.* Nat Struct Mol Biol, 2007. **14**(1): p. 54-59.

28. Wei, R., P. Sorger, and S. Harrison, *Molecular organization of the Ndc80 complex, an essential kinetochore component.* Proceedings of the National Academy of Sciences, 2005. **102**(15): p. 5363-5367.

29. Wang, H.-W., et al., *Architecture and Flexibility of the Yeast Ndc80 Kinetochore Complex.* Journal of Molecular Biology, 2008. **383**(4): p. 894-903.

30. Pinsky, B., et al., *The Ipl1-Aurora protein kinase activates the spindle checkpoint by creating unattached kinetochores.* Nature Cell Biology, 2005. **8**: p. 78-83.

31. DeLuca, J., et al., *Hec1 and Nuf2 Are Core Components of the Kinetochore Outer Plate Essential for Organizing Microtubule Attachment Sites.* Molecular Biology of the Cell, 2005. **16**(2): p. 519-531.

32. Hori, T., et al., *Dynamic behavior of Nuf2-Hec1 complex that localizes to the centrosome and centromere and is essential for mitotic progression in vertebrate cells.* Journal of Cell Science, 2003. **116**(16): p. 3347-3362.

33. Dong, Y., et al., *The outer plate in vertebrate kinetochores is a flexible network with multiple microtubule interactions.* Nature Cell Biology, 2007. **9**(5): p. 516.

34. Wilson-Kubalek, E.M., et al., *Orientation and structure of the Ndc80 complex on the microtubule lattice.* J. Cell Biol., 2008: p. jcb.200804170-jcb.200804170.

35. Westermann, S., et al., *Formation of a Dynamic Kinetochore-Microtubule Interface through Assembly of the Dam1 Ring Complex.* Molecular Cell, 2005. **17**(2): p. 277-290.

36. Tanaka, K., et al., *Molecular mechanisms of kinetochore capture by spindle microtubules.* Nature, 2005. **434**: p. 987-994.

37. Cheeseman, I., et al., *Mitotic Spindle Integrity and Kinetochore Function Linked by the Duo1p/Dam1p Complex.* The Journal of Cell Biology, 2001. **152**(1): p. 197-212.

38. Asbury, C., et al., *The Dam1 kinetochore complex harnesses microtubule dynamics to produce force and movement.* Proceedings of the National Academy of Sciences, 2006. **103**(26): p. 9873.

39. Westermann, S., et al., *The Dam1 kinetochore ring complex moves processively on depolymerizing microtubule ends.* 2006.

40. Franck, A., et al., *Tension applied through the Dam1 complex promotes microtubule elongation providing a direct mechanism for length control in mitosis.* Nature Cell Biology, 2007. **9**(7): p. 832.

41. Molodtsov, M.I., et al., *Force production by depolymerizing microtubules: a theoretical study.* Proceedings of the National Academy of Sciences of the United States of America, 2005. **102**(12): p. 4353-8.

42. Efremov, A., et al., *In search of an optimal ring to couple microtubule depolymerization to processive chromosome motions.* Proceedings of the National Academy of Sciences of the United States of America, 2007. **104**(48): p. 19017-22.

43. Liu, J. and J.N. Onuchic, *A driving and coupling "Pac-Man" mechanism for chromosome poleward translocation in anaphase A.* Proceedings of the National Academy of Sciences of the United States of America, 2006. **103**(49): p. 18432-7.

44. Gestaut, D.R., et al., *Phosphoregulation and depolymerization-driven movement of the Dam1 complex do not require ring formation.* Nat Cell Biol, 2008. **10**(4): p. 407-414.

45. Hill, T., *Theoretical Problems Related to the Attachment of Microtubules to Kinetochores.* Proceedings of the National Academy of Sciences, 1985. **82**(13): p. 4404-4408.

46. Joglekar, A. and A. Hunt, *A Simple, Mechanistic Model for Directional Instability during Mitotic Chromosome Movements.* Biophysical Journal, 2002. **83**(1): p. 42-58.

47. O'Toole, E.T., et al., *Morphologically distinct microtubule ends in the mitotic centrosome of Caenorhabditis elegans.* J. Cell Biol., 2003. **163**(3): p. 451-456.

48. Yeung, T., et al., *Effects of substrate stiffness on cell morphology, cytoskeletal structure, and adhesion.* Cell Motility and the Cytoskeleton, 2005. **60**: p. 24-34.

49. Lo, C.-M., et al., *Cell Movement Is Guided by the Rigidity of the Substrate.* Biophys. J., 2000. **79**(1): p. 144-152.

50. Flanagan, L.A., et al., *Neurite branching on deformable substrates.* Neuroreport, 2002. **13**(18): p. 2411-5.

51. Georges, P.C., et al., *Matrices with Compliance Comparable to that of Brain Tissue Select Neuronal over Glial Growth in Mixed Cortical Cultures.* Biophys. J., 2006. **90**(8): p. 3012-3018.

52. Engler, A.J., et al., *Matrix Elasticity Directs Stem Cell Lineage Specification.* Cell, 2006. **126**(4): p. 677-689.

53. Hu, K., et al., *Differential Transmission of Actin Motion Within Focal Adhesions.* Science, 2007. **315**(5808): p. 111-115.

54. Jurado, C., J.R. Haserick, and J. Lee, *Slipping or Gripping? Fluorescent Speckle Microscopy in Fish Keratocytes Reveals Two Different Mechanisms for Generating a Retrograde Flow of Actin.* Mol. Biol. Cell, 2005. **16**(2): p. 507-518.

55. Smilenov, L.B., et al., *Focal Adhesion Motility Revealed in Stationary Fibroblasts.* Science, 1999. **286**(5442): p. 1172-1174.

56. Zamir, E. and B. Geiger, *Molecular complexity and dynamics of cell-matrix adhesions.* J Cell Sci, 2001. **114**(20): p. 3583-3590.

57. Brown, M.E. and P.C. Bridgman, *Retrograde flow rate is increased in growth cones from myosin IIB knockout mice.* J Cell Sci, 2003. **116**(6): p. 1087-1094.

58. Bell, G.I., *Models for the specific adhesion of cells to cells.* Science, 1978. **200**(4342): p. 618-627.

59. Nakamura, H. and J.-i. Funahashi, *Introduction of DNA into Chick Embryos by in Ovo Electroporation.* Methods, 2001. **24**(1): p. 43-48.

60. Fass, J.N. and D.J. Odde, *Tensile Force-Dependent Neurite Elicitation via Anti-?1 Integrin Antibody-Coated Magnetic Beads.* Biophys. J., 2003. **85**(1): p. 623-636.

61. Wang, Y.L. and R.J. Pelham, *Preparation of a flexible, porous polyacrylamide substrate for mechanical studies of cultured cells.* Methods in enzymology, 1998. **298**: p. 489-96.

62. Kandow, C.E., et al., *Polyacrylamide Hydrogels for Cell Mechanics: Steps Toward Optimization and Alternative Uses*, in *Cell Mechanics*. 2007, Academic Press. p. 29-46.

63. Hertz, H., *Uber die Beruhrung fester elastischer Korper.* J. Reine Angew. Mathematik. [in German], 1882. **92**: p. 156?171-156?171.

64. Ding, H., *Elasticity of Transversely Isotropic Materials*. 2006: Springer. 435.

65. Ji, L. and G. Danuser, *Tracking Quasi-Stationary Flow of Weak Fluorescent Signals by Adaptive Multi-Frame Correlation.* Journal of Microscopy, 2005. **220**(3): p. 150-167.

66. Sprague, B.L., et al., *Mechanisms of Microtubule-Based Kinetochore Positioning in the Yeast Metaphase Spindle.* Biophys. J., 2003. **84**(6): p. 3529-3546.

67. Gardner, M.K., et al., *Tension-dependent Regulation of Microtubule Dynamics at Kinetochores Can Explain Metaphase Congression in Yeast.* Mol. Biol. Cell, 2005. **16**(8): p. 3764-3775.

68. Gardner, M.K., D.J. Odde, and K. Bloom, *Hypothesis testing via integrated computer modeling and digital fluorescence microscopy.* Methods, 2007. **41**(2): p. 232-237.

69. Pearson, C.G., et al., *Measuring Nanometer Scale Gradients in Spindle Microtubule Dynamics Using Model Convolution Microscopy.* Mol. Biol. Cell, 2006. **17**(9): p. 4069-4079.

70. Bicek, A.D., et al., *Analysis of microtubule curvature.* Methods in Cell Biology, 2007. **83**: p. 237-68.

71. Balaban, N.Q., et al., *Force and focal adhesion assembly: a close relationship studied using elastic micropatterned substrates.* Nat Cell Biol, 2001. **3**(5): p. 466-472.

72. Riveline, D., et al., *Focal Contacts as Mechanosensors: Externally Applied Local Mechanical Force Induces Growth of Focal Contacts by an mDia1-dependent and ROCK-independent Mechanism.* J. Cell Biol., 2001. **153**(6): p. 1175-1186.

73. Mallavarapu, A. and T. Mitchison, *Regulated Actin Cytoskeleton Assembly at Filopodium Tips Controls Their Extension and Retraction.* J. Cell Biol., 1999. **146**(5): p. 1097-1106.

74. Gupton, S.L. and C.M. Waterman-Storer, *Spatiotemporal Feedback between Actomyosin and Focal-Adhesion Systems Optimizes Rapid Cell Migration.* Cell, 2006. **125**(7): p. 1361-1374.

75. Howard, J. and R.L. Clark, *Mechanics of Motor Proteins and the Cytoskeleton.* Applied Mechanics Reviews, 2002. **55**(2): p. B39-B39.

76. Pelham, R.J. and Y.-l. Wang, *Cell locomotion and focal adhesions are regulated by substrate flexibility.* Proceedings of the National Academy of Sciences, 1997. **94**(25): p. 13661-13665.

77. Denda, S. and L.F. Reichardt, *Studies on Integrins in the Nervous System.* Methods in enzymology, 2007. **426**: p. 203-221.

78. Gil, O.D., et al., *Ankyrin Binding Mediates L1CAM Interactions with Static Components of the Cytoskeleton and Inhibits Retrograde Movement of L1CAM on the Cell Surface.* The Journal of Cell Biology, 2003. **162**(4): p. 719-730.

79. Gomez, T.M., F.K. Roche, and P.C. Letourneau, *Chick sensory neuronal growth cones distinguish fibronectin from laminin by making substratum contacts that resemble focal contacts.* Journal of Neurobiology, 1996. **29**(1): p. 18-34.

80. Lin, C.H. and P. Forscher, *Growth cone advance is inversely proportional to retrograde F-actin flow.* Neuron, 1995. **14**(4): p. 763-71.

81. Nishimura, K., et al., *L1-Dependent Neuritogenesis Involves Ankyrin B That Mediates L1-CAM Coupling with Retrograde Actin Flow.* The Journal of Cell Biology, 2003. **163**(5): p. 1077-1088.

82. Renaudin, A., et al., *Organization of point contacts in neuronal growth cones.* Journal of Neuroscience Research, 1999. **55**(4): p. 458-471.

83. Suter, D.M. and P. Forscher, *Substrate-cytoskeletal coupling as a mechanism for the regulation of growth cone motility and guidance.* Journal of Neurobiology, 2000. **44**(2): p. 97-113.

84. Pellegrin, S. and H. Mellor, *The Rho Family GTPase Rif Induces Filopodia through mDia2.* Current Biology, 2005. **15**(2): p. 129-133.

85. Sigal, Y.J., et al., *Cdc42 and ARP2/3-independent regulation of filopodia by an integral membrane lipid-phosphatase-related protein.* J. Cell Sci., 2007. **120**(2): p. 340-352.

86. Straight, A.F., et al., *Dissecting Temporal and Spatial Control of Cytokinesis with a Myosin II Inhibitor.* Science, 2003. **299**(5613): p. 1743-1747.

87. Limouze, J., et al., *Specificity of blebbistatin, an inhibitor of myosin II.* Journal of Muscle Research and Cell Motility, 2004. **25**(4): p. 337-341.

88. Rosner, H., et al., *Attenuation of actinomyosinII contractile activity in growth cones accelerates filopodia-guided and microtubule-based neurite elongation.* Brain Research, 2007. **1176**: p. 1-10.

89. Faix, J. and K. Rottner, *The making of filopodia.* Current Opinion in Cell Biology, 2006. **18**(1): p. 18-25.

90. Rochlin, M.W., et al., *Localization of myosin II A and B isoforms in cultured neurons.* J Cell Sci, 1995. **108**(12): p. 3661-3670.

91. Bridgman, P.C., et al., *Myosin IIB Is Required for Growth Cone Motility.* J. Neurosci., 2001. **21**(16): p. 6159-6169.

92. Krasik, E.F., K.L. Yee, and D.A. Hammer, *Adhesive Dynamics Simulation of Neutrophil Arrest with Deterministic Activation.* Biophys. J., 2006. **91**(4): p. 1145-1155.

93. Nedelec, F., *Computer simulations reveal motor properties generating stable antiparallel microtubule interactions.* J. Cell Biol., 2002. **158**(6): p. 1005-1015.

94. Kruse, K. and F. J?licher, *Actively Contracting Bundles of Polar Filaments.* Physical Review Letters, 2000. **85**(8): p. 1778-1778.

95. Cytrynbaum, E.N., J.M. Scholey, and A. Mogilner, *A Force Balance Model of Early Spindle Pole Separation in Drosophila Embryos.* Biophys. J., 2003. **84**(2): p. 757-769.

96. Gardner, M., et al., *Chromosome congression by kinesin-5 motor-mediated disassembly of longer kinetochore microtubules.* Cell, 2008. **In Press**.

97. Janson, M.E., et al., *Crosslinkers and Motors Organize Dynamic Microtubules to Form Stable Bipolar Arrays in Fission Yeast.* Cell, 2007. **Vol 128**: p. 357-368.

98. Julicher, F. and J. Prost, *Spontaneous Oscillations of Collective Molecular Motors.* Physical Review Letters, 1997. **78**(23): p. 4510-4510.

99. Bruinsma, R., *Theory of Force Regulation by Nascent Adhesion Sites.* Biophys. J., 2005. **89**(1): p. 87-94.

100. Nicolas, A., B. Geiger, and S.A. Safran, *Cell mechanosensitivity controls the anisotropy of focal adhesions.* Proceedings of the National Academy of Sciences of the United States of America, 2004. **101**(34): p. 12520-5.

101. Nicolas, A. and S.A. Safran, *Limitation of Cell Adhesion by the Elasticity of the Extracellular Matrix.* Biophys. J., 2006. **91**(1): p. 61-73.

102. Khatiwala, C.B., S.R. Peyton, and A.J. Putnam, *Intrinsic mechanical properties of the extracellular matrix affect the behavior of pre-osteoblastic MC3T3-E1 cells.* Am J Physiol Cell Physiol, 2006. **290**(6): p. C1640-1650-C1640-1650.

103. Peyton, S.R. and A.J. Putnam, *Extracellular matrix rigidity governs smooth muscle cell motility in a biphasic fashion.* Journal of Cellular Physiology, 2005. **204**(1): p. 198-209.

104. Galbraith, C.G., K.M. Yamada, and M.P. Sheetz, *The relationship between force and focal complex development.* J. Cell Biol., 2002. **159**(4): p. 695-705.

105. Besser, A. and S.A. Safran, *Force-induced adsorption and anisotropic growth of focal adhesions.* Biophysical Journal, 2006. **90**(10): p. 3469-84.

106. Shemesh, T., et al., *Focal adhesions as mechanosensors: a physical mechanism.* Proceedings of the National Academy of Sciences of the United States of America, 2005. **102**(35): p. 12383-8.

107. Woo, S. and T.M. Gomez, *Rac1 and RhoA Promote Neurite Outgrowth through Formation and Stabilization of Growth Cone Point Contacts.* J. Neurosci., 2006. **26**(5): p. 1418-1428.

108. Wolgemuth, C.W., *Lamellipodial Contractions during Crawling and Spreading.* Biophys. J., 2005. **89**(3): p. 1643-1649.

109. Giannone, G., et al., *Lamellipodial Actin Mechanically Links Myosin Activity with Adhesion-Site Formation.* Cell, 2007. **Vol 128**: p. 561-575.

110. Erdmann, T. and U.S. Schwarz, *Stochastic dynamics of adhesion clusters under shared constant force and with rebinding.* The Journal of Chemical Physics, 2004. **121**(18): p. 8997-9017.

111. Schwarz, U.S., T. Erdmann, and I.B. Bischofs, *Focal adhesions as mechanosensors: the two-spring model.* Bio Systems, 2004. **83**(2-3): p. 225-32.

112. Molloy, J.E., et al., *Movement and force produced by a single myosin head.* Nature, 1995. **378**(6553): p. 209-12.

113. Cuda, G., et al., *In vitro actin filament sliding velocities produced by mixtures of different types of myosin.* Biophys. J., 1997. **72**(4): p. 1767-1779.

114. Lele, T.P., et al., *Investigating complexity of protein-protein interactions in focal adhesions.* Biochemical and Biophysical Research Communications, 2008. **369**(3): p. 929-934.

115. Jiang, G., et al., *Two-piconewton slip bond between fibronectin and the cytoskeleton depends on talin.* Nature, 2003. **424**(6946): p. 334-337.

116. Fisher, T.E., et al., *The study of protein mechanics with the atomic force microscope.* Trends in Biochemical Sciences, 1999. **24**(10): p. 379-384.

117. Joglekar, A.P., et al., *Molecular architecture of a kinetochore-microtubule attachment site.* Nat Cell Biol, 2006. **8**(6): p. 581-585.

118. Davis, T.N. and L. Wordeman, *Rings, bracelets, sleeves, and chevrons: new structures of kinetochore proteins.* Trends in Cell Biology, 2007. **17**(8): p. 377-382.

119. Meraldi, P., et al., *Phylogenetic and structural analysis of centromeric DNA and kinetochore proteins.* Genome Biol, 2006. **7**(3).

120. Tanaka, K., et al., *Molecular mechanisms of microtubule-dependent kinetochore transport toward spindle poles.* J. Cell Biol., 2007. **178**(2): p. 269-281.

121. Miranda, J., et al., *The yeast DASH complex forms closed rings on microtubules.* Nature Structural & Molecular Biology, 2005. **12**: p. 138-143.

122. Moores, C., et al., *The role of the kinesin-13 neck in microtubule depolymerization.* Cell Cycle, 2006. **5**(16): p. 1812-5.

123. Nicklas, R., *The Forces that Move Chromosomes in Mitosis.* Annual Reviews in Biophysics and Biophysical Chemistry, 1988. **17**(1): p. 431-449.

124. VanBuren, V., D. Odde, and L. Cassimeris, *Estimates of lateral and longitudinal bond energies within the microtubule lattice.* Proceedings of the National Academy of Sciences, 2002. **99**(9): p. 6035.

125. Northrup, S. and H. Erickson, *Kinetics of Protein-Protein Association Explained by Brownian Dynamics Computer Simulation.* Proceedings of the National Academy of Sciences, 1992. **89**(8): p. 3338-3342.

126. Olson, W., T. Spitznagel, and M. Yarmush, *Dissociation kinetics of antigen-antibody interactions: studies on a panel of anti-albumin monoclonal antibodies.* Mol Immunol, 1989. **26**(2): p. 129-36.

127. Wang, H., et al., *Architecture of the Dam1 kinetochore ring complex and implications for microtubule-driven assembly and force-coupling mechanisms.* Nature Structural & Molecular Biology, 2007. **14**: p. 721-726.

128. McIntosh, J., et al., *Fibrils Connect Microtubule Tips with Kinetochores: A Mechanism to Couple Tubulin Dynamics to Chromosome Motion.* Cell, 2008. **135**(2): p. 322-333.

129. Cheeseman, I., et al., *The Conserved KMN Network Constitutes the Core Microtubule-Binding Site of the Kinetochore.* Cell, 2006. **127**(5): p. 983-997.

130. Rieder, C. and E. Salmon, *The vertebrate cell kinetochore and its roles during mitosis.* Trends in Cell Biology, 1998. **8**(8): p. 310-318.

131. Cimini, D., et al., *Aurora Kinase Promotes Turnover of Kinetochore Microtubules to Reduce Chromosome Segregation Errors.* Current Biology, 2006. **16**(17): p. 1711-1718.